

HD-R124 006

STUDIES OF ELECTRON TRAPS IN GALLIUM ARSENIDE AND
GALLIUM ARSENIDE PHOSPH. (U) ILLINOIS UNIV AT URBANA
COORDINATED SCIENCE LAB D 5 DAY MAR 80 R-877

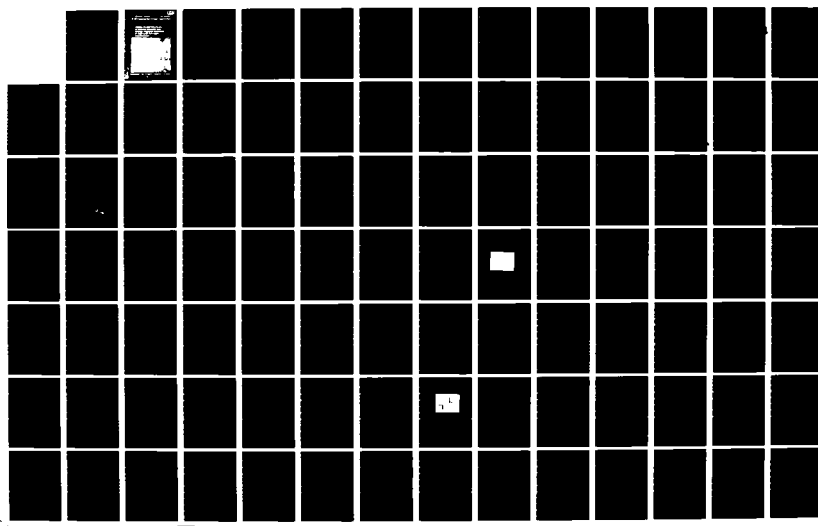
1/2

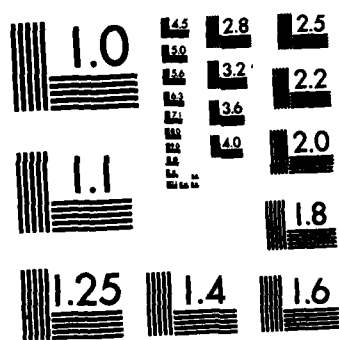
UNCLASSIFIED

N00014-79-C-0424

F/G 20/12

NL





MICROCOPY RESOLUTION TEST CHART
NATIONAL BUREAU OF STANDARDS-1963-A

ADA 124006

DEPARTMENT OF DEFENSE PROGRAM

DEPARTMENT OF DEFENSE
DEPARTMENT OF DEFENSE
DEPARTMENT OF DEFENSE
DEPARTMENT OF DEFENSE

CHICAGO, ILLINOIS

Unclassified

SECURITY CLASSIFICATION OF THIS PAGE (When Data Entered)

REPORT DOCUMENTATION PAGE		READ INSTRUCTIONS BEFORE COMPLETING FORM
1. REPORT NUMBER	2. GOVT ACCESSION NO.	3. RECIPIENT'S CATALOG NUMBER
		AD-A124006
4. TITLE (and Subtitle)		5. TYPE OF REPORT & PERIOD COVERED
STUDIES OF ELECTRON TRAPS IN GALLIUM ARSENIDE AND GALLIUM ARSENIDE PHOSPHIDE BY DEEP LEVEL TRANSIENT SPECTROSCOPY		Technical Report
7. AUTHOR(s)		6. PERFORMING ORG. REPORT NUMBER
Ding-Yuan Samuel Day		8. CONTRACT OR GRANT NUMBER(s)
		N00014-79-C-0424 N00014-76-C-0806
9. PERFORMING ORGANIZATION NAME AND ADDRESS		10. PROGRAM ELEMENT, PROJECT, TASK AREA & WORK UNIT NUMBERS
Coordinated Science Laboratory University of Illinois at Urbana-Champaign Urbana, Illinois 61801		
11. CONTROLLING OFFICE NAME AND ADDRESS		12. REPORT DATE
Office of Naval Research Arlington, Virginia		March 1980
14. MONITORING AGENCY NAME & ADDRESS (if different from Controlling Office)		13. NUMBER OF PAGES
		155
		15. SECURITY CLASS. (of this report)
		Unclassified
		15a. DECLASSIFICATION/DOWNGRADING SCHEDULE
16. DISTRIBUTION STATEMENT (of this Report)		
Approved for public release, distribution unlimited.		
17. DISTRIBUTION STATEMENT (of the abstract entered in Block 20, if different from Report)		
18. SUPPLEMENTARY NOTES		
19. KEY WORDS (Continue on reverse side if necessary and identify by block number)		
DLTS Semiconductors Defects		
20. ABSTRACT (Continue on reverse side if necessary and identify by block number)		
System effects and data analysis for deep level transient spectroscopy (DLTS) have been examined and applied to study the deep levels in the GaAs-GaP system. Studies of typical DLTS systems using either the lock-in amplifier or the dual-channel boxcar averager are presented. The effects of non-zero gate width for the boxcar averager, phase angle adjustment for the lock-in amplifier, and response time of a typical commercial capacitance meter are investigated. Errors introduced in the measurements by these effects are calculated for typical cases. Measurements of the gold level in silicon are presented, along with calculated correc-		

20. Abstract (Continued)

tions. We find the correction to be minimal in the boxcar-averager method, but significant in the lock-in amplifier approach.

A DLTS system is described for measuring deep levels in diodes exhibiting large leakage currents. A capacitance bridge is used employing the diode to be tested along with a dummy diode of similar characteristics. The DLTS spectrum of a leaky GaAs planar diode is measured and compared to experimental results obtained with two standard DLTS systems. It is shown that measurements with the standard systems are impossible in certain temperature ranges because of overloading problems. The approach described here, however, gives the DLTS spectrum between 77°K and 300°K.

In the study of the main electron trap (0.83eV from the conduction band) in VPE n-GaAs, we have examined the annealing behavior of this deep level and the effect of the implanted species. In the annealing study, we find that the trap concentration change is related to the Ga vacancy. In the implantation study, we observed that the trap concentration changes depending on whether the implanted species is incorporated into Ga or As substitutional sites. The DLTS results suggest that the main electron trap involves the Ga vacancy.

Electron traps in VPE n-GaAs_{1-x}P_x alloys with several compositions have been examined. It is observed that the DLTS spectra for the as-grown alloys are similar to each other. There are differences in DLTS spectra among the N-doped, N-free, and N-implanted samples for the same alloy composition. Deep levels caused by the radiation-induced damage are observed in the N-implanted samples.

Accession For	
NTIS GRA&I	<input checked="" type="checkbox"/>
DTIC TAB	<input type="checkbox"/>
Unannounced	<input type="checkbox"/>
Justification	
By _____	
Distribution/	
Availability Codes	
Avail and/or	
Dist	Special
A	



STUDIES OF ELECTRON TRAPS IN GALLIUM ARSENIDE AND GALLIUM
ARSENIDE PHOSPHIDE BY DEEP LEVEL TRANSIENT SPECTROSCOPY

by

Ding-Yuan Samuel Day

This work was supported in part by the Joint Services Electronics
Program (U.S. Army, U.S. Navy and U.S. Air Force) under Contract N00014-
79-C-0424 and the Office of Naval Research under Contract N00014-76-C-0806.

Reproduction in whole or in part is permitted for any purpose
of the United State Government.

Approved for public release. Distribution unlimited.

STUDIES OF ELECTRON TRAPS IN GALLIUM ARSENIDE AND GALLIUM
ARSENIDE PHOSPHIDE BY DEEP LEVEL TRANSIENT SPECTROSCOPY

BY
DING-YUAN SAMUEL DAY

B.S., National Taiwan University, 1973
M.S., Michigan State University, 1976

THESIS

Submitted in partial fulfillment of the requirements
for the degree of Doctor of Philosophy in Electrical Engineering
in the Graduate College of the
University of Illinois at Urbana-Champaign, 1980

Thesis Advisor: B. G. Streetman

Urbana, Illinois

STUDIES OF ELECTRON TRAPS IN GALLIUM ARSENIDE AND GALLIUM
ARSENIDE PHOSPHIDE BY DEEP LEVEL TRANSIENT SPECTROSCOPY

Ding-Yuan Samuel Day, Ph.D.
Coordinated Science Laboratory and
Department of Electrical Engineering
University of Illinois at Urbana-Champaign, 1980

System effects and data analysis for deep level transient spectroscopy (DLTS) have been examined and applied to study the deep levels in the GaAs-GaP system.

Studies of typical DLTS systems using either the lock-in amplifier or the dual-channel boxcar averager are presented. The effects of non-zero gate width for the boxcar averager, phase angle adjustment for the lock-in amplifier, and response time of a typical commercial capacitance meter are investigated. Errors introduced in the measurements by these effects are calculated for typical cases. Measurements of the gold level in silicon are presented, along with calculated corrections. We find the correction to be minimal in the boxcar-averager method, but significant in the lock-in amplifier approach.

A DLTS system is described for measuring deep levels in diodes exhibiting large leakage currents. A capacitance bridge is used employing the diode to be tested along with a dummy diode of similar characteristics. The DLTS spectrum of a leaky GaAs planar diode is measured and compared to experimental results obtained with two standard DLTS systems. It is shown that measurements with the standard systems are impossible in certain temperature ranges because of overloading problems. The approach described here, however, gives the DLTS spectrum between 77° and 300°K.

In the study of the main electron trap (0.83eV from the conduction band) in VPE n-GaAs, we have examined the annealing behavior of this deep level and the effect of the implanted species. In the annealing study, we find that the trap concentration change is related to the Ga vacancy. In the implantation study, we observed that the trap concentration changes depending on whether the implanted species is incorporated into Ga or As substitutional sites. The DLTS results suggest that the main electron trap involves the Ga vacancy.

Electron traps in VPE n-GaAs_{1-x}^P_x alloys with several compositions have been examined. It is observed that the DLTS spectra for the as-grown alloys are similar to each other. There are differences in DLTS spectra among the N-doped, N-free, and N-implanted samples for the same alloy composition. Deep levels caused by the radiation-induced damage are observed in the N-implanted samples.

ACKNOWLEDGEMENTS

The author is deeply grateful to Professor B. G. Streetman for his guidance, encouragement and generous support that made this work possible.

The author wishes to thank Professor G. E. Stillman and Professor K. Hess for their encouragement and for many helpful discussions. He would like to acknowledge the support and encouragement of Professor G. E. Anner. He is grateful to Professor H. Morkoç for helpful discussions and for providing MBE GaAs.

The author is especially indebted to Dr. D. V. Lang of Bell Laboratories for inspiring discussions and collaboration. He is grateful to Dr. L. C. Kimerling of Bell Laboratories for kindly help, Dr. W. O. Groves of Monsanto Co., for Donating VPE GaAs and Dr. D. R. Myers of the National Bureau of Standards for providing Au-doped Si diodes.

The author immensely appreciates the assistance and friendship of his colleagues Dr. G. T. Marcyk, Dr. M. Y. Tsai, Dr. M. Feng, Dr. R. A. Milano, Dr. M. J. Helix, Dr. K. V. Vaidyanathan, Dr. D. J. Wolford, J. D. Oberstar, T. Yu, P. A. Martin, S. S. Chan, K. J. Soda, S. Shichijo, T. H. Windhorn, G. E. Bulman and L. W. Cook. He wishes to thank the many members, especially O. E. Gardner, of the professional staff of the Coordinated Science Laboratory, for their invaluable help throughout the course of this work. Special thanks go to Mrs. E. M. Kesler, Ms. L. A. Ruggieri and Ms. C. E. Cox for their careful typing of this manuscript.

Finally, the author dedicates this work to his wife Shin-Mann and daughter Shelley. The understanding, encouragement, help and love from his wife have been greatly appreciated.

TABLE OF CONTENTS

CHAPTER	Page
1. INTRODUCTION.....	1
2. BACKGROUND REVIEW.....	4
2.1 Generation-Recombination-Trapping Mechanism.....	4
2.2 Junction Capacitance Transient Technique.....	4
2.3 Deep Level Transient Spectroscopy.....	11
2.3.1 Majority and minority carrier traps.....	14
2.3.2 Trap concentration.....	14
2.3.3 Trap energy level.....	14
2.3.4 Capture cross section.....	15
2.4 Ion Implantation.....	16
2.5 Encapsulation and Anneal.....	20
2.5.1 Silicon dioxide deposition.....	20
2.5.2 Silicon nitride deposition.....	20
2.5.3 Anneal.....	23
3. DLTS STUDIES.....	24
3.1 DLTS Systems.....	24
3.1.1 DLTS system with a commercial capacitance meter...	24
3.1.2 DLTS set-up with a specially designed capaci- tance bridge.....	27
3.1.3 DLTS system with the two-diode method.....	32
3.2 System Effects and Data Analysis	42
3.2.1 Dual-channel boxcar averager	43
3.2.2 Lock-in amplifier	46
3.2.3 Experimental example and discussion	55
3.2.4 Summary	61
4. STUDIES OF ELECTRON TRAPS IN THE GaAs-GaP SYSTEM BY DEEP LEVEL TRANSIENT SPECTROSCOPY	63
4.1 Studies of Electron Traps in GaAs	63
4.1.1 Material preparation and device fabrication	63
4.1.2 Electron traps in VPE n-GaAs	65
4.1.3 Annealing behavior of electron trap V7 in epitaxial n-GaAs	76
4.1.4 Study of electron trap V7 in ion implanted VPE n-GaAs	91

CHAPTER	Page
4.2 Studies of Electron Traps in VPE n-GaAs Ternary Alloy	101
4.2.1 Material preparation and device fabrication	101
4.2.2 Electron traps in VPE n-GaP	103
4.2.3 Electron traps in VPE n-GaAs _{0.15} P _{0.85}	106
4.2.4 Electron traps in VPE n-GaAs _{0.35} P _{0.65}	111
4.2.5 Electron traps in VPE n-GaAs _{0.60} P _{0.40}	116
5. SUMMARY AND CONCLUSIONS	120
5.1 DLTS Studies	120
5.2 Studies of Electron Traps in GaAs	122
5.3 Studies of Electron Traps in GaAs _{1-x} P _x Alloys	123
5.4 Suggestions for Further Investigations	124
References	126
Appendix A: Lock-in Amplifier Operation and Numerical Computation Program for the DLTS System	131
Appendix B: Dual-channel Boxcar Averager Operation and Numerical Computation Programs for the DLTS System	140
Appendix C: Computer Programs for Calculating Thermal Activation Energies and Capture Cross Sections for DLTS Systems Using Either the Lock-in Amplifier or the Boxcar Averager	144
Appendix D: Projected Range Statistics of Implanted B, Be, Ga, O, and N in GaAs, obtained from LSS Theory	149
VITA	155

I. INTRODUCTION

Defects and deep impurity centers in semiconductor materials are sites of generation, recombination, and trapping of electrons and holes. These centers have important effects on the electrical and optical performance of semiconductor devices. Some of these centers are introduced intentionally during the device fabrication processes to produce desirable electrical or optical characteristics, for example, gold centers are used in Si switching devices, chromium in semi-insulating GaAs, and nitrogen isoelectronic traps in $\text{GaAs}_{1-x}\text{P}_x$ LED's. However, some deep levels are incorporated unintentionally, and can undesirably lower the yield of good devices and circuits, such as nonradiative recombination centers in GaP LED's and the radiation damage after ion implantation.

The generation-recombination-trapping kinetics associated with a single level in the bandgap have been analyzed by Shockley and Read [1], Hall [2], and extended to multilevel systems by Sah and Shockley [3]. Deep levels in semiconductors have been poorly understood due to the lack of convenient and effective experimental methods, as well as the theoretically difficult nature of this topic [4]. A transient capacitance technique [5] has been developed in conjunction with thermally stimulated current (TSC) and photoconductivity measurements to provide information on the electrical properties of deep impurities and defects [6,7]. More recently, a powerful transient capacitance spectroscopic method, called Deep Level Transient Spectroscopy (DLTS), has been developed by Lang [8]. The DLTS method is particularly useful for studying levels deeper than about 0.1eV in the bandgap, whether they are radiative or not [4]. DLTS is therefore a complementary tool to photoluminescence

measurements, which are suitable for studying only radiative centers [4]. This technique has been applied to the study of bulk deep levels as well as to interface states [8-12].

Ion implantation has been accepted as one of the most important techniques for device fabrication, as well as for semiconductor research. Ion-implanted semiconductor material contains considerable lattice damage [13,14], and post-implant annealing is necessary to obtain high electrical and optical activation. Recently laser-beam [15-19] and electron-beam [20,21] techniques have been used to supplement or replace conventional high temperature thermal annealing in the reordering of implanted material. However, these two annealing techniques are still in their infancy. In this work, ion implantation is used as a powerful tool for its doping controllability, uniformity and reproducibility, and the conventional high temperature thermal anneal is used because of its reliability and widespread applications.

Although the epitaxial growth of III-V compound materials has made significant progress, the existence of discrete deep states in considerable concentrations in these materials is an obvious limitation. Considerable efforts are underway to assess the deep level content with respect to concentration, electronic properties, and physico-chemical origin. For our study of epitaxial GaAs material, we concentrate on a dominant electron trap which is closely related to the growth process. This trapping center is usually in the order of 10^{14} cm^{-3} concentration in VPE GaAs [22,23] and is not detected in typical LPE or MBE material. For the $\text{GaAs}_{1-x}\text{P}_x$ alloy, there have been limited reports on deep levels by the DLTS method [24-28]. In this work, we examine the deep levels

in various available alloy compositions of the ternary alloy. This is an important step for future work in this laboratory to understand the behavior of deep levels in various alloy composition, with the eventual goal of developing a unified theoretical explanation of deep level behavior.

A general background review is given in Chapter 2. The DLTS setup, system effects, and data analysis are addressed in detail in Chapter 3. The experimental results and discussions concerning the work on GaAs and $\text{GaAs}_{1-x} \text{P}_x$ are elaborated in Chapter 4. Finally a summary and suggestions for future study are given in Chapter 5.

2. BACKGROUND REVIEW

2.1 Generation-Recombination-Trapping Mechanism

The three most important processes by which transitions occur at deep levels are thermal, optical, and Auger processes. For the thermal process, energy and momentum are conserved with participation of phonons; for the optical process energy conservation is provided by photons, and momentum conservation by phonons; in the Auger-impact process, other carriers accommodate both energy and momentum conservation. These processes are shown for a single level in the bandgap in Fig. 2.1, where [6]

- E_C, E_V = conduction and valence band edges, respectively.
- E_T = energy position of the deep level.
- n, p = electron and hole concentrations, respectively.
- n_T, p_T = occupied and empty deep level concentrations, respectively.
- c_n^t, c_n^o = electron thermal and optical capture rates, respectively.
- c_n^n, c_n^p = electron Auger capture rates by excitations of another electron and hole, respectively.
- e_n^t, e_n^o = electron thermal and optical emission rates respectively.
- e_n^n, e_n^p = electron impact emission rates by impact with another electron and hole, respectively.

The parameters c and e with subscript p are analogous quantities for holes.

2.2 Junction Capacitance Transient Technique

Consider the thermal process in Fig. 2.1 (the superscript t is dropped, since a thermal process is understood):

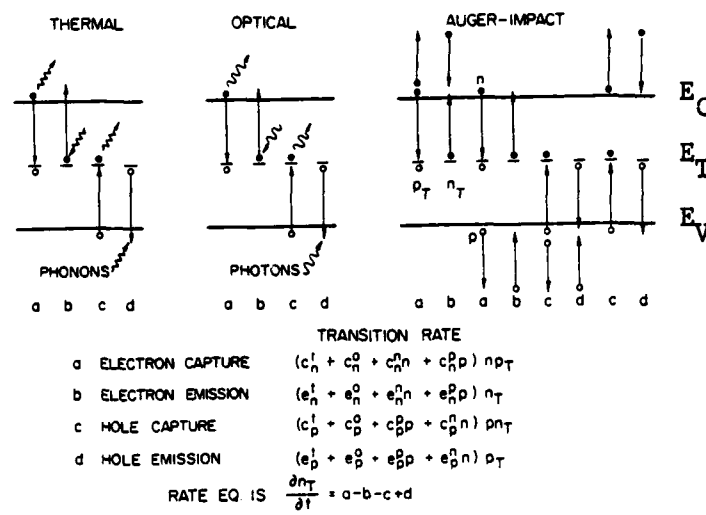


Fig. 2.1. Electron and hole capture and emission transitions; the transition rate of the thermal, optical and Auger-impact processes at deep level (Sah [6]).

$$\frac{dn_T}{dt} = c_n n (N_{TT} - n_T) - e_n n_T - c_p p n_T + e_p (N_{TT} - n_T) \quad (2.1)$$

where $N_{TT} = n_T + p_T$

The advantage of studying deep levels in a reverse-biased p-n junction or a Schottky barrier is the linearization of rate equations. Also, data accuracy is better compared with low temperature Hall measurements [29]. In the depletion region,

$$n = p \approx 0$$

$$\frac{dn_T}{dt} = - (e_n + e_p) n_T + e_p N_{TT}$$

and

$$n_T(t) = N_{TT} \frac{e_p}{e_p + e_n} + N_{TT} \frac{e_n}{e_p + e_n} \exp [-(e_p + e_n)t] \quad (2.2)$$

if $n_T(0) = N_{TT}$

The thermal emission rate e_n can be related to the thermal capture rate c_n and thermal capture cross section σ_n by detailed balance at thermal equilibrium:

$$e_n = c_n N_C g_n e^{-(E_C - E_T)/k_B T} = \sigma_n \langle v_n \rangle N_C g_n e^{-(E_C - E_T)/k_B T} \quad (2.3)$$

similarly

$$e_p = c_p N_V g_p e^{-(E_T - E_V)/k_B T} = \sigma_p \langle v_p \rangle N_V g_p e^{-(E_T - E_V)/k_B T} \quad (2.4)$$

where N_C and N_V are the effective densities of states in the conduction band extrema; g_n and g_p are the degeneracy factors of the deep level; $\langle v_n \rangle$ and $\langle v_p \rangle$ are the root-mean-square (rms) thermal velocities of

electrons and holes; and k_B is the Boltzmann constant. Generally, for an energy level in the upper (lower) half of the bandgap, the electron (hole) emission rate is much higher than the hole (electron) emission rate, so that the excitation of trapped holes (electrons) can be neglected. A deep level with $e_n \gg e_p$ ($e_p \gg e_n$) is classified as an electron (hole) trap. A deep level with $e_n \sim e_p$ is a recombination center.

For an electron trap, Eq. (2.2) can be simplified to

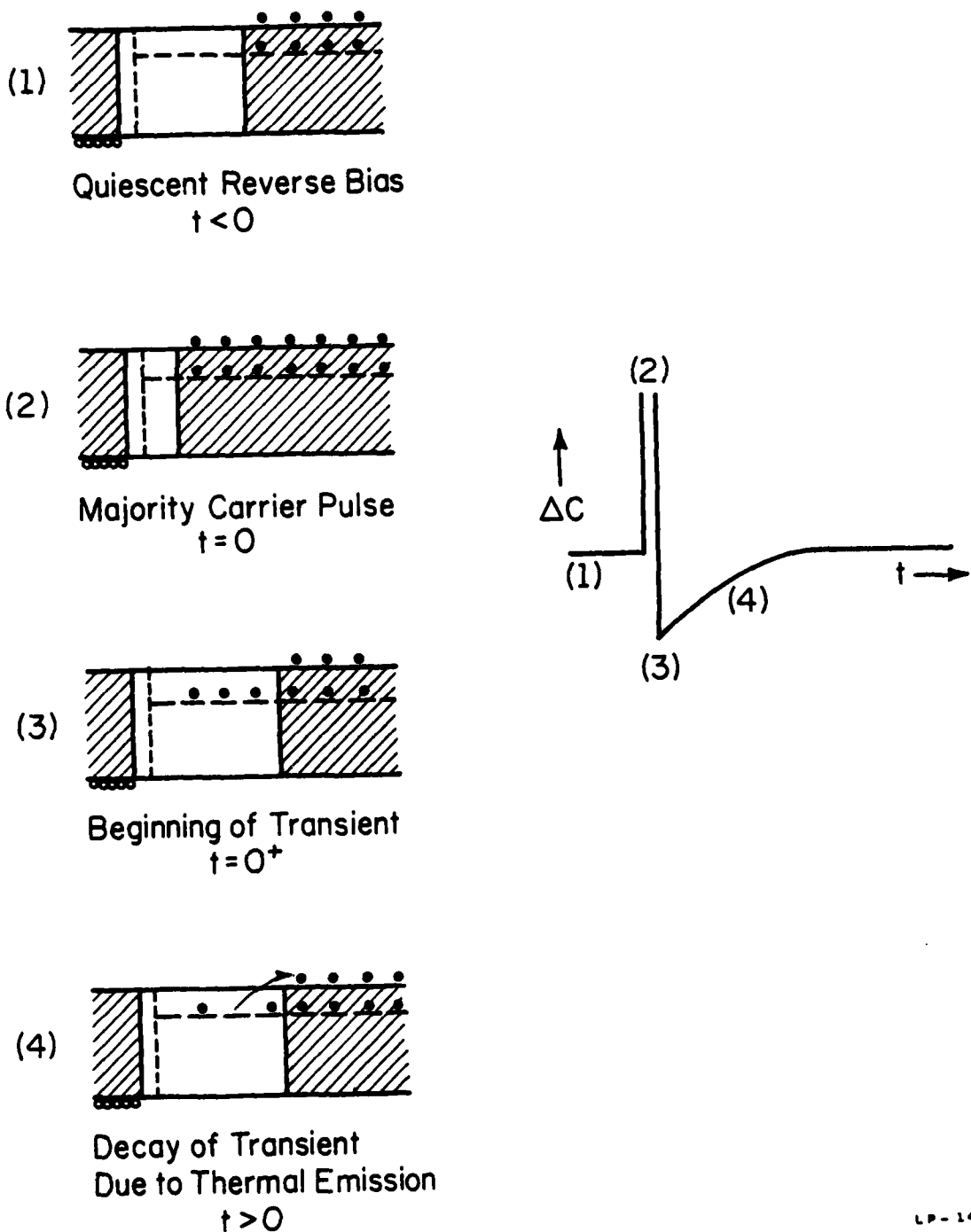
$$n_T(t) = N_{TT} \exp(-e_n t), \text{ if } n_T(0) = N_{TT}$$

As shown in Fig. 2.2 and Fig. 2.3, electron traps which are majority carrier traps can be filled up initially by a voltage pulse with an adequate duration, which collapses the depletion region. Hole traps which are minority carrier traps can not be filled unless the voltage pulse is large enough to forward bias the junction and inject the minority carriers.

It is known that the depletion region capacitance of an abrupt p^+ - n junction or a Schottky barrier on an n -type semiconductor is given by

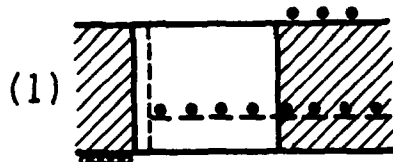
$$C = \frac{\epsilon A}{W} = A \sqrt{\frac{\epsilon q N_D^+}{2(V_R + V_{bi})}} \quad (2.5)$$

where V_{bi} is the built-in voltage of the junction or barrier; V_R is the reverse bias; ϵ is the permittivity of the semiconductor material; q is the electronic charge; N_D^+ is the net charge of uncompensated donors, which are assumed constant in the depletion region; A is the area of the junction or Schottky barrier; W is the depletion width. An analogous

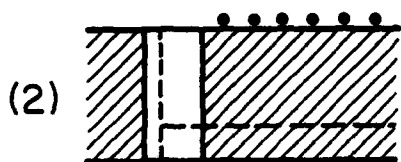


LP-1453

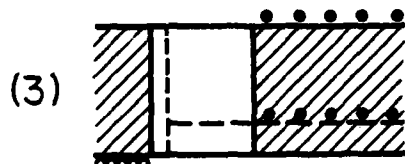
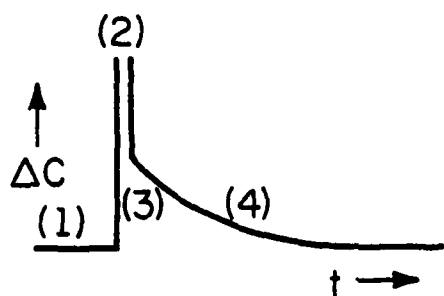
Fig. 2.2. Capacitance transient due to a majority carrier trap in a p^+ -n diode. The insets labeled 1 through 4 schematically show the charge state of the defect level and width of the space charge region (unshaded portion) at various times before and during the transient (Lang [8]).



Quiescent Reverse Bias
 $t < 0$



Injection Pulse
 $t = 0$



Beginning of Transient
 $t = 0^+$



Decay of Transient
Due to Thermal Emission
 $t > 0$

LP-1478

Fig. 2.3. Capacitance transient due to a minority carrier trap in a $p^+ - n$ diode (Lang [8]).

expression holds for an abrupt n^+ or Schottky barrier on p-type semiconductor material.

As shown in Fig. 2.2, before the trap-filling pulse there is a quiescent depletion width. The rapid and large capacitance change due to the depletion width reduction during the pulse period sometimes overloads the measurement system. Immediately after the pulse, the carriers in the shallow donor states are thermally excited into conduction band and swept away by the junction electric field. The capacitance then decreases to the value contributed by the net ionized donors and the electrons in the trapping centers. Thermal emission of the trapped electrons is a slow process, and the time constant τ_n ($1/e_n$) depends mainly on the ratio of the activation energy to the device temperature. Therefore, a slow capacitance transient can be observed in a suitable temperature range and utilized to extract the important parameters characterizing this deep level. If we assume the trapping centers are neutral when filled with electrons, then after the pulse the total charged centers are

$$N^+ = N_D^+ + N_{TT} (1 - e^{-t/\tau_n})$$

The capacitance transient can be obtained mathematically:

$$C(t) = A \sqrt{\epsilon_0 [N_D^+ + N_{TT} (1 - e^{-t/\tau_n})]} \quad (2.6)$$

$$\Delta C = C(\infty) - C(0) = C(\infty) [1 - \sqrt{\frac{N_D^+}{N_D^+ + N_{TT}}}] \quad (2.7)$$

The exact trap concentration in the depletion region can be obtained from ΔC if N_D^+ is known. If $\frac{N_{TT}^+}{N_D^+} < 0.1$, Eq. (2.6) can be simplified as

$$C(t) = A \sqrt{\frac{\epsilon q N_D}{2(V_R + V_{bi})} \left(1 - \frac{1}{2} \frac{N_{TT}}{N_D} e^{-t/\tau_n}\right)}$$

$$\Delta C(t) = C(\infty) - C(t) = C(\infty) \frac{1}{2} \frac{N_{TT}}{N_D} e^{-t/\tau_n} \quad (2.8)$$

$$\Delta C = \Delta C(0) = C(\infty) \frac{1}{2} \frac{N_{TT}}{N_D}$$

$$\frac{N_{TT}}{N_D} = \frac{2\Delta C}{C(\infty)} \quad (2.9)$$

By using the junction capacitance transient technique, the trap concentration, the thermal emission time constant, and hence the thermal activation energy can be obtained ideally [29]. For this method, the existence of only a single level must be known in advance. For a multi-level system it is not practical to use the computer to extract the time constants from the capacitance transient data. The DLTS method invented by Lang [8] is more powerful and is becoming increasingly popular in semiconductor research.

2.3 Deep Level Transient Spectroscopy

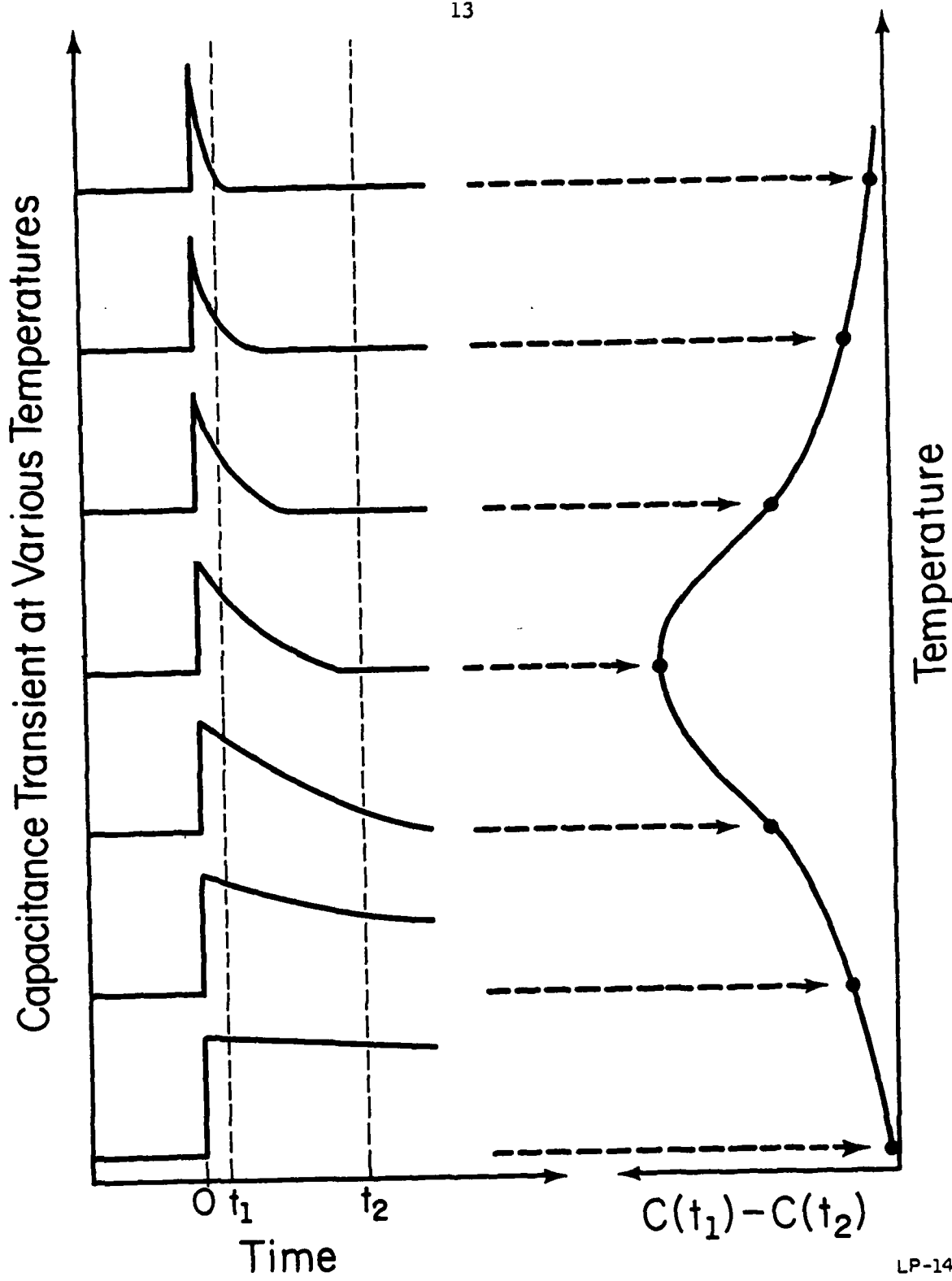
DLTS is basically a pulsed junction capacitance transient technique. The most important feature is the capability of displaying a spectrum of deep levels as a function of device temperature. The spectrum indicates the number and type (majority or minority carrier) of traps. Trap concentration, energy level and capture cross section can also be obtained to characterize the deep level.

Consider a reverse biased p^+ -n junction. A periodic capacitance transient is obtained if the junction is pulsed periodically to fill the traps. Since the thermal emission rate depends strongly on the ratio of the activation energy to the device temperature, the time constants for different energy levels may vary by orders of magnitude at a given same temperature. The key concept of the DLTS method is to preset a rate window electronically such that only the trap with an emission rate within the rate window can be observed by the DLTS system. The junction is thermally scanned so that each trap can be observed at the temperature where its emission rate is within the chosen rate window. Either a dual-channel boxcar averager or a lock-in amplifier [30-32] can be used to set the rate window and process the periodic capacitance transient. The details of this method will be discussed in Chapter 3.

Figure 2.4 is an illustration of how a dual-channel boxcar averager is used to define the rate window. The boxcar averager measures the difference of the capacitance transient at two sampling instants t_1 and t_2 . The boxcar output is thus given by

$$S(\tau) = C(t_1) - C(t_2) = \Delta C(e^{-t_1/\tau} - e^{-t_2/\tau}) \quad (2.10)$$

The signal $S(\tau)$ will reach a maximum at the temperature where the thermal emission time constant τ_{\max} is obtained from $\frac{dS(\tau)}{d\tau} \Big|_{\tau_{\max}} = 0$, or $\tau_{\max} = (t_2 - t_1)/\ln(t_2/t_1)$. As discussed above, the DLTS peaks for various levels appear at specific temperatures, and a DLTS spectrum is displayed in a single thermal scan.



LP-1490

Fig. 2.4. Illustration of how a dual-channel boxcar averager is used to define the rate window. The left hand side shows capacitance transients at various temperatures, while the right-hand side shows the corresponding DLTS signal resulting from using the boxcar averager to display the difference between the capacitances at times t_1 and t_2 as a function of temperature (Lang [8]).

2.3.1 Majority and minority carrier traps

As shown in Fig. 2.2 and Fig. 2.3, the capacitance transients due to a majority carrier trap and a minority carrier trap are of opposite polarity, as are the DLTS peaks. Therefore, a DLTS spectrum can indicate clearly the type of the trapping centers.

2.3.2 Trap concentration

The DLTS peak is proportional to ΔC , which is related to the trap concentration as given by Eq. (2.7) or Eq. (2.9).

2.3.3 Trap energy level

Equation (2.3) can be written as

$$e_n = 2 \left(\frac{3k_B}{m^*} \right)^{1/2} \left(\frac{2\pi k_B m_{dn}}{h^2} \right)^{3/2} g_n \sigma_n T^2 e^{-(E_C - E_T)/k_B T} \quad (2.11)$$

Where m^* is the conductivity electron effective mass; m_{dn} is the density of states electron effective mass; h is Planck's constant; and $E_C - E_T$ is the energy depth of the trap below the conduction band minimum. It has been shown that nonradiative capture and recombination by multi-phonon emission [33] (MPE) via lattice relaxation instead of cascade capture [34] is a commonly occurring nonradiative mechanism in both GaAs and GaP [33]. At sufficiently high temperature, the MPE process causes the capture cross section to increase exponentially with temperature. It is proposed that [24,33]

$$\sigma_n = \sigma_\infty e^{-W_\sigma/k_B T} \quad (2.12)$$

here W_σ is obtained from thermal capture rate measurement as a function of temperature. Therefore

$$e_n = 2 \left(\frac{3k_B}{m^*} \right)^{1/2} \left(\frac{2\pi k_B \cdot m_{dn}}{h^2} \right)^{3/2} \sigma_{\sigma} T^2 e^{-\Delta E/k_B T} \quad (2.13)$$

where

$$\Delta E = E_C - E_T + W_{\sigma}$$

Therefore,

$$T^2 \tau_n \approx e^{\Delta E/k_B T}$$

From the preset emission rate windows and the corresponding temperatures where the DLTS peaks for this level occur, an Arrhenius plot of $T^2 \tau_n$ VS $1/T$ can be obtained. The energy depth ΔE is thus obtained from the slope of this plot.

2.3.4 Capture cross section

The magnitude of the carrier capture cross section depends strongly on the capture process, charge states of the trapping centers, temperature, and electric field in the region of interest [35]. Capture cross section can be calculated from Eq. (2.13) or can be measured by the DLTS method as discussed here.

During the trap-filling pulse period, the parameters in Eq. (2.1) are of different values from those under a quiescent reverse bias. For an electron trap in the majority carrier case,

$$e_n \gg e_p$$

$$e_n = c_n n_1 \ll c_n n \quad \text{if } E_C - E_T \gg E_C - E_F$$

where

$$n_1 = g_n N_C e^{- (E_C - E_T) / k_B T}$$

$$p \approx 0$$

so

$$\frac{dn_T}{dt} = -c_n n n_T + c_n n N_{TT}$$

$$n_T(t) = N_{TT} (1 - e^{-c_n n t}), \text{ if } n_T(0) = 0$$

where at the end of pulse duration w , the filled trap concentration is

$$n_T(w) = N_{TT} (1 - e^{-c_n n w}) \quad (2.15)$$

and

$$n_T(w) = N_{TT} \text{ if } w \gg (c_n n)^{-1}$$

By observing the DLTS peak values for different pulse durations, $n_T(w)$ replaces N_{TT} in Eq. (2.9):

$$\frac{n_T(w)}{N_D} = \frac{2AC}{C(\infty)} \quad (2.16)$$

The thermal capture rate can be obtained from Eq. (2.15) and Eq. (2.16).

The thermal capture cross section can then be calculated from

$c_n = \sigma_n \langle v_n \rangle$. In order to do the capture cross section measurement, the pulse generator should have a rise time as fast as possible because $(c_n n)^{-1}$ is in the order of nanoseconds to microseconds.

2.4 Ion Implantation

Ion implantation is now a standard technique of doping semiconductors in the areas of field-effect transistors, integrated circuits, microwave devices, and optical detectors. It has the advantage of doping uniformity, controllability, and reproducibility when compared with conventional thermal diffusions. Furthermore, ion implantation can be utilized to introduce special ion species into semiconductors to produce desired properties. For instance, in studies of defects or deep impurities in semiconductors, one can implant certain ion species to create

deep levels and characterize these levels in terms of activation energies as well as capture cross sections. These results can pave the way to identify the deep levels which are important to the understanding of material properties and device physics.

Ion implantation denotes the bombardment of a solid substrate with ions in the keV to MeV energy range. A typical implanter, MP 300 keV ion implanter from Accelerators Inc., is shown schematically in Fig. 2.5. It consists of an ion source, a mass separator, and a target chamber. Source materials are introduced into the ion source and excited to obtain the desired ions. These ions are extracted from the source and accelerated by a high electric field. The ion beam is then deflected by a magnet and slit configuration so that the desired ions can be separated from unwanted species having different ratios of ion mass to ion charge. The ion beam is scanned over the target area to obtain a homogeneous doping. In the target chamber, the sample holder is tilted from the beam normal by an angle of 7° in order to avoid channelling of ions along specific crystal directions.

The distribution of implanted ions in the solid substrate depends on the acceleration voltage and the masses of the implanted ions and the host atoms. Stopping of the high energy ions by the target atoms occurs by interactions with core electrons and by nuclear collision processes. These primary collisions cause displacement of host atoms, which in turn are stopped by cascade collision processes. Hence, a statistical distribution of implanted ions occurs within the solid. For an amorphous target this distribution is peaked around the mean projected range R_p with a standard deviation ΔR_p . Tables of R_p and ΔR_p are

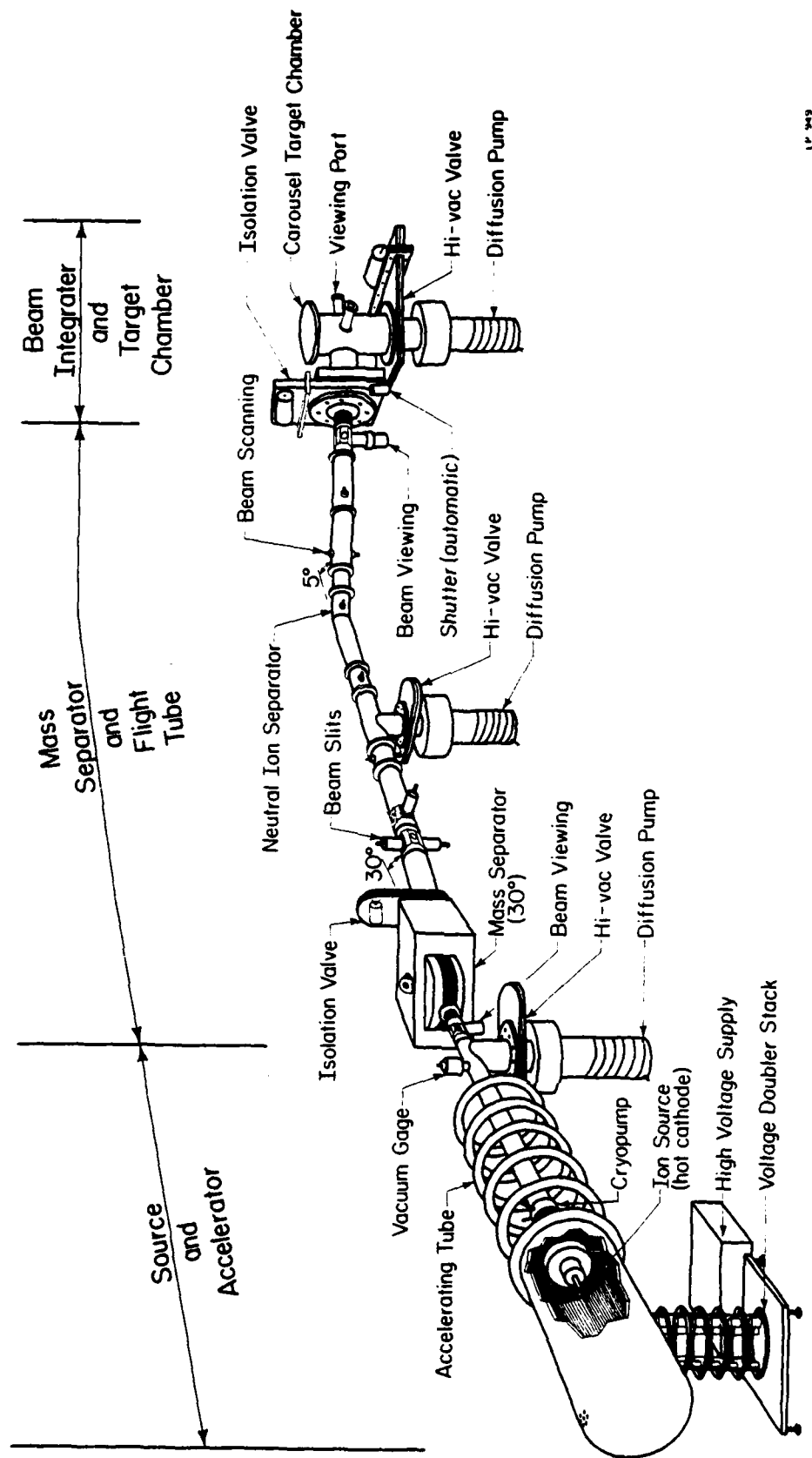


Fig. 2.5. Schematic diagram of the ion implantation system.

available [36], computed from the Lindhard-Scharff -Schiott (LSS) theory [37]. The implanted ion profile can usually be approximated by a Gaussian function given by

$$N(x) = N_p \exp \left[\frac{-(x-R_p)^2}{2\Delta R_p^2} \right] \quad (2.17)$$

where N_p is the peak concentration obtained at $x = R_p$:

$$N_p = \frac{0.4 N_D}{\Delta R_p}$$

and N_D is the fluence (also called dose) of the implant in unit of ions/cm². Some deviation of the profile from a Gaussian shape is usually expected because of higher order moments [36] neglected in Eq. (2.17).

The implanted ions are introduced into the crystal by brute force. The incorporation of foreign atoms into the crystal lattice is therefore far from what is expected at thermal equilibrium. The lattice damage depends on the dose, acceleration voltage, relative ion mass to target atom mass, and the temperature at which the implant is performed [14]. The location of implanted atoms in the lattice may be either substitutional or interstitial. Most defects caused by the implantation are unstable [14,38]. Even at room temperature they tend to form more stable configurations [14,30]. In order to restore the lattice order and semiconductor properties in the bombarded region, the substrate must be annealed at elevated temperatures. Although recrystallization of amorphized silicon layers can be achieved by annealing at $\sim 500^\circ\text{C}$ - 600°C for a few minutes in an inert ambient [39], residual defects are observed by the DLTS method [40,41]. The annealing behavior is therefore very

complex. Impurity atoms have to compete with lattice atoms and defects to obtain a stable incorporation. In order to fully recover the electrical and optical properties, annealing temperature as high as $900 \sim 1000^{\circ}\text{C}$ are necessary. For compound semiconductors protective surface layers or suitable ambients are necessary to avoid decomposition of the material due to the incongruent vaporization of compound elements [42]. Encapsulations by Si_3N_4 or SiO_2 layers are used in this work.

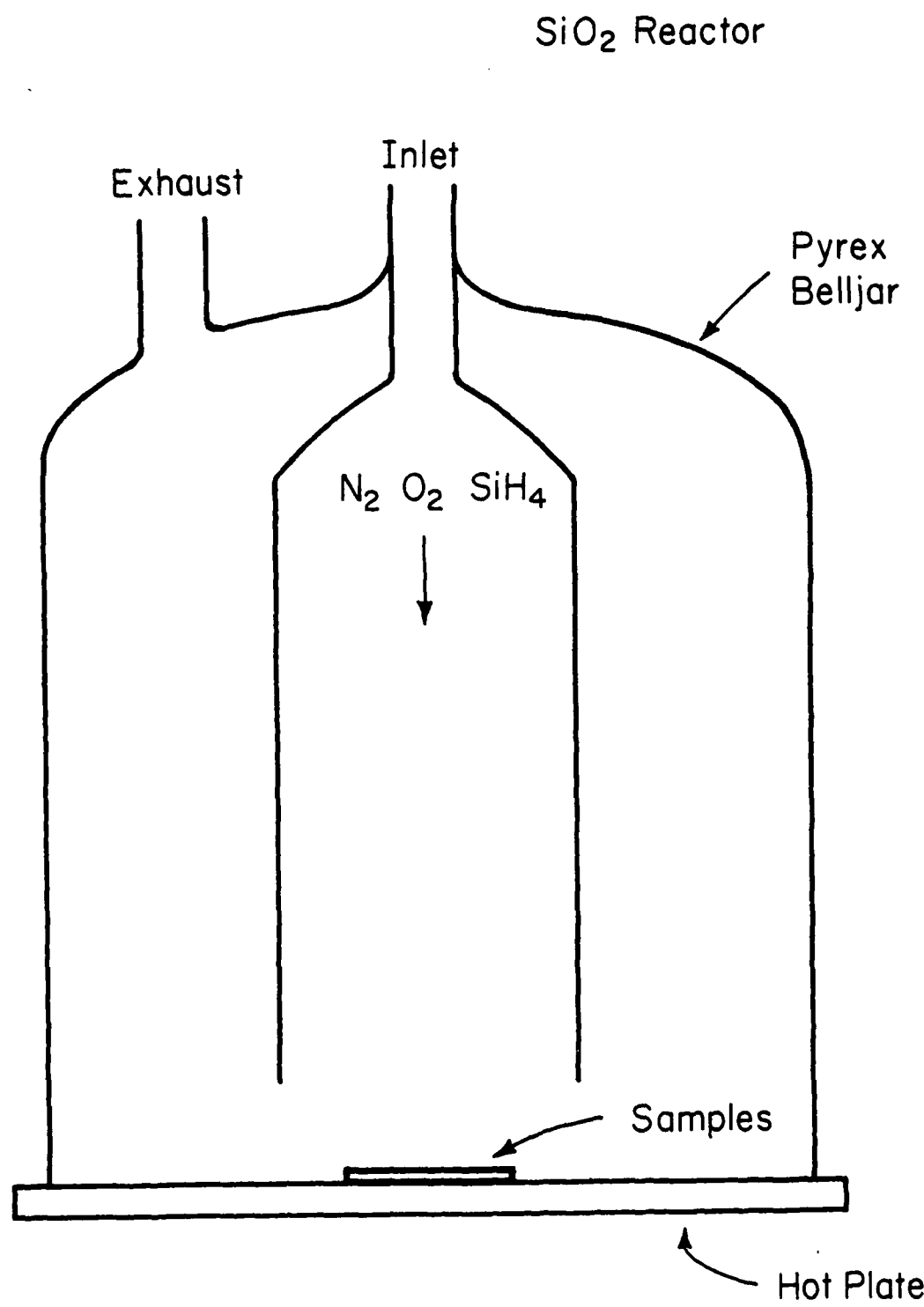
2.5 Encapsulation and Anneal

2.5.1 Silicon dioxide deposition

Shown in Fig. 2.6 is the SiO_2 deposition system, in which SiO_2 films are deposited by the oxidation of silane. A mixture of silane, nitrogen and oxygen, flow over the sample mounted on a heated plate at 500°C . The flow of gases is controlled by needle valves and monitored by flowmeters. The approximate flow rates are ~ 80 standard cubic centimeters per minute (SCCM) of nitrogen, ~ 1.1 SCCM of oxygen, and ~ 28 SCCM of 2% silane with 98% nitrogen. Films used in this work are typically $1000 \sim 1500 \text{ \AA}$.

2.5.2 Silicon Nitride Deposition

Figure 2.7 shows schematically the RF plasma Si_3N_4 deposition system [43]. The details of this system have been discussed elsewhere [44]. A brief operation procedure is given here. After loading the samples on a graphite heater, the chamber and gas line are pumped down to $< 3 \times 10^{-6}$ torr. A preliminary nitrogen discharge is initiated to remove remaining oxygen from the system while the sample is covered by a shutter. After running the nitrogen discharge for a few minutes, the rf power is turned off. After introducing nitrogen and silane to a



LP-1463

Fig. 2.6. Schematic diagram of silicon dioxide reactor.

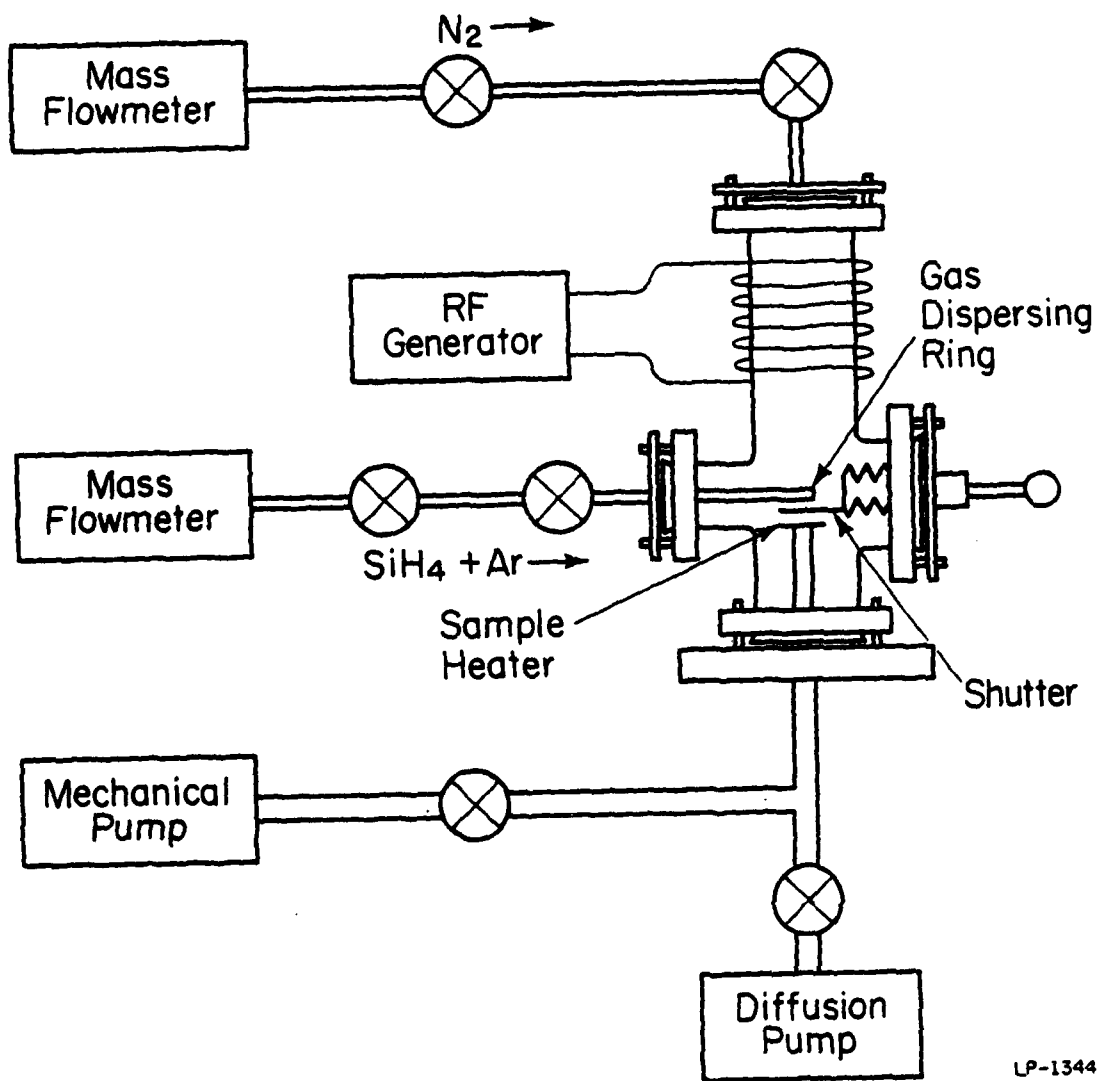


Fig. 2.7. Schematic diagram of rf plasma silicon nitride deposition system in which gases are introduced into reaction chamber separately (Helix [43]).

desired flow rate monitored by mass flowmeters, the shutter is removed, the sample is quickly heated to ~ 300 - 350°C , and plasma discharge is then initiated. For most encapsulation work the flow rates are 50 SCCM for N_2 and ~ 11 - 12.6 SCCM for the 2% SiH_4 in Ar. The films deposited are usually ~ 1000 - 1500 \AA . It has been shown [43,44] that Si_3N_4 films can be obtained with stoichiometric ratio ($\text{Si} : \text{N} = 0.75$), and both Rutherford backscattering and Auger electron spectroscopy show that the film contains little oxygen. This is an important result, since oxygen-contaminated nitrides allow gallium outdiffusion during the annealing of GaAs [45].

2.5.3 Anneal

The high temperature anneals are performed in a 12" Trans Temp furnace with a silica liner. The ambient during the anneal is flowing N_2 gas, and the temperature is monitored with a Chromel-Alumel thermocouple and Fluke 2100 A digital thermometer.

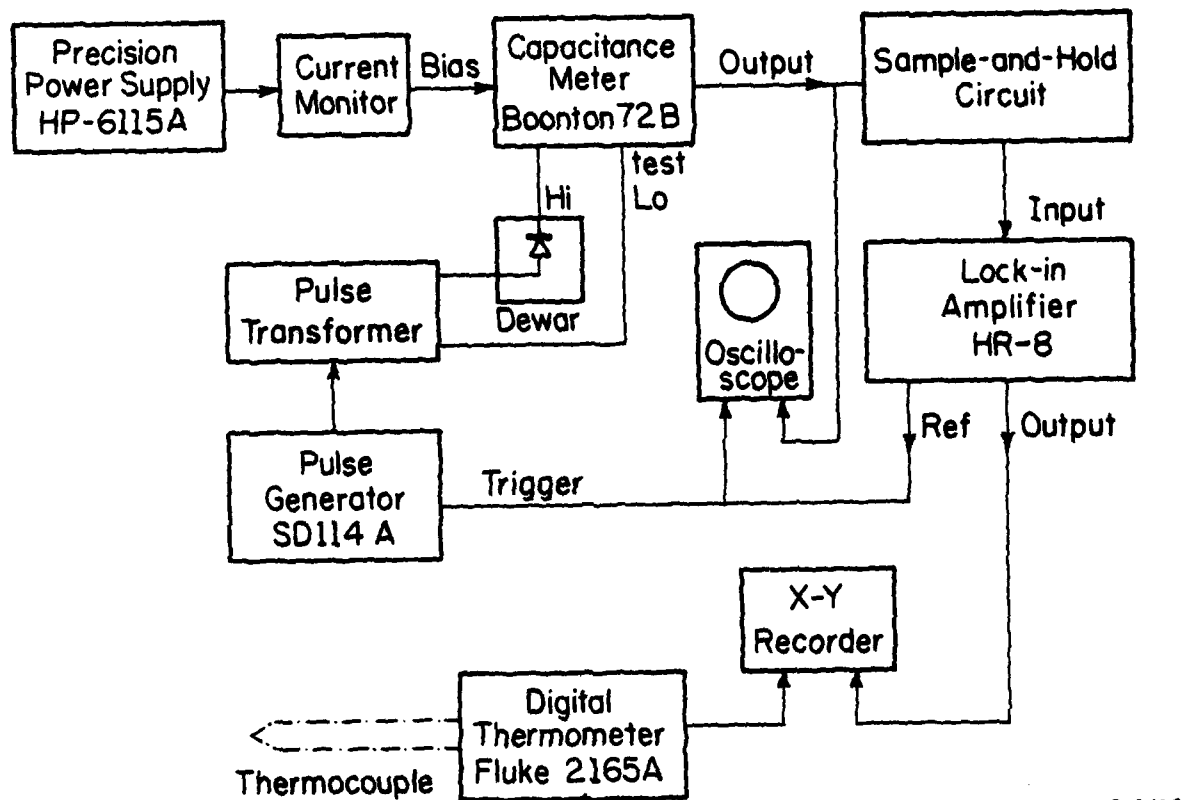
3. DLTS STUDIES

3.1 DLTS Systems3.1.1 DLTS system with a commercial capacitance meter

Shown in Fig. 3.1 is the block diagram of a DLTS system with a Boonton 72B capacitance meter used early in this work. The pulsed bias is generated by an HP-6115A precision power supply and a Systron-Donner SD114A pulse generator. The voltage pulse is coupled to the diode through a pulse transformer as shown in the diagram. A PAR HR-8 lock-in amplifier is used to process the capacitance transient and set the rate window. The lock-in output is plotted against temperature on an x-y recorder. A Sulfrian cryogenic dewar was modified for electrical measurement. An Artronix temperature controller is used for temperature selection and thermal scanning. Both a Chromel-Alumel thermocouple and a calibrated Rosemount temperature sensor are placed adjacent to the sample for accurate temperature measurement.

Distortion of the pulse waveform can occur due to the pulse transformer. This distortion problem is critical to the capture cross section measurement where a fast-rise pulse is required. The voltage pulse can be connected to the LO bias terminal of the Boonton 72B meter with a $50\ \Omega$ resistor to replace an internal shunt capacitor of $0.47\ \mu\text{F}$. With this change in the DLTS set-up as shown schematically in Fig. 3.2, one can avoid the pulse distortion considerably without using the pulse transformer.

A typical commercial capacitance meter such as Boonton 72B has a response time of about 1 ms. This relatively slow response time and consequent overloading problem of the meter during the pulsing period



LP-1418

Fig. 3.1. Block diagram of a DLTS system using a Boonton 72B capacitance meter and a pulse transformer.

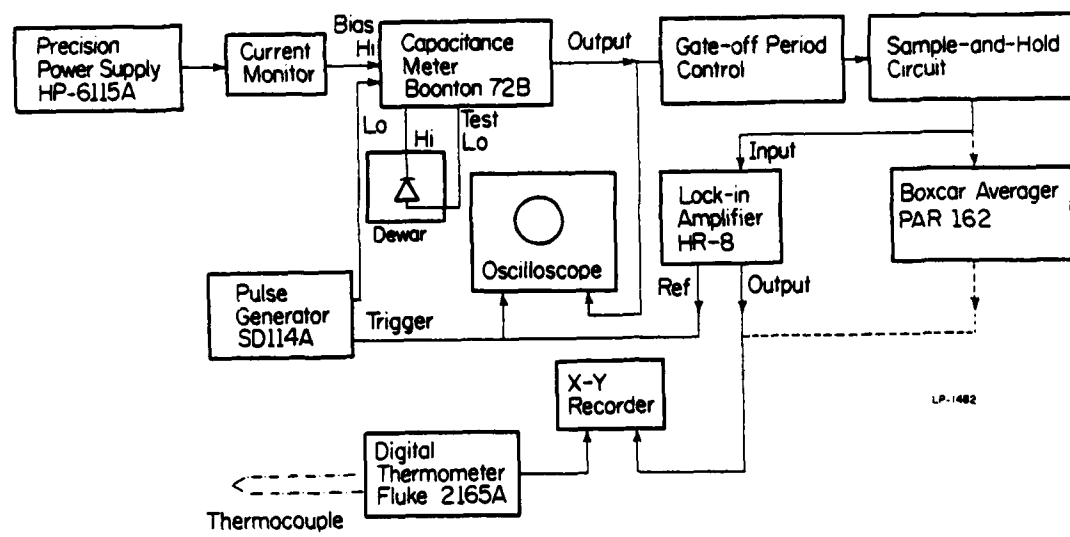


Fig. 3.2. Block diagram of a DLTS system using a Boonton 72B capacitance meter.

make it necessary to gate off the signal during the initial period of the transient in order to avoid spurious electrical effects due to the bias pulse. A detailed discussion of system effects and data analysis [46] is given in Section 3.2.

With the set-up shown in Fig. 3.2, we have examined the Au-doped Si diodes from the National Bureau of Standards to calibrate our DLTS system. In the fabrication of these diodes gold was evaporated on the back side of a Si wafer and diffused for 24 hrs. at 825°C to obtain a gold concentration of approximately 10^{13} cm^{-3} . The diode diameter used in this work was 17 mils. Shown in Fig. 3.3 are the DLTS spectra of the electron trap of Au in a typical $\text{p}^+ \text{n}$ junction. By adjusting the lock-in frequency to preset the rate window, we can obtain a DLTS spectrum for each rate window. From the emission rates and corresponding temperatures at the DLTS peaks, the energy level of this trap is estimated to be $0.54 \pm 0.01 \text{ eV}$ as shown in Fig. 3.4. The capture cross section σ_n is estimated to be $2 \times 10^{-15} \text{ cm}^2$ at room temperature, and the trap concentration is about $2 \times 10^{13} \text{ cm}^{-3}$. These data are consistent with previous work [47,48] and our system is properly calibrated. The decrease of the DLTS peak for higher frequency will be fully discussed in Sec. 3.2.

3.1.2 DLTS set-up with a specially designed capacitance bridge

In the junction capacitance transient technique, a capacitance transient is obtained due to the "slow" thermal emission process of carriers in the trapping centers. The emission is slow relative to the period of the driving signal of a capacitance bridge. The effect of driving frequency on the capacitance transient due to trapping centers

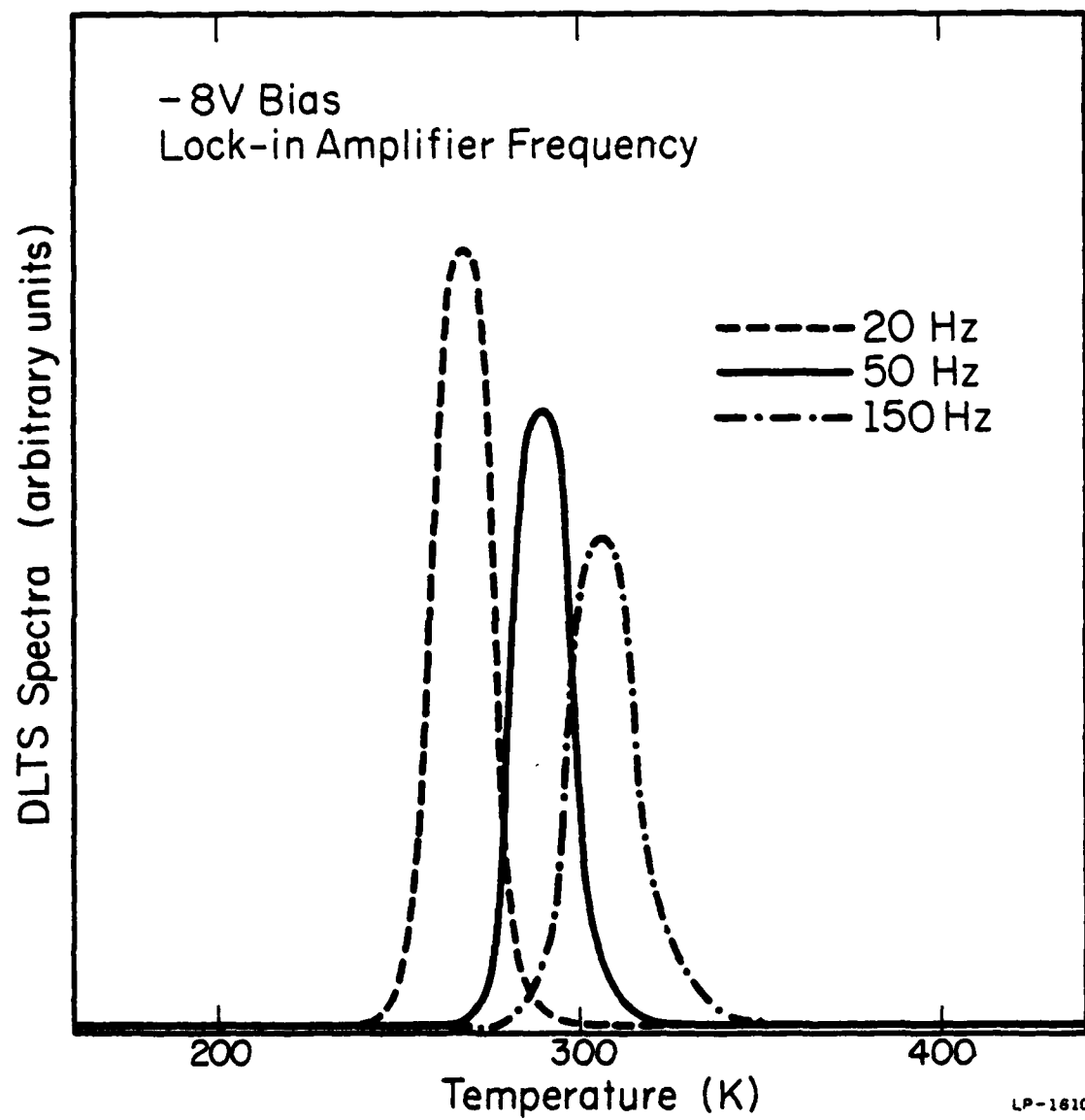


Fig. 3.3. DLTS spectra of the electron (majority carrier) trap in the Au diffused p^+ -n silicon junction for various lock-in frequency settings.

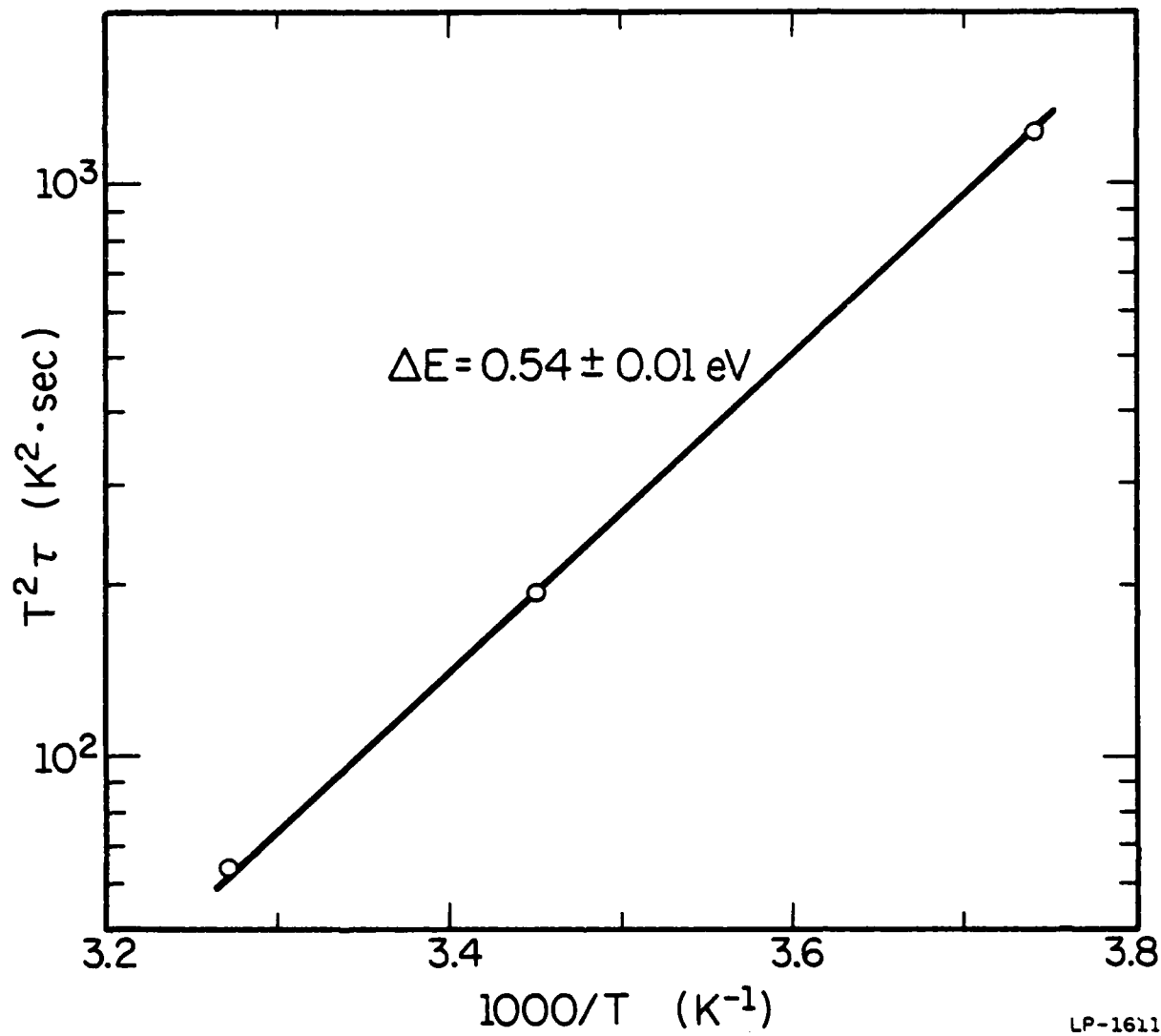


Fig. 3.4. Arrhenius plot of $T^2\tau$ vs. $1000/T$ obtained for the electron trap in the Au diffused p^+-n silicon junction.

has been experimentally demonstrated [49]. A wider range of trap energy and better S/N ratio can be obtained from higher driving frequency. Dr. D. V. Lang proposed a DLTS system with a capacitance bridge of 20 MHz [50] instead of 1 MHz as used in Boonton 72B. As shown in Fig. 3.5 is the block diagram of an improved DLTS system with a homemade capacitance bridge. Tektronix SG 503 provides a constant rf voltage output of 20 MHz . The rf signal power is split into the reference and test paths without interaction between the two. The reference rf voltage should be as large as possible to drive the HP rf mixer into saturation. In the testing path, the rf voltage across the test diode is kept $< 0.2V$ peak to peak [50] by a variable attenuator and the 50Ω output impedance of the pulse generator. The diode quiescent capacitance is nulled out by the attenuating and phase-shifting circuit in the dummy arm. Any impedance change of the test diode can be sensed and amplified by the PAR 115 low noise wideband amplifier. This signal is demodulated by the reference signal through a phase sensitive ~~detector~~. The phase shifter in the reference path is used to pick up either the conductive or the capacitive component of the impedance change in the test diode. A Boonton 76-3A standard capacitor across the diode is used to discriminate the capacitive mode, by maximizing the PAR 113 low noise pre-amplifier output in response to a 1 pF change in the standard capacitor. Although there are two other methods for mode-selection proposed by Dr. Lang, this is the most straightforward. The total system response time depends only on the PAR 113 output time constant, which is usually on the order of $1 \mu\text{sec}$. The system recovery time from overloading is $< 1 \mu\text{s}$ as long as the PAR 113 (which has a long recovery time) is not overloaded.

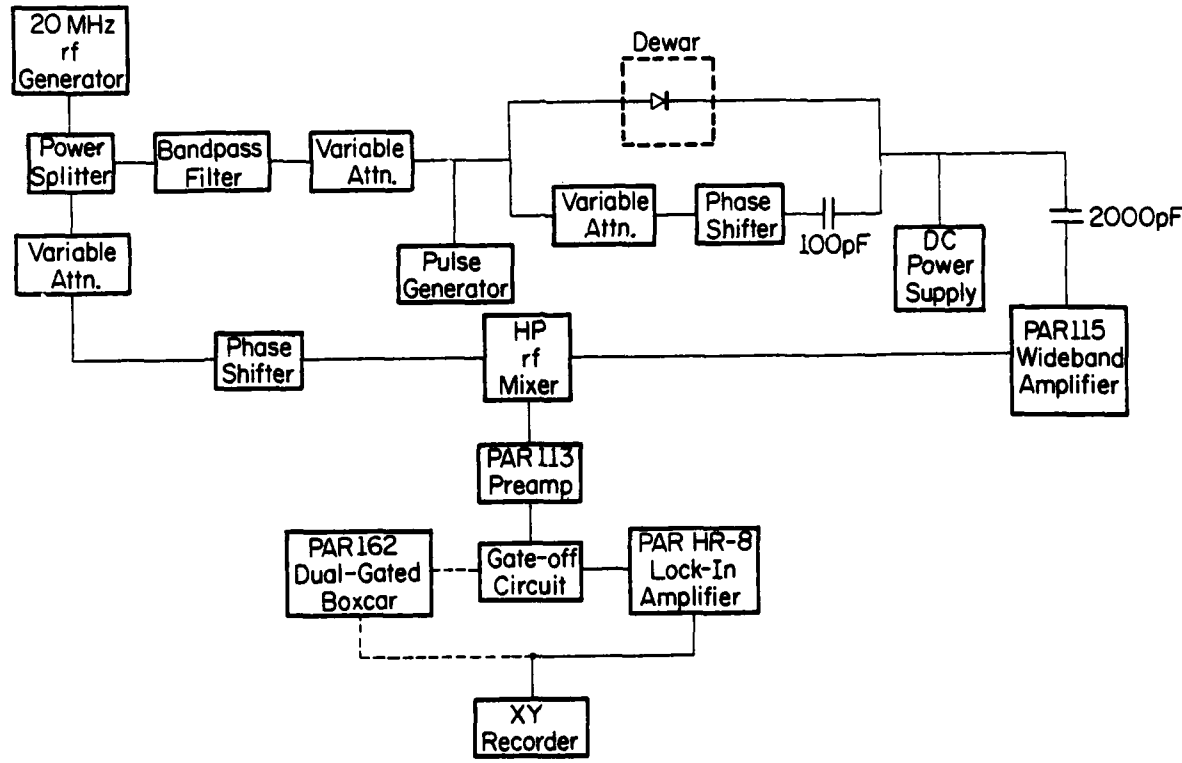


Fig. 3.5. DLTS system with a fast capacitance bridge of 1 μ sec response time (Lang [8]).

Shown in Fig. 3.6 is the DLTS spectrum of a p^+ n LPE GaAs diode obtained from Lang to calibrate our capacitance bridge. The p^+ layer is Ge-doped to $2 \times 10^{18} \text{ cm}^{-3}$ and the n layer is unintentionally doped with a net donor concentration of $1.5 \times 10^{16} \text{ cm}^{-3}$. There are two hole (minority carrier) traps with energy levels at $0.44 \pm 0.01 \text{ eV}$ and $0.76 \pm 0.01 \text{ eV}$ from the valence band edge. The estimated trap densities are $6.0 \times 10^{14} \text{ cm}^{-3}$ for the deeper one and $8.3 \times 10^{14} \text{ cm}^{-3}$ for the shallower one, as measured by Lang [8]. In addition, a n^+p gold diffused silicon diode is used to calibrate this system. As shown in Fig. 3.7, there are two hole (majority carrier) traps in the junction region. The estimated energy levels in this case are $0.33 \pm 0.01 \text{ eV}$ and $0.54 \pm 0.01 \text{ eV}$ from the valence band. These data agree very well with those observed by Miller et al [9].

3.1.3 DLTS system with the two-diode method

As discussed previously, DLTS measurements require a capacitance bridge with high sensitivity and fast response to detect the usually small capacitance transient. Since leakage currents are highly temperature sensitive, a large leakage current always prohibits a bridge circuit from being balanced on a high sensitivity scale over a wide range of device temperature. Naturally it is desirable to keep the leakage currents of the diodes as low as possible. However, applications of the DLTS method in the study of semiconductor defects often involve imperfect junctions. For example, diodes formed by ion implantation usually exhibit large leakage currents if the post-implant anneal conditions are not adequate to remove all radiation damage. As a consequence, it is difficult to apply DLTS to ion implanted structures, particularly in

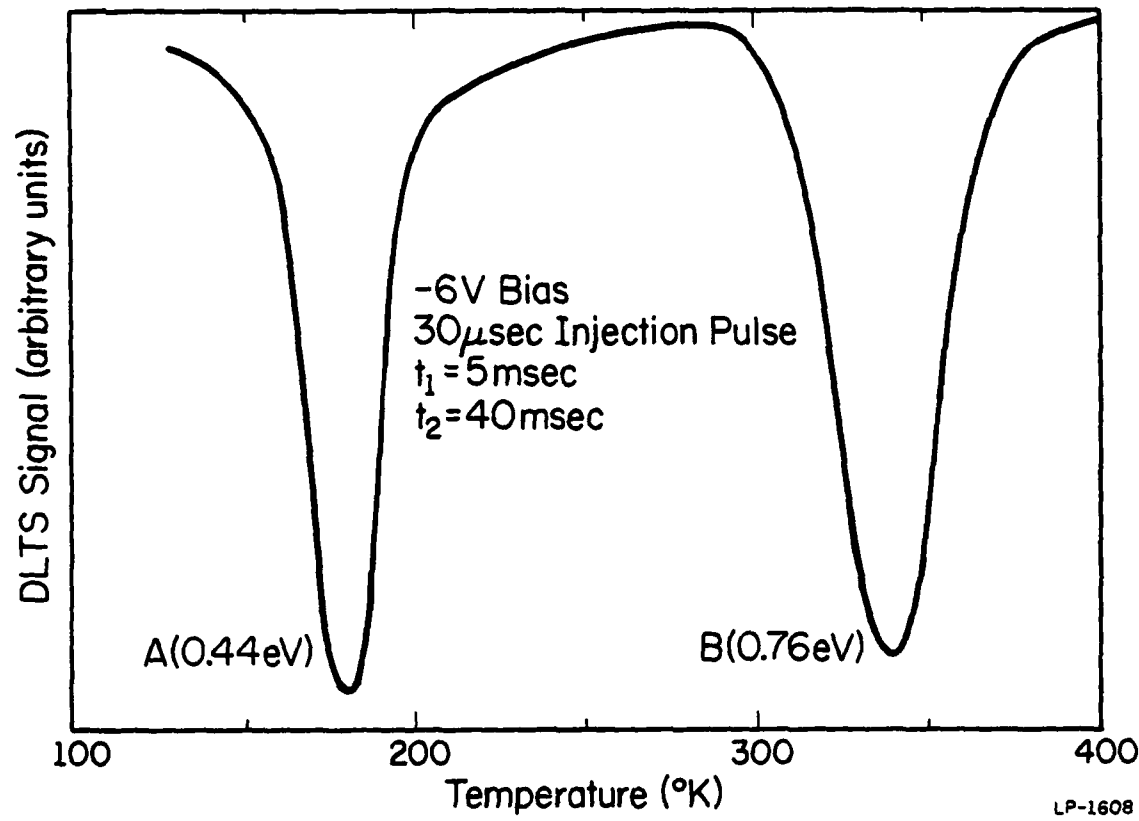


Fig. 3.6. DLTS spectrum of hole (minority carrier) traps in a p^+ -n GaAs junction.

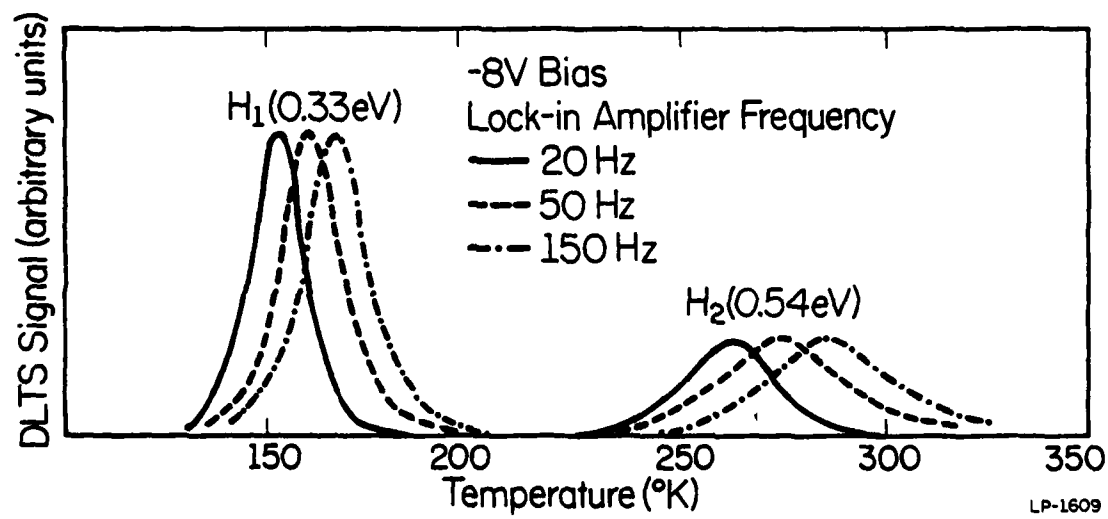


Fig. 3.7. DLTS spectra of hole (majority carrier) traps in the Au diffused n^+ - p silicon junction for various lock-in frequency settings.

the study of partially annealed material. In this section we describe a DLTS system using two similar diodes in the bridge circuit to offset the leakage currents. We examine the effects of diode leakage currents on the DLTS measurements made using this approach compared with two other systems. The experimental results of a leaky Be-implanted GaAs planar p^+ -n junction show that this new version successfully eliminates the problem of measuring diodes with appreciable leakage currents [51].

The DLTS system used in this work is shown in the block diagram of Fig. 3.8. Two diodes having similar C-V and I-V characteristics are mounted on the same header to minimize the temperature difference between the two devices. The 20 MHz driving signals across these two diodes are set 180° out of phase by a phase shifter, and kept below 0.2 V peak-to-peak. Hence, the quiescent capacitances of the two diodes under the same reverse bias are well balanced at any temperature. As usual, we apply a periodic voltage pulse for trap filling and emptying to detect deep levels in the depleted region of the junction. In order to pulse the test diode only, the pulse must pass through two variable attenuators, a bandpass filter, and a power splitter before reaching the dummy diode. The power splitters are used for impedance matching and decoupling the interactions between the two output arms.

A fast gate-off circuit along with its input and output waveforms is shown in Fig. 3.9. To gate-off the capacitance transient during the initial overloading period, the input signal is held at the value present just before the overloading period and then is sampled for the remaining period. The gate-off period (holding period) is controlled by the RC time constant of the NE 555 integrated circuit timer. The holding

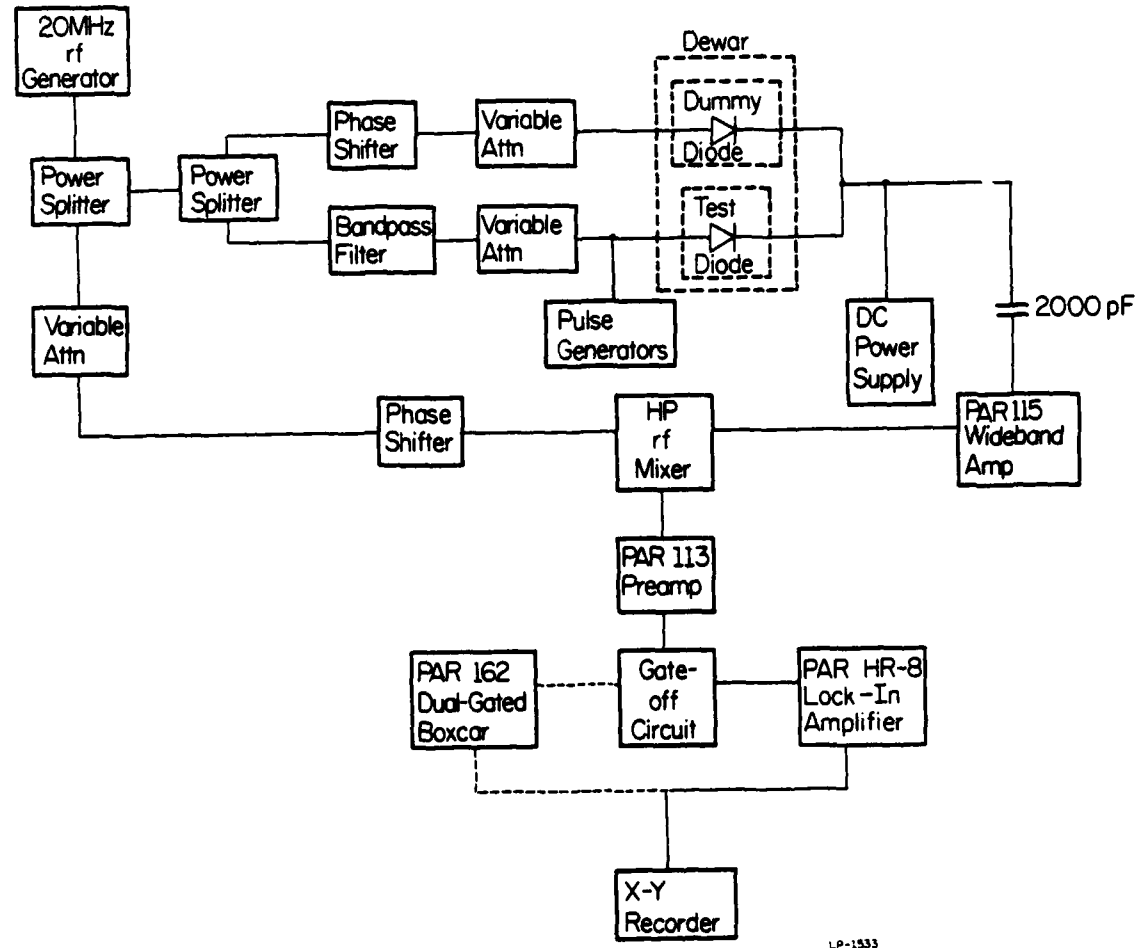


Fig. 3.8. Block diagram of a DLTS system using the two-diode method.

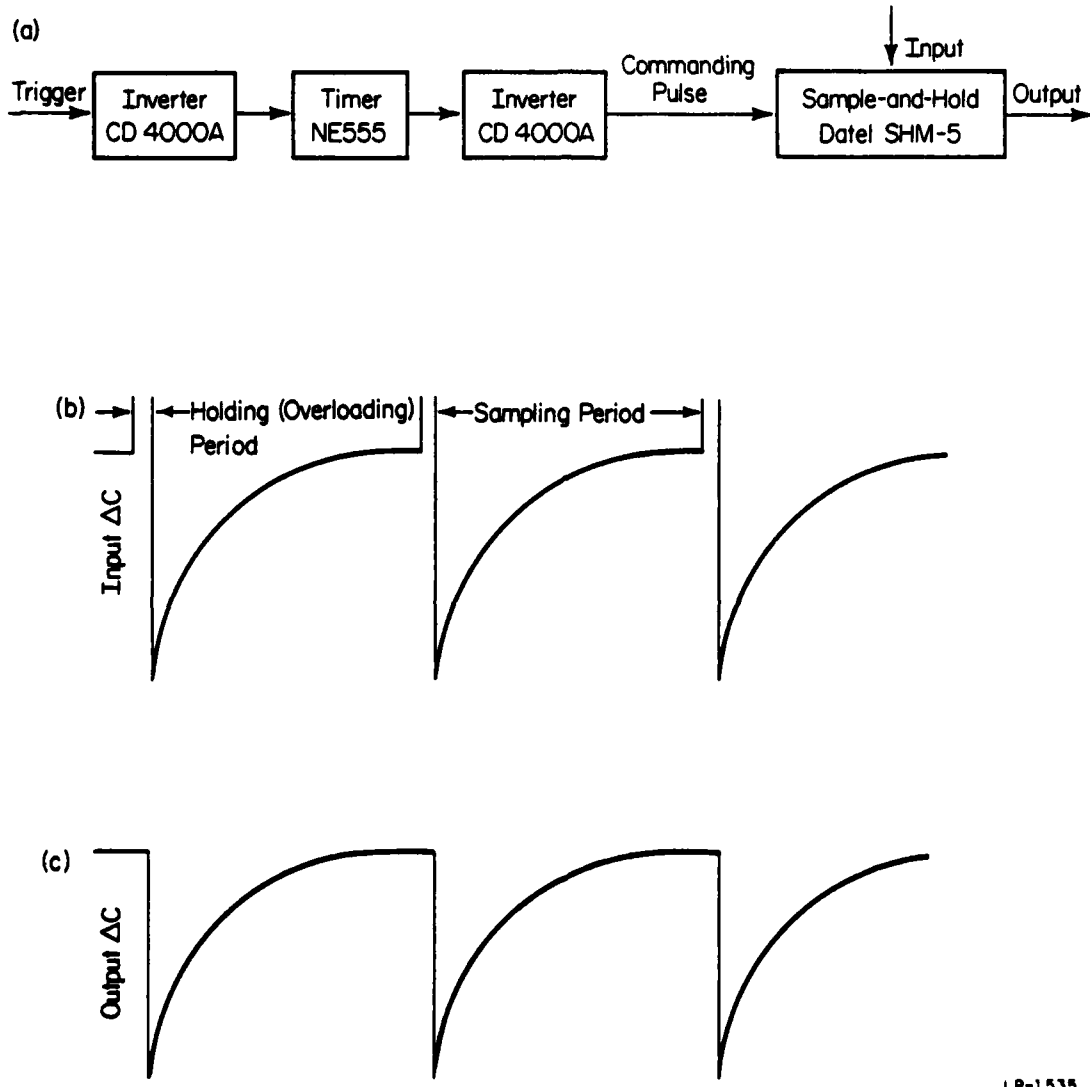


Fig. 3.9. A fast response gate-off circuit for the DLTS system using a lock-in amplifier: (a) block diagram; normalized exponential capacitance transient before (b) and after (c) gate-off.

and sampling commands should occur right before and after the bias pulse which causes the overloading. The synchronization output of a Systron-Donner 114A pulse generator is set ahead of the output pulse to trigger the holding command. The total response time of this gate-off circuit is less than 2 μ sec and therefore is compatible with the capacitance bridge.

DLTS measurements were performed using 20 V reverse bias and 20 μ sec pulse width on two similar implanted GaAs planar p-n junctions. These two leaky diodes were taken from the same area of the GaAs wafer, and therefore were subjected to the same fabrication processes. The diodes were formed by implanting 250 keV Be (10^{14} cm^{-2} fluence) into n-type VPE GaAs through a photoresist mask. The sample was encapsulated in Si_3N_4 and annealed for 30 minutes at 800°C . The I-V characteristic of the test diode is shown in Fig. 3.10. Three DLTS systems were used to make measurements on this diode. The first system is shown in Fig. 3.8. The second one, using a Boonton 72B capacitance meter, is shown in Fig. 3.2. The third system is shown in Fig. 3.5. A lock-in amplifier with the fast gate-off circuit is used on all three systems for this experiment.

The solid curve in Fig. 3.11 is the DLTS spectrum of the leaky diode using the two-diode system. It indicates that there are four deep electron traps in the junction region. The activation energies are 0.43, 0.58, 0.86 and 1.26 eV. The activation energies for these levels are obtained from the slopes of the Arrhenius plots of $T^2\tau$ vs. $1/T$. The thermal emission rate window, $1/\tau$, is set by a PAR HR-8 lock-in amplifier. The 0.43, 0.58, and 0.86 eV levels have been observed previously in

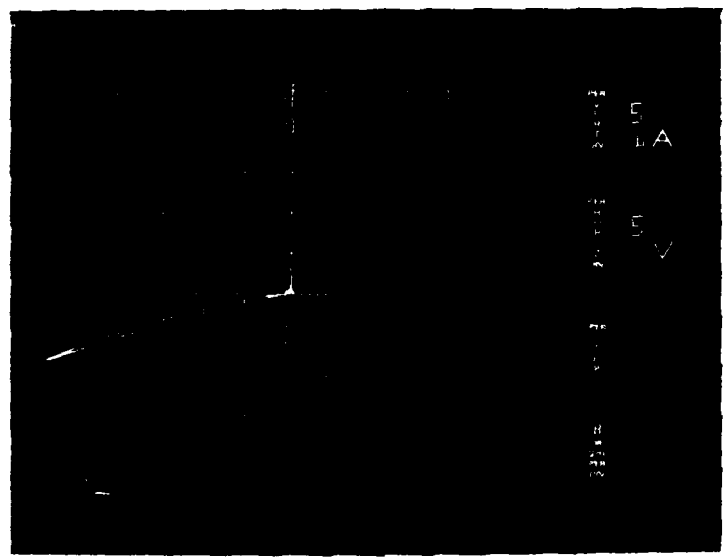


Fig. 3.10. I-V characteristic of the Be-implanted GaAs test diode.

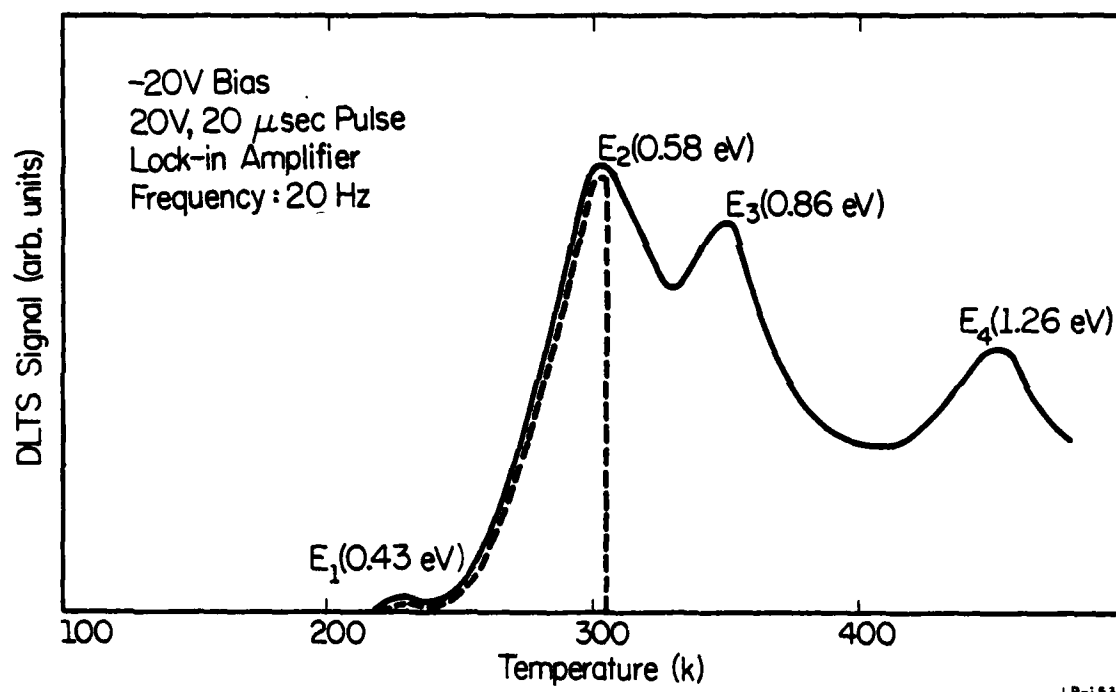


Fig. 3.11. DLTS spectra of the test diode, having an I-V characteristic as shown in Fig. 3.10. The solid curve, obtained by using the two-diode system, indicates that there are four deep levels. The dashed curve, obtained by using the system of Fig. 3.2 shows that the capacitance meter moves off scale due to the large diode leakage current.

undamaged VPE material [22]. The dashed curve in Fig. 3.11 is the DLTS spectrum using the system which employs a Boonton 72B capacitance meter. This meter will not stay balanced on the 1 pF scale and runs off scale during the temperature scan. Although the capacitance transient is only of the order of 0.01 pF, the leakage current prohibits the capacitance bridge from remaining balanced. If the third system is used, a spectrum similar to that of the two-diode system is obtained, but the position of each peak depends on the temperature at which the bridge was initially balanced. Also, the magnitude of each peak is not reproducible. This phenomenon can be explained by considering the rf mixer as a phase-sensitive detector, with the 20 MHz reference signal as the LO input. The bridge output is amplified and connected to the RF terminal. Therefore the RF input includes both the unbalance residue and the capacitance transient. Since the output of the mixer is a nonlinear function of the LO and RF inputs, the transient part of the mixer output will be proportional to the capacitance transient change of the diode only if the bridge offset is small. If, however, the offset changes significantly during the wide-range temperature scan, the transient part of the mixer output is no longer proportional to the capacitance transient. Therefore, the peak position and magnitude depend on the temperature at which the bridge is balanced initially. This is precisely the situation when a leaky diode is being tested.

A new version of a DLTS system employing a two-diode method has been examined in these experiments. Comparisons of results of this system with those of two standard systems show that the two-diode version is essential for accurate measurements on diodes having large leakage currents.

3.2 System Effects and Data Analysis

Deep Level Transient Spectroscopy (DLTS) [8] has become a wide-spread method for studying deep-level impurities and defects in semiconductors. Since several variations of the basic system are in use, it is worthwhile to compare and evaluate system effects and methods of data analysis which could affect the results obtained by different techniques. In its original concept, the DLTS system was proposed using a dual channel boxcar averager for establishing a rate window [8]. Another possibility is to use a lock-in amplifier in place of the boxcar. In either case, the most important problem is to extract the DLTS rate window from the boxcar or lock-in settings. This analysis has been presented in the literature only for rather idealized situations [8,32].

If a typical commercial capacitance meter is used to measure the transient capacitance, the relatively slow response time and consequent overloading problems of the meter make it necessary to gate-off the signal during the initial period of the transient in order to avoid spurious electrical effects due to the bias pulse. For the boxcar averager case, it is possible to avoid problems arising from this gate-off requirement by setting the first sampling instant to occur after the gate-off period. Indeed, a separate gating circuit is not even necessary with a boxcar. For the lock-in amplifier case, however, the effect of the gate-off period on the determination of the rate window must be considered. This has not been done in the past [32].

With the boxcar averager the measurements are typically made using relatively wide gates, rather than the narrow sampling periods originally proposed [8]. This is because the signal-to-noise ratio (S/N)

is better for larger gate widths. Therefore, a calculation of the rate window is needed for wide gates.

In this work we will examine these questions in detail. We will calculate the boxcar rate window for arbitrary gate widths and compare this with the simple formula originally proposed [8]. We will extend the original lock-in rate window calculations [32] to consider the effects due to the gating-off period. We find that the rate window is very sensitive to the phase setting of the lock-in. These effects are illustrated by experimental examples for the case of the Au-donor level in Si.

The DLTS system used in this work is shown in the block diagram of Fig. 3.2. A Boonton 72B capacitance meter is used to measure the transient capacitance, and either the dual-channel boxcar averager or the lock-in amplifier is used for setting the rate window.

It is necessary to gate-off the first 1-2 msec of the capacitance signal because of the 1 msec response time of the capacitance meter and the consequent overloading problems. By using the fast response gate-off circuit shown in Fig. 3.9, we can gate-off the signal for a chosen period and thus avoid baseline restoration problems.

DLTS measurements were performed using the n^+ p gold diffused junction diode with 8.0 V reverse bias and 20 μ sec pulse width.

3.2.1 Dual-channel boxcar averager

In a system employing a dual-channel boxcar averager, the transient signals are fed into the integrators with gates set at times t_1 and t_2 after the bias pulse. For very narrow gates the differential output $S(\tau)$ is simply the capacitance at t_1 minus the capacitance at t_2 :

$S(\tau) = C(t_1) - C(t_2)$. The rate window τ_{\max}^{-1} , which is the value of the thermal emission rate at the maximum of $S(\tau)$ vs. temperature (T) for a particular trap level, is then simply given by¹

$$\tau_{\max} = (t_2 - t_1) / \ln(t_2/t_1). \quad (3.1)$$

However, it is known [9] that S/N is improved with wider gate widths (w). In fact, $S/N \propto \sqrt{w}$, as would be expected for white noise. Thus, the expression for τ_{\max} must account for a finite sampling period.

The normalized output $s(\tau)$ for the case of arbitrary gate widths is given by

$$\begin{aligned} s(\tau) &= \frac{S(\tau)}{\Delta C} = [C(t_1) - C(t_2)] / \Delta C \\ &= \tau (1 - e^{-w/\tau}) (e^{-t_1/\tau} - e^{-t_2/\tau}) / w \end{aligned} \quad (3.2)$$

where $\Delta C = C(\infty) - C(0)$. The rate window is determined by differentiating $s(\tau)$ with respect to τ and setting the resulting expression equal to zero. Therefore, τ_{\max} is the solution of

$$\begin{aligned} e^{-(t_1 - t_2)/\tau} [1 + (t_1/\tau) - e^{-w/\tau} (1 + w/\tau + t_1/\tau)] \\ - [1 + (t_2/\tau) - e^{-w/\tau} (1 + w/\tau + t_2/\tau)] = 0 \end{aligned} \quad (3.3)$$

With numerical computation as shown in Appendix B the normalized emission time constant τ_{\max}/t_1 can be plotted versus normalized gate width $p = w/(t_2 - t_1)$. An example of such a computation is shown in Fig. 3.12. Since t_2/t_1 is normally kept constant during the measurement, results are plotted in Fig. 3.12 for typical values $t_2/t_1 = 5$ and 10 .

As a relatively good approximation to this exact calculation, the midpoint of the gate can be used in Eq. (1) to obtain

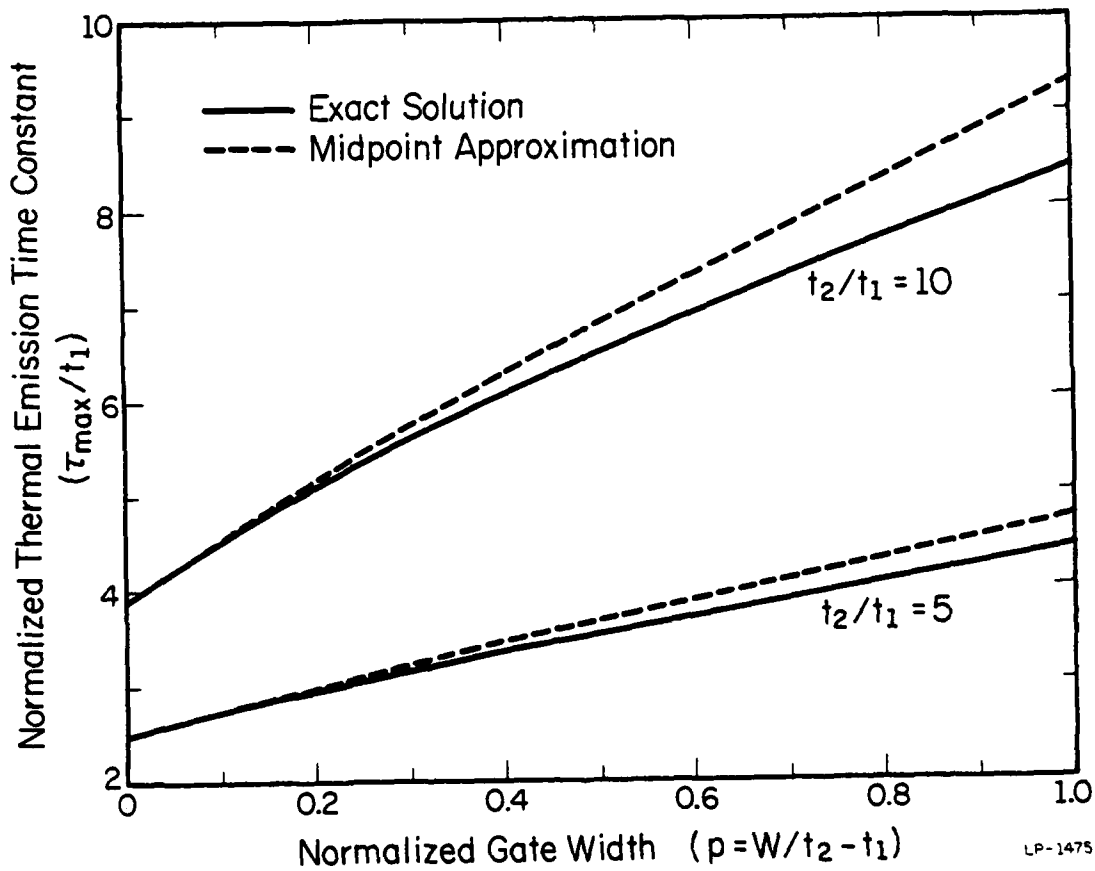


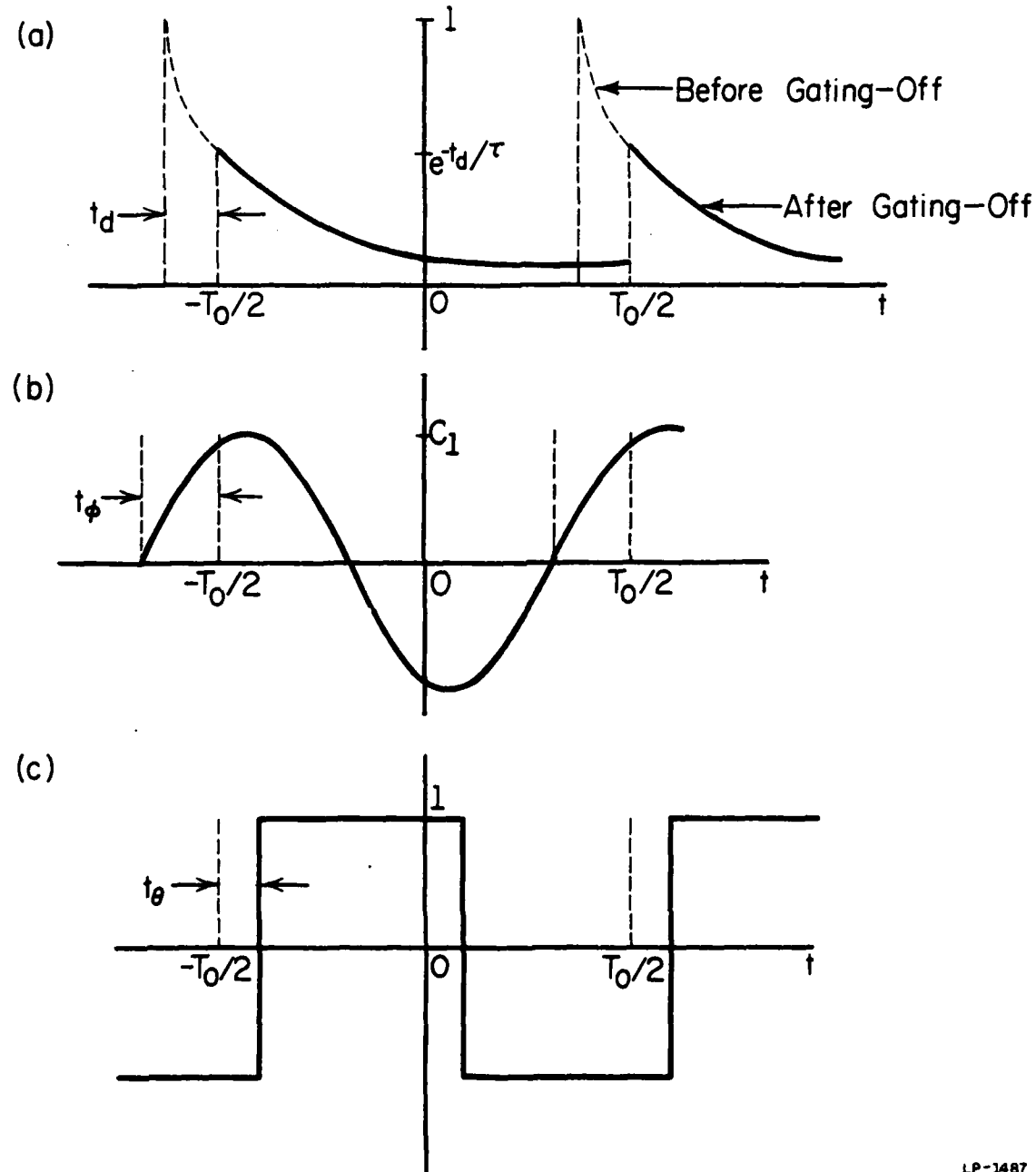
Fig. 3.12. Normalized emission time constant (τ_{\max}/t_1) plotted vs. normalized gate width p for the boxcar averager case from equation (3.3). Also shown (dashed lines) are approximations from equation (3.4).

$$\tau_{\max} = (t_2 - t_1) / \ln[(t_2 + w/2) / (t_1 + w/2)] \quad (3.4)$$

The values of τ_{\max}/t_1 obtained from this expression are plotted as the dashed curves in Fig. 3.12. It is clear that for cases chosen here, the error of this approximation is less than 10%. The effect of this approximation is to shift the DLTS Arrhenius plot by less than 2 K with essentially no change in slope.

3.2.2 Lock-in amplifier

The signal response, tuning procedure, and calculation of trap concentrations from peak heights of the lock-in amplifier output have been discussed previously [32] for the ideal case in which the system response time and overloading of the capacitance meter may be neglected. However, the apparent transient signal which is generated by the bias pulse being filtered with the response time of the capacitance meter may easily be confused with the true transient due to deep levels. It is therefore common practice to gate-off a small portion t_d of the initial portion of the transient signal. A sample-and-hold circuit may be used for this purpose as shown in Fig. 3.9. For the boxcar case such a circuit is actually redundant, since the gates may be adjusted to automatically reject the initial portion of the transient. As shown in Fig. 3.13(a), the initial value of the transient after gating-off, normalized with respect to the initial value before gating-off, is $\exp(-t_d/\tau)$. Since τ is a function of temperature, the peak value of this transient will vary during the temperature scan. Therefore, an analysis of the lock-in amplifier signal must include the gate-off time t_d . In addition, the phase setting of a lock-in amplifier fundamentally affects the signal. The PAR HR-8 lock-in amplifier used in Fig. 3.2 measures the



LP-1487

Fig. 3.13. Phase adjustment and gate-off effect in the lock-in amplifier case; (a) normalized exponential capacitance transient before and after gating-off; (b) fundamental Fourier component of the transient, $c_1 \sin(2\pi t/T_0 + \phi)$; (c) lock-in amplifier mixer weighting function for phase setting θ .

amplitude and phase of the fundamental Fourier component of the transient shown in Fig. 3.13(b). The lock-in output is the integral of the product of the square-wave weighting function in Fig. 3.13(c) and this fundamental Fourier component. The phase of the fundamental component is ϕ ; corresponding to the time $t_\phi = T_o(\phi/360)$ where T_o is the lock-in period. Similarly, the lock-in phase setting θ corresponds to the time $t_\theta = T_o(\theta/360)$.

Let us now calculate the fundamental Fourier component of the transient shown in Fig. 3.13(a). The normalized input signal after gating-off is $\exp(-t_d/\tau) \times \exp[-(t + T_o/2)/\tau]$, where T_o is the period of the lock-in and hence of the applied pulse. The Fourier expansion of a function $f(t)$ over the interval $-T_o/2 \leq t < T_o/2$ is

$$f(t) = a_0/2 + \sum_{n=1}^{\infty} [a_n \cos \frac{2\pi nt}{T_o} + b_n \sin \frac{2\pi nt}{T_o}] \quad (3.5)$$

or

$$= a_0/2 + \sum_{n=1}^{\infty} c_n \sin \left(\frac{2\pi nt}{T_o} + \phi_n \right) \quad (3.6)$$

where

$$a_n = \frac{2}{T_o} \int_{-T_o/2}^{T_o/2} f(t) \cos \frac{2\pi nt}{T_o} dt \quad (3.7)$$

$$b_n = \frac{2}{T_o} \int_{-T_o/2}^{T_o/2} f(t) \sin \frac{2\pi nt}{T_o} dt \quad (3.8)$$

and

$$c_n = \sqrt{a_n^2 + b_n^2} \quad \phi_n = \tan^{-1} \frac{a_n}{b_n} \quad (3.9)$$

For the transient in Fig. 3(a) the fundamental coefficients a_1 , b_1 , and c_1 are

$$a_1(t_d, T_o) = \exp(-t_d/\tau) \left(\frac{T_o}{2\tau}\right) \left[\exp(-T_o/\tau) - 1 \right] / \left[\left(\frac{T_o}{2\tau}\right)^2 + \pi^2 \right] \quad (3.10)$$

$$b_1(t_d, T_o) = \exp(-t_d/\tau) \pi \left[\exp(-T_o/\tau) - 1 \right] / \left[\left(\frac{T_o}{2\tau}\right)^2 + \pi^2 \right] \quad (3.11)$$

$$c_1(t_d, T_o) = \exp(-t_d/\tau) \left[\exp(-T_o/\tau) - 1 \right] / \left[\left(\frac{T_o}{2\tau}\right)^2 + \pi^2 \right]^{1/2} \quad (3.12)$$

and

$$\phi_1 = \tan^{-1} \frac{a_1}{b_1} = \tan^{-1} \frac{T_o}{2\pi\tau} \quad (3.13)$$

From an integral of the fundamental Fourier component shown in Fig. 3.13(b), described by Eqs. (3.6), (3.12), and (3.13), with the square wave in Fig. 3.13(c), the lock-in signal is

$$S(\tau) \propto \frac{\exp(-t_d/\tau)[1-\exp(-T_o/\tau)]}{\sqrt{\left(\frac{T_o}{2\tau}\right)^2 + \pi^2}} \cos(\phi_1 + \theta). \quad (3.14)$$

We may consider three basic modes of lock-in DLTS operation: namely, (1) maximum signal, (2) truncated-transient phase reference, or (3) bias-pulse phase reference. The first mode corresponds to adjusting the lock-in phase to give a maximum DLTS peak for each lock-in frequency. For $t_d = 0$, the phase setting is independent of frequency and given [32] by $\theta = -24.5^\circ$. Modes (2) and (3) are identical for $t_d = 0$ since the bias pulse coincides with the beginning of the measured transient. For $t_d \neq 0$, however, these modes are quite different.

The rate window for the maximum signal mode may be most readily

obtained from the solution of $dc_1/d\tau = 0$. Therefore, from Eq. (3.12) we see that τ_{\max} for this mode is the numerical solution to

$$\exp\left(-\frac{T_o}{\tau}\right)\left\{\left(\frac{t_d}{T_o} + 1\right)\left[\left(\frac{T_o}{2\tau}\right)^2 + \pi^2\right] + \frac{T_o}{4\tau}\right\} - \frac{T_o}{4\tau} - \frac{t_d}{T_o}\left[\left(\frac{T_o}{2\tau}\right)^2 + \pi^2\right] = 0. \quad (3.15)$$

The phase corresponding to this maximum value of c_1 vs T is given by

$$\phi_1(\tau_{\max}) = \tan^{-1} \frac{T_o}{2\pi\tau_{\max}}. \quad (3.16)$$

The truncated-transient phase reference mode corresponds to $t_\theta = 0$ in Fig. 3.13(c), i.e. the lock-in square wave zero crossing coincides with the beginning of the signal after the gating-off period. The rate window may be obtained either from $db_1/d\tau = 0$ (Eq. 3.11) or from $dS/d\tau = 0$ with $\theta = 0$ (Eq. 3.14). Choosing the latter expression for more generality, we have

$$\begin{aligned} & \exp(-T_o/\tau)\left\{\left[\left(\frac{2t_d}{T_o} + 2\right)\left(\frac{T_o}{2\tau}\right)^2 + \pi^2\right] + \frac{T_o}{2\tau}\right\}\cos(\theta + \phi_1) + \pi\sin(\theta + \phi_1)\} \\ & - \left[\frac{2t_d}{T_o}\left(\left(\frac{T_o}{2\tau}\right)^2 + \pi^2\right) + \frac{T_o}{2\tau}\right]\cos(\theta + \phi_1) - \pi\sin(\theta + \phi_1) = 0 \quad (3.17) \end{aligned}$$

The numerical solution of this expression for the case $\theta = 0$ gives τ_{\max} for this second mode of operation.

The bias-pulse phase reference mode corresponds to the lock-in zero crossing being set at the end of the bias pulse, i.e. at the true $t = 0$ point of the transient during the gated-off portion of the signal. We may use Eq. (3.17) in this case as well, with θ chosen so that $t_\theta = -t_d$ as shown in Fig. 3.13.

In this work, t_d was chosen to be 1.6 msec with the pulse frequency varying from 5 Hz to 80 Hz. The numerical solutions as a

function of lock-in frequency T_o^{-1} for normalized emission time constant τ_{max}/T_o are shown by the solid curves in Fig. 3.14 for the three methods. The dashed curves show the (frequency independent) solutions for the $t_d = 0$ case. It is clear that the errors due to ignoring the gate-off effect are significant for the first two methods, especially at high frequency where t_d/T_o is not negligible. The third method -- referencing the lock-in phase to the bias pulse -- is clearly preferable, with the frequency dependence of τ_{max} being only a few percent even for the worst case.

The magnitudes of the DLTS peaks obtained using the three methods are shown as a function of lock-in frequency in Fig. 3.15. For $t_d = 0$ there is no frequency dependence, but for a non-negligible gating-off period the effect is substantial. The DLTS peaks become uniformly smaller for increased frequency in all three methods.

The behavior of these solutions as a function of lock-in phase setting for a fixed frequency (50 Hz) is shown in Figs. 3.16 and 3.17. Figure 3.16 is a comparison of the last two methods: the truncated-transient phase reference mode where the lock-in zero crossing is after t_d , and the bias-pulse phase reference mode where the zero-crossing is before t_d . The ideal behavior occurs for $t_d = 0$ where the two methods are exactly the same. As we saw in Fig. 2.14, note again that the bias pulse method is nearly ideal for $t_d \neq 0$, whereas the method of referencing the phase to the truncated transient may introduce substantial error. Since the magnitude of this error is frequency dependent, the net effect is to skew the data on an Arrhenius plot leading to incorrect activation energies, as we shall see in the experimental example.

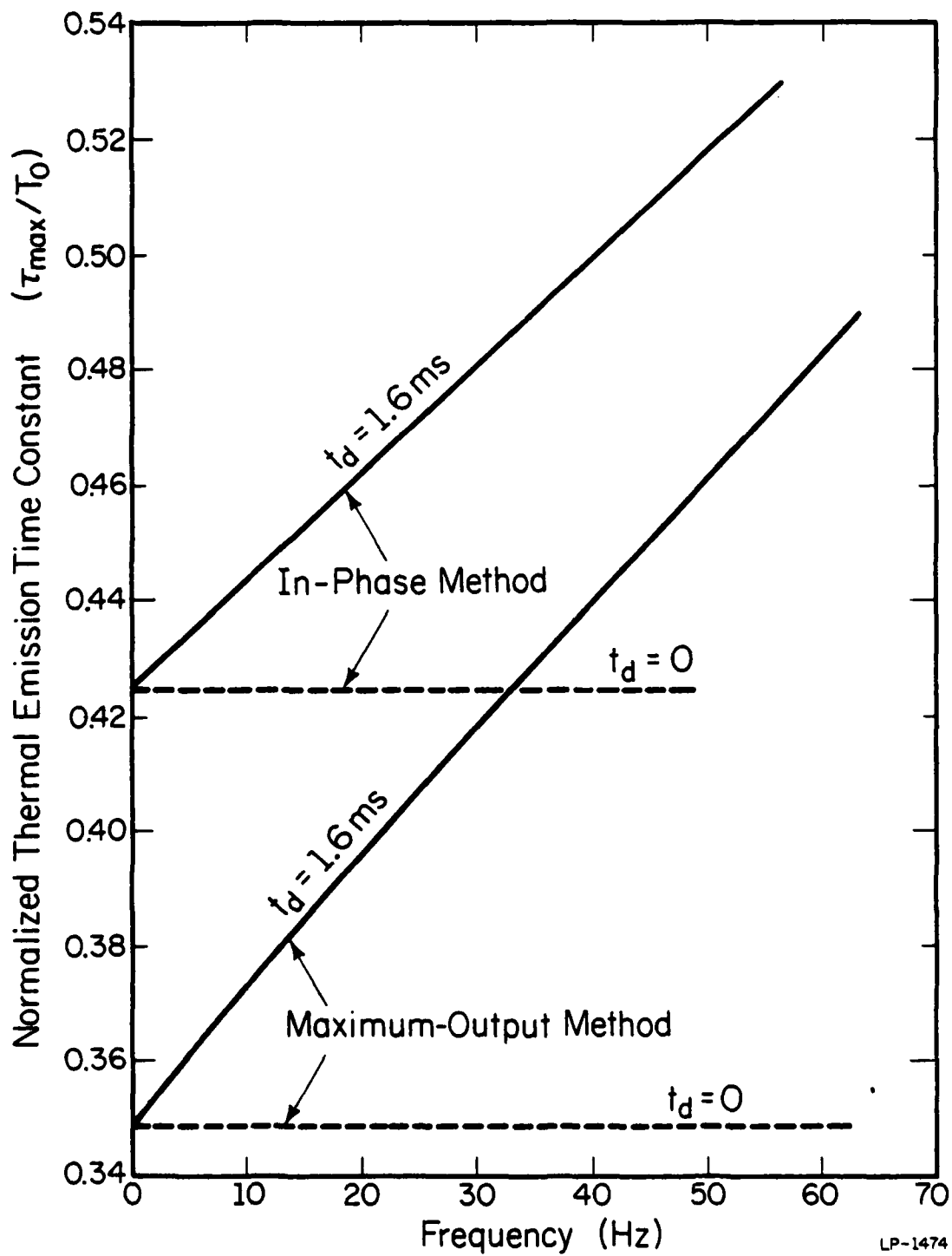


Fig. 3.14. Normalized emission time constant (τ_{\max}/T_0) vs. pulse frequency f for the lock-in amplifier case. The maximum output method refers to equation (3.15); the truncated transient phase reference method refers to equation (3.17) with $t_0 = 0$; and the bias-pulse phase reference method refers to equation (3.17) with $t_0 = -t_d$.

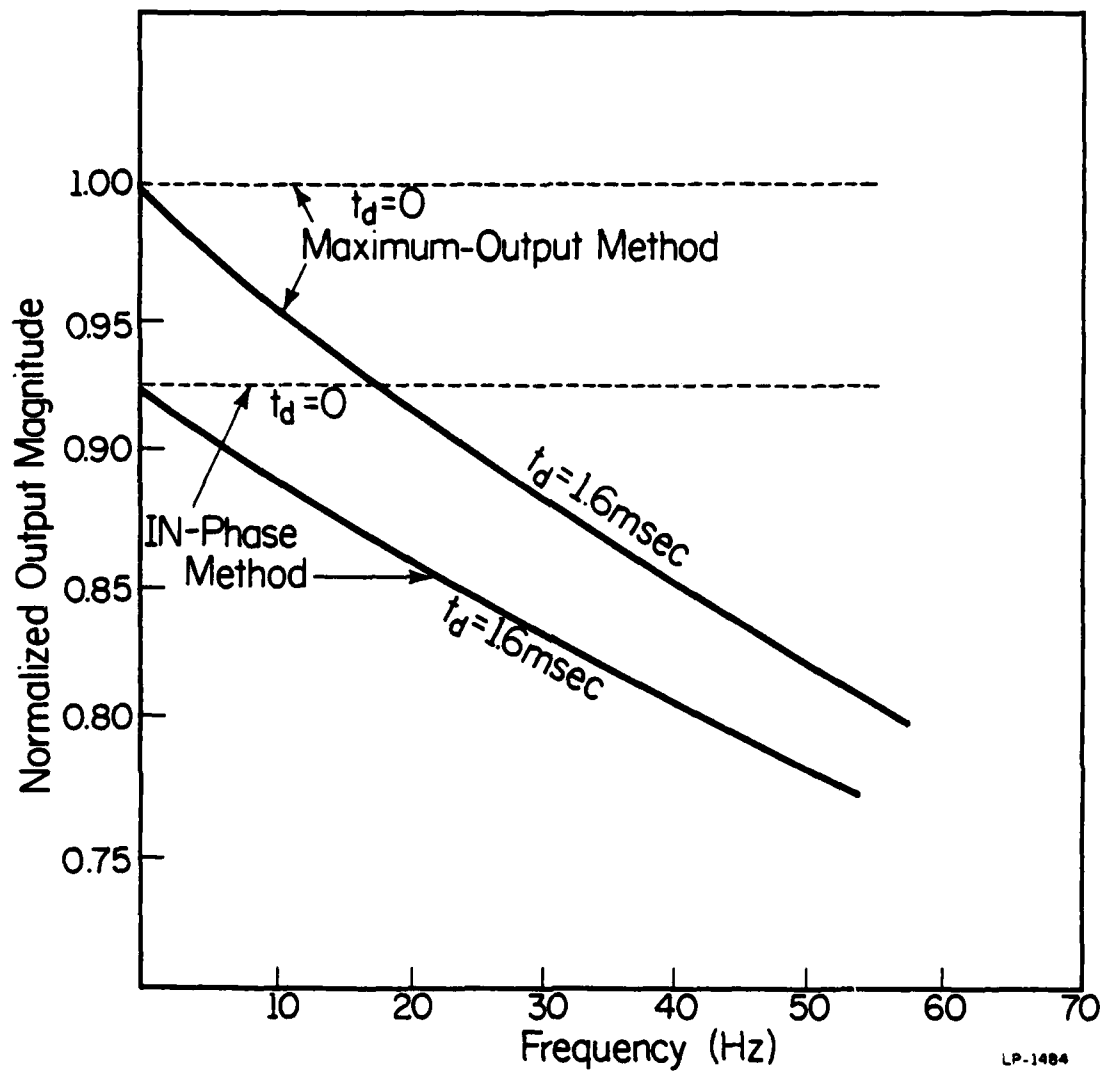


Fig. 3.15. Normalized output magnitude (equation 3.14) as a function of frequency f for the lock-in amplifier case. The three methods are the same as in Fig. 3.14. The dashed line illustrates neglect of the gate-off effect.

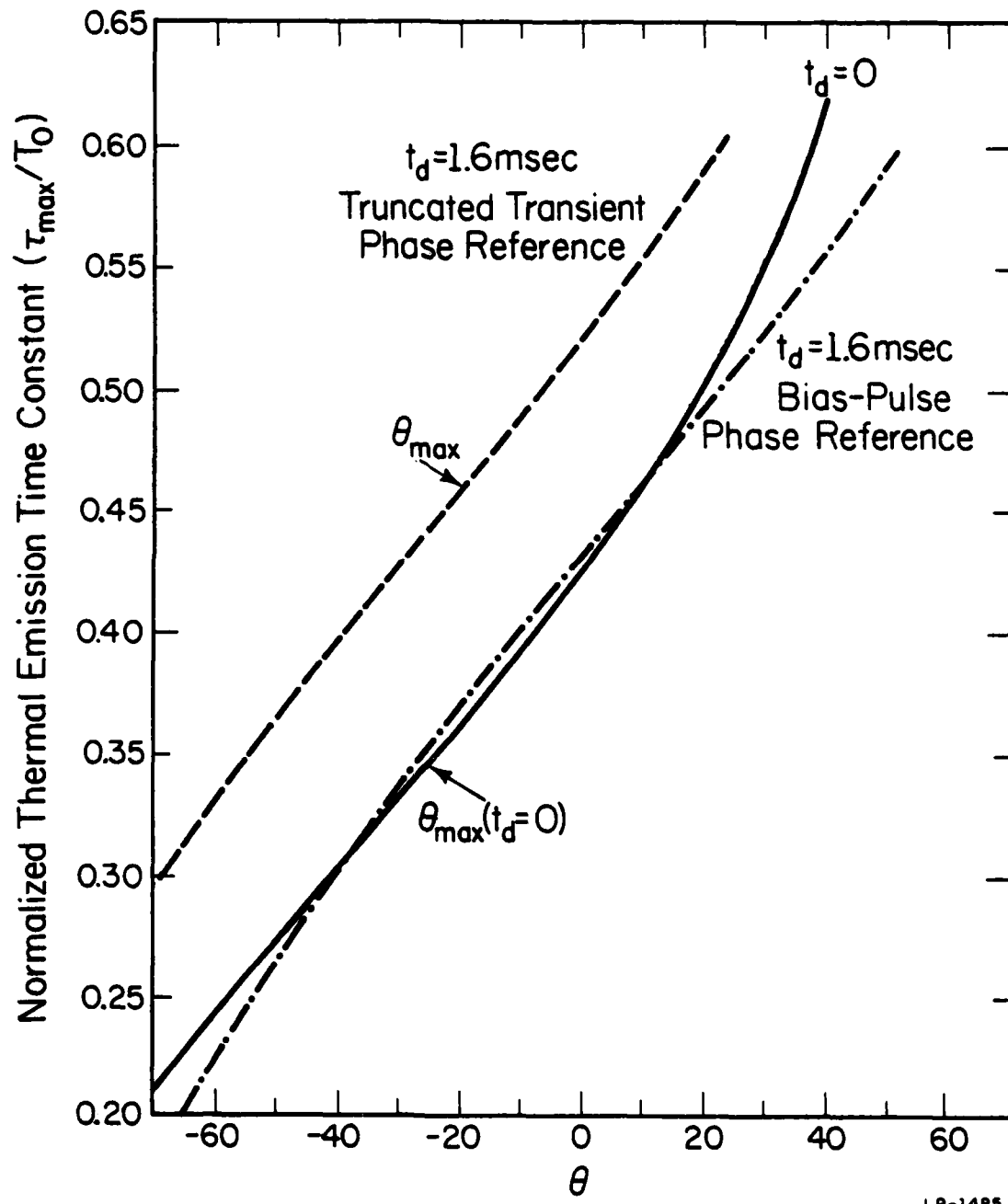


Fig. 3.16. Normalized solution of equation (3.17) for $t_d = 0$ and $t_d = 1.6\text{ msec}$ as a function of the lock-in phase setting referred to the truncated transient and to the bias-pulse methods at $f = 50\text{ Hz}$.

Even if there is little frequency dispersion in the rate window, we see in Fig. 3.16 that the proper value of τ_{\max}/T_0 is quite sensitive to the phase setting. The signal magnitude, on the other hand, is relatively insensitive to the phase setting, as can be seen in Fig. 3.17. Thus it is important that the phase be set by synchronizing the lock-in waveforms with the signal or with the bias pulses and not by merely maximizing the lock-in output signal. A 10% range in τ_{\max} will shift a typical DLTS peak by less than about 2 K. If we can consider this an acceptable error, then according to Fig. 3.16 we must set θ to within $\pm 6^\circ$ of the desired mode of operation to be within this 10% range. More demanding limits on τ_{\max} set correspondingly narrower limits on $\Delta\theta$.

Schott et. al. [32] have considered in some detail a typical phase setting routine for the maximum signal mode in the $t_d = 0$ case. Note, as shown in Fig. 3.17, however, that the required phase setting θ_{\max} for this mode in the $t_d \neq 0$ case is frequency dependent. Although the shift from 0 to 50 Hz in the $t_d = 1.6$ msec case is only 5.4° and thus within our acceptable limits of error, one should be aware that in general the phase should be reset for each frequency when using this mode. Similarly, the phase must be reset for each frequency to maintain the truncated-transient reference mode. On the other hand, the bias-pulse reference mode need be adjusted only once for all frequencies. This, coupled with the very small frequency dispersion of τ_{\max} in this mode, makes it the preferred method of lock-in DLTS operation.

3.2.3 Experimental example and discussion

In order to illustrate the various modes of DLTS operation which we have just discussed, we measured the hole-emission spectrum of

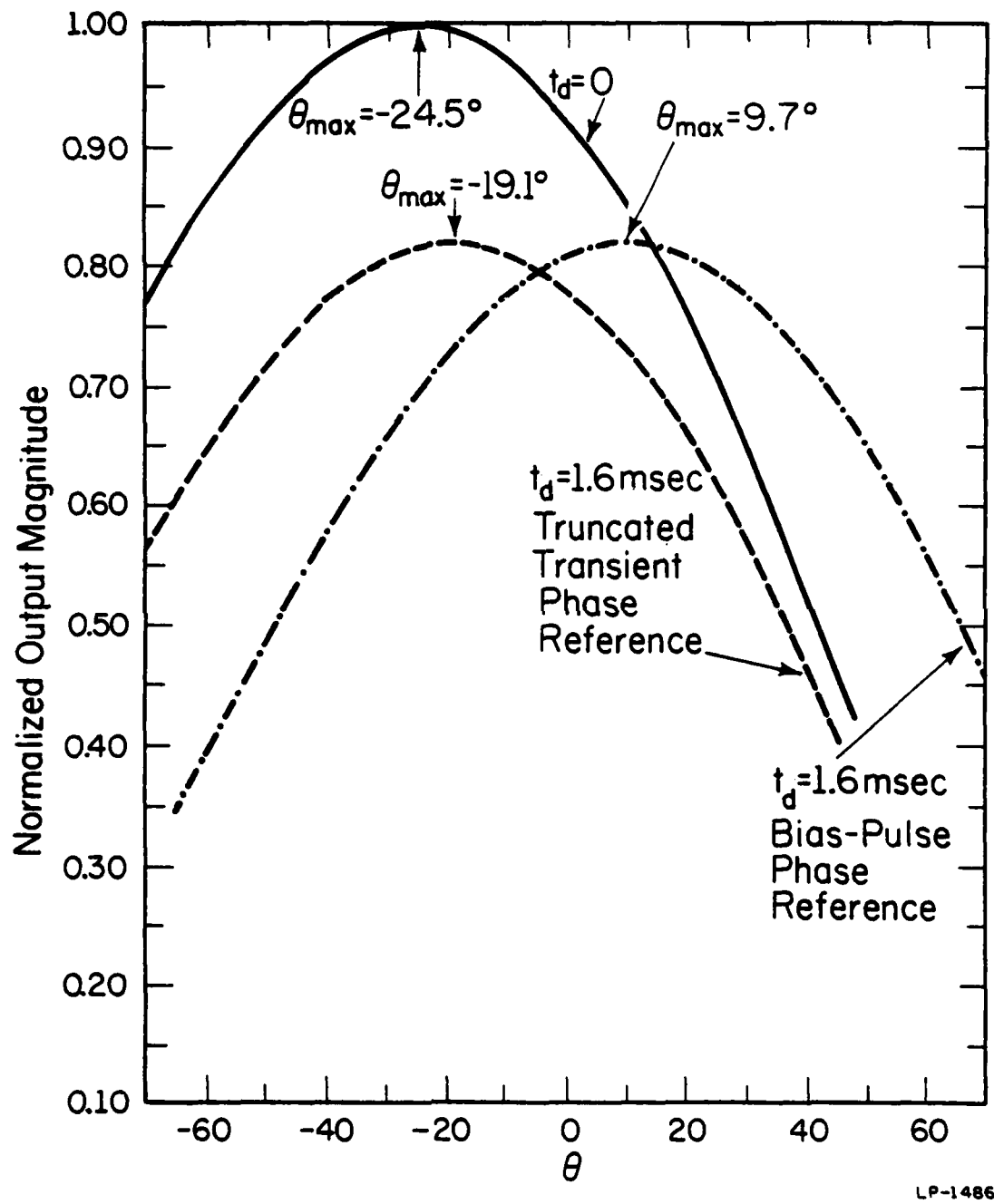


Fig. 3.17. Normalized output magnitude (equation 3.14) as a function of the lock-in phase setting referred to the truncated transient and bias-pulse methods at $f = 50\text{Hz}$.

LP-1486

the gold donor level in a silicon n^+p diode using the apparatus in Fig. 3.2. Arrhenius plots were constructed for data taken in the various operational modes according to the rate window calculation above using both the $t_d = 0$ and $t_d = 1.6$ msec relationships between τ_{max} and T_0 . For this experiment, we set $p = 0.1$ and $t_2/t_1 = 5$ for the boxcar averager and performed measurements with $f = 5, 20, 50$, and 80 Hz for the lock-in amplifier. The gate-off time was $t_d = 1.6$ msec. The τ_{max} relationship and activation energies ΔE (with T^2 correction) [9] calculated for all cases are shown in Table 3.1.

For the boxcar averager, two observations can be made from these results:

- (1) For the small setting of p and fixed value of t_2/t_1 used here, the error in τ_{max} introduced by the midpoint approximation method is negligible. The activation energy ΔE , which can be calculated from the Arrhenius plot of $T^2\tau$ vs $1/T$, is also obtained with negligible error.
- (2) For large settings of p and fixed t_2/t_1 , the error in the approximate τ_{max} is always less than 10% (Fig. 3.12). For particular values of p and t_2/t_1 , if we plot $T^2\tau$ vs $1/T$ with and without the midpoint approximation, two parallel lines result. The activation energy (proportional to the slope) is found to be the same, although the τ_{max} values are not strictly correct in the approximate method. As we noted earlier, however, the actual shift in temperature of the Arrhenius plot is typically less than 2 K.

TABLE 3.1
Comparison of the thermal emission time constant and the energy level obtained from various methods.

CASE	METHOD	τ_{\max} (msec)	ΔE (eV)
Boxcar Averager	exact solution	$2.73t_1$	0.33 ± 0.03
	midpoint approximation	$2.73t_1$	0.33 ± 0.03
Lock-in Amplifier	Truncated transient phase reference method		
	with correction	$0.424 T_o + 1.87$	0.33 ± 0.01
	without correction	$0.424 T_o$	0.36 ± 0.01
Maximum-output method			
	with correction	$0.3485 T_o + 2.28$	0.33 ± 0.01
	without correction	$0.3485 T_o$	0.38 ± 0.03
Bias-pulse phase reference method			
	with correction	$(0.424 + 6) T_o$	0.33 ± 0.01
	without correction	$0.424 T_o$	0.34 ± 0.01

For the lock-in amplifier case, several observations can be made:

- (1) A large error in the τ_{\max} values due to the neglect of the $e^{-t_d/\tau}$ is expected from Fig. 3.14 for the maximum output and truncated-transient reference cases. The plot of $T^2\tau$ vs $1000/T$ for the maximum output method (Eq. 3.15) are shown in Fig. 3.18 for both the $t_d = 0$ and $t_d = 1.6$ msec values of τ_{\max} . The data points plotted from uncorrected τ_{\max} values ($t_d = 0$) deviate somewhat from a straight line. The comparison of corrected and uncorrected data shows that in this case it is absolutely necessary to consider the gate-off effect in order to obtain the true activation energy and emission time constant.
- (2) For the bias-pulse phase reference method, it is expected that the error introduced by using the uncorrected thermal emission time constants in the activation energy calculation should be small. As shown in Table 3.1, this discrepancy is actually within the experimental error.
- (3) The peak value of the lock-in amplifier output is expected to decrease with increasing frequency (Fig. 3.15). Such a frequency variation is found experimentally. If the gate-off effect were truly negligible, the peak value should instead be independent of pulse frequency. This illustrates that the output magnitude should be corrected in the calculation of trap concentration, especially for higher frequencies.
- (4) The phase adjustment is critical for the lock-in amplifier as discussed in connection with Fig. 3.16. The bias-pulse

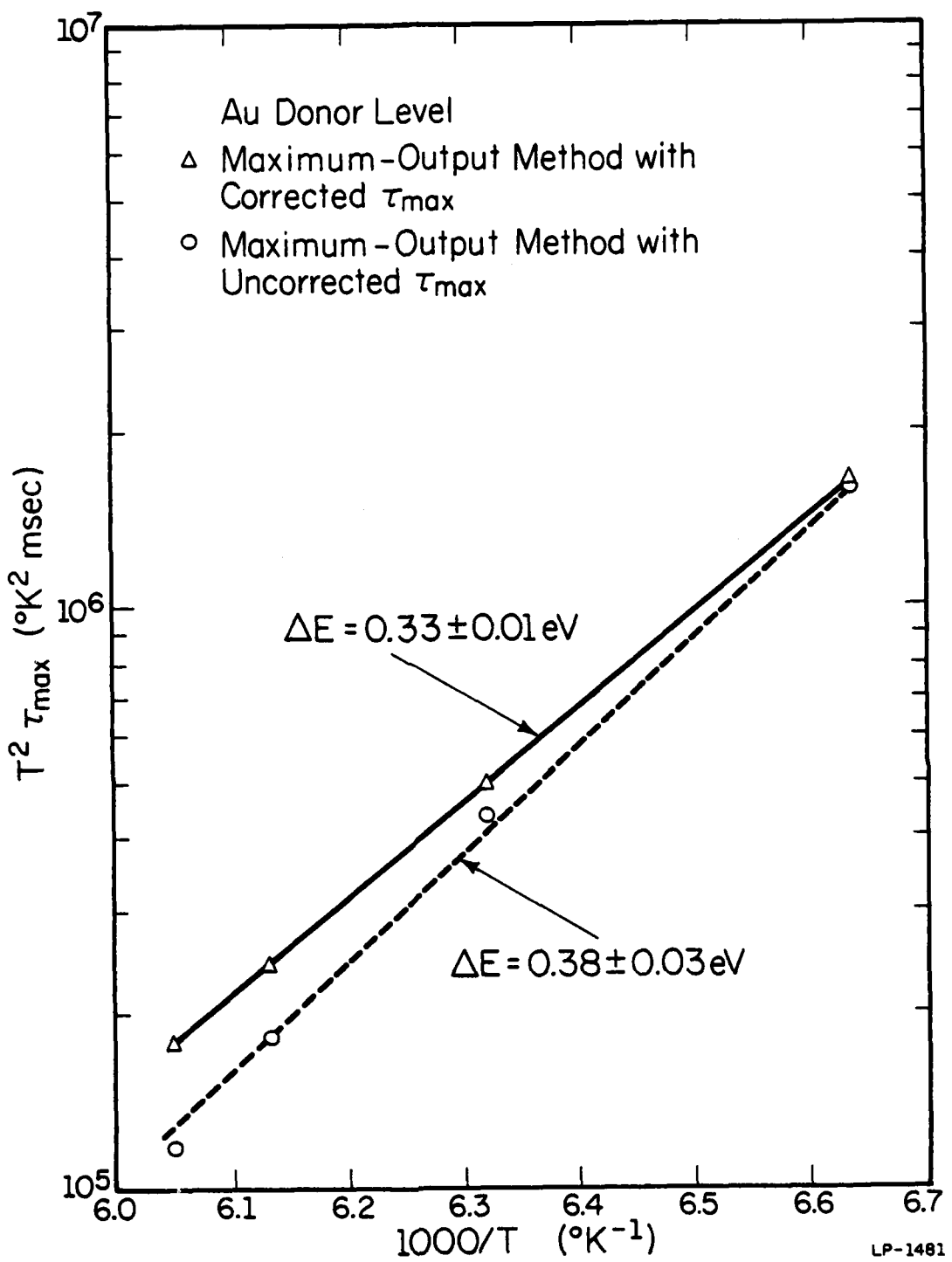


Fig. 3.18. Arrhenius plot of $T^2 \tau_{\max}$ vs. $1000/T$ obtained for the gold donor level in an n^+p silicon junction with and without the correction for maximum-output method.

reference method involves much simpler phase settings than either of the other two methods and hence introduces less error. Since this method also needs practically no correction to τ_{\max} , it is clearly the method of preference for the lock-in methods.

We see also that the boxcar and lock-in methods of DLTS are quite comparable, both in complexity and in accuracy. The boxcar method is not subject to spurious recovery effects in the initial portion of the transient, but it is somewhat complex to change the gates for different rate windows. Using the lock-in method with bias-pulse phase reference, it is relatively simple to change rate windows; however, the phase must be accurately adjusted and the initial recovery problem must be dealt with. Both methods yield comparable S/N if the boxcar is used with wide gates. Thus neither stands out above the other as the "best" method. In the end, the choice of a rate window system must be based primarily on personal preference and on the best utilization of existing equipment.

3.2.4 Summary

The DLTS systems based on either a dual-channel boxcar integrator or a lock-in amplifier are analyzed for realistic experimental conditions. We present expressions which may be numerically solved to yield the DLTS rate window for cases of arbitrarily wide boxcar gates and for gating-off of the initial portion of the transient in the lock-in case. Solutions for typical experimental parameters show that the boxcar rate window may be adequately approximated by Lang's original expression applied to the midpoints of the gates. We find that the lock-in DLTS systems are in general critically sensitive to the phase setting and

and analyze in detail three possible modes of operation: (1) maximum signal, (2) phase referenced to the beginning of the truncated transient, and (3) phase referenced to the bias pulse. The first two methods show considerable shifts in the rate window relationship τ_{\max}/T_0 as a function of lock-in frequency when the initial portion of the transient is gated-off to avoid overload and recovery time effects. The third method is much less frequency sensitive and thus is clearly the best choice for those who prefer lock-in operation. These concepts are illustrated by DLTS measurements of the hole-emission spectra of the gold donor level in silicon n^+p diodes. The data show that a naive analysis of the first two modes of lock-in operation yields activation energies which are seriously in error. With proper analysis, however, all DLTS methods produce identical results.

4. STUDIES OF ELECTRON TRAPS IN THE GaAs-GaP SYSTEM BY DEEP LEVEL TRANSIENT SPECTROSCOPY

4.1 Studies of Electron Traps in GaAs

It has been reported [22] that there are six electron traps in device quality VPE n-GaAs. These are discussed in two review papers [52, 53] dedicated to the signatures of deep levels in epitaxial GaAs. An electron trap with thermal activation energy of 0.83eV from the conduction band is the dominant one and is consistently reported in DLTS work [23,55]. It has been conjectured that this dominant level is related to oxygen impurity atoms on arsenic sites, [56-58] or that it is related to the Ga vacancy [23]. Although there have been numerous studies of this level, a positive identification of the responsible defect has been lacking. In this study we report detailed experimental results which will contribute significantly to the understanding and identification of this deep level.

4.1.1 Material preparation and device fabrication

All of the VPE n-GaAs (100) material used in this work was provided by the Monsanto Company (St. Louis). The epitaxial layer thickness is about $10\mu\text{m}$. Shown in Fig. 4-1 is the net donor concentration profile of the undoped n epitaxial layer, obtained from C-V measurement. The depth is calculated from Eq. (2.5) and the capacitance is obtained from an Al-gate Schottky barrier with an area of $1.30 \times 10^{-3} \text{ cm}^2$ (16mils dia.). The concentration is assumed to be a constant value of $1.2 \times 10^{15} \text{ cm}^{-3}$ in this study. Two wafers from the same growth run (Monsanto 1-1138) are used in this study, and we find that these two wafers are essentially identical in terms of net donor concentration and the main trap concentration.

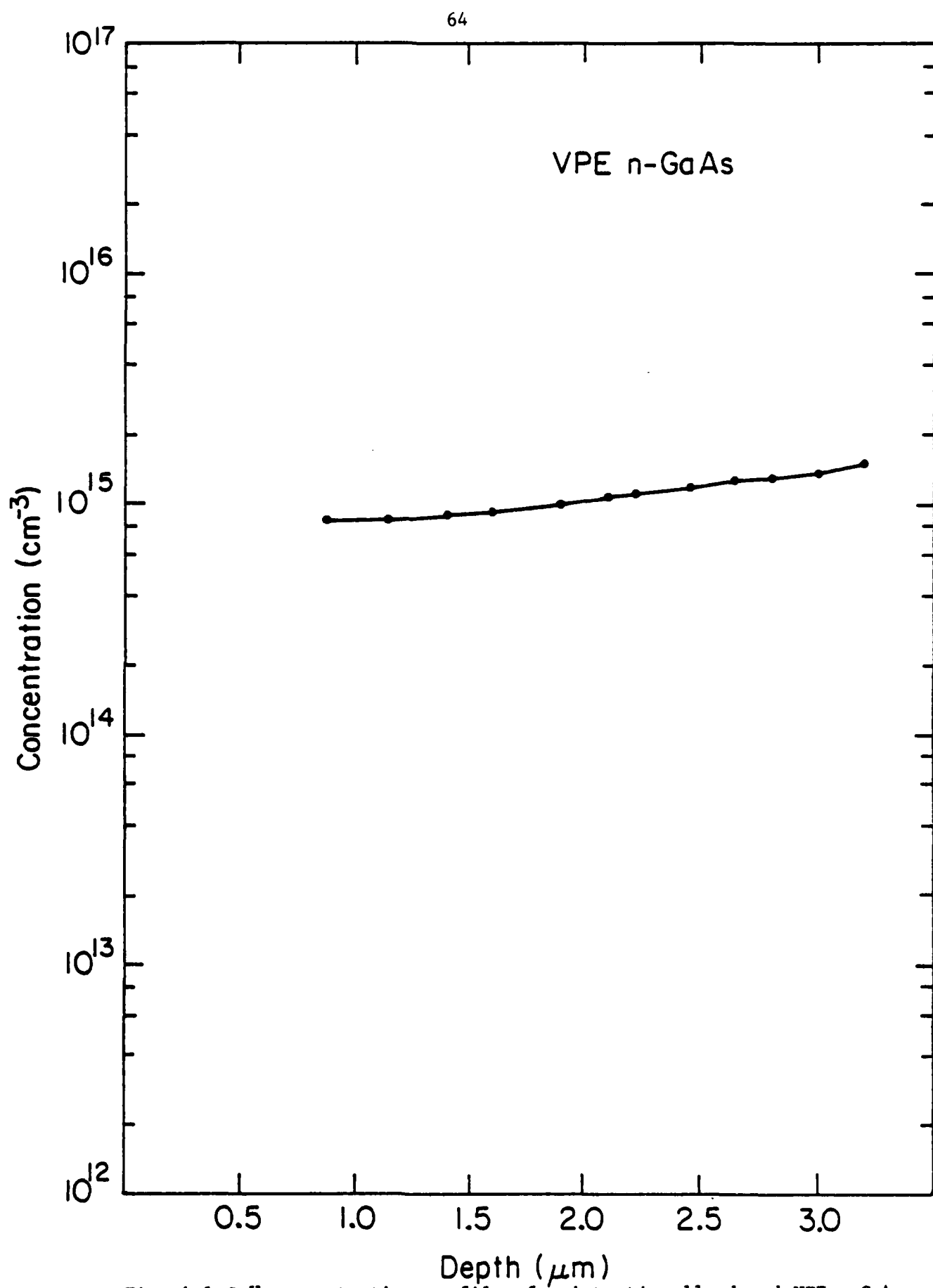


Fig. 4.1 C-V concentration profile of unintentionally doped VPE n-GaAs.

Liquid phase epitaxial (LPE) n-GaAs material was provided by Dr. R. Milano and Professor G. E. Stillman of the University of Illinois at Urbana-Champaign. The LPE epitaxial layer, on an n^+ GaAs substrate, had a net donor concentration of about $2 \times 10^{15} \text{ cm}^{-3}$. The molecular beam epitaxy (MBE) n-GaAs used in this study was grown by Professor H. Morkoç at the Coordinated Science Laboratory in this university and had a net donor concentration of $1 \times 10^{15} \text{ cm}^{-3}$.

An Al layer of $1000 \text{ \AA} \sim 2000 \text{ \AA}$ thickness is evaporated to make Schottky barriers on epitaxial n-GaAs. Ag-Sn eutectic alloy is evaporated on the n^+ substrate and sintered at $\sim 350^\circ\text{C}$ for 30 sec for ohmic contact. Two Schottky barriers are cleaved from the same sample and are mounted on the same T0-18 or T0-5 header in the DLTS set-up with the two-diode method described previously.

The I-V characteristics of a typical Schottky barrier on VPE n-GaAs is shown in Fig. 4.2. The forward I-V characteristic is shown with scales of 0.5 V/div horizontally and 0.1 mA/div vertically. The reverse I-V characteristic has scales of 10V/div horizontally and $5\mu\text{A}/\text{div}$ vertically.

4.1.2 Electron Traps in VPE n-GaAs

As mentioned in Chapter 2, either a dual-channel boxcar averager or a lock-in amplifier can be used in the DLTS system to preset the rate window. For signals much less than 100mV, the lock-in amplifier is better than the boxcar averager in terms of S/N ratio due to the maximum sensitivity of 100mV in the boxcar averager. The gate-off effect discussed in Chapter 3 is negligible in this case because of the fast response time of $1 \sim 2\mu\text{sec}$ in our DLTS system. Therefore, a lock in amplifier is preferred

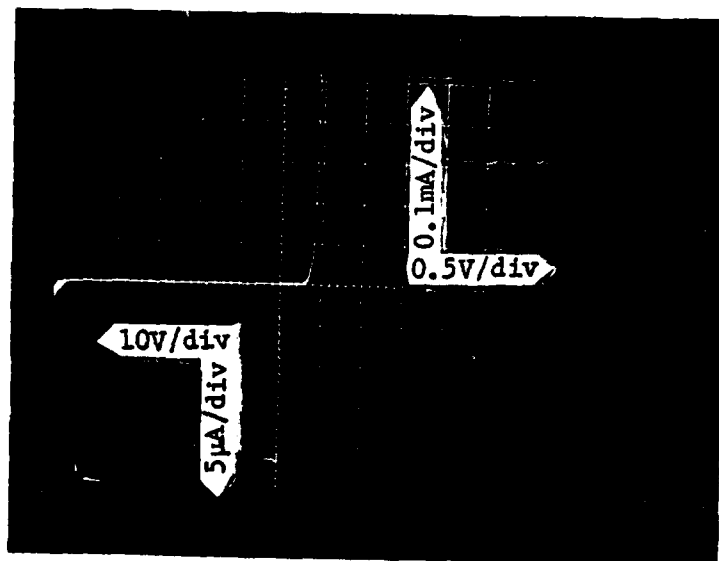


Fig. 4.2 I-V characteristics of a typical Schottky barrier on VPE n-GaAs.

in this study and the bias-pulse phase reference mode (which is the same as the truncated transient phase mode) is used. The thermal emission time constant and trap concentration calculations are therefore based on this mode. The lock-in amplifier phase is adjusted to show a positive DLTS signal for a majority carrier trap and a negative signal for a minority carrier trap.

Shown in Fig. 4.3 is the DLTS spectrum of electron traps in VPE n-GaAs. The DLTS signal is expressed in terms of trap concentration calculated from Eq. (2.16) by assuming that each trap is uniformly distributed throughout the observed layer. Here the symbol V designates VPE material, and similarly L and M stand for LPE and MBE later in this chapter. The electron trap V7 is dominant in VPE n-GaAs. The other traps are present in only very small concentrations and appear only accidentally. Therefore, it is hard to conduct a systematic experiment to understand the physico-chemical origins of traps other than V7.

The thermal activation energy for each trap is obtained from the slope of the Arrhenius plot of $T^2 \tau$ vs $1000/T$ shown in Fig. 4.4. The least-square-fit program to calculate activation energy for either a boxcar or a lock-in case is presented in Appendix C.

The concentration profile of the main electron trap V7 is shown in Fig. 4.5, and the depth is obtained from Eq. (2.5). The concentration in the observed layer obtained from two pulses of different amplitude is calculated according to Eq. (A7) in the appendix of Ref. 50.

This equation can be simplified to

$$\delta \left(\frac{\Delta C}{C} \right) = \frac{1}{2} \frac{N_{TT}}{N_D} + \left(\frac{\delta V}{V_R + V_{bi}} \right) \quad (4.1)$$

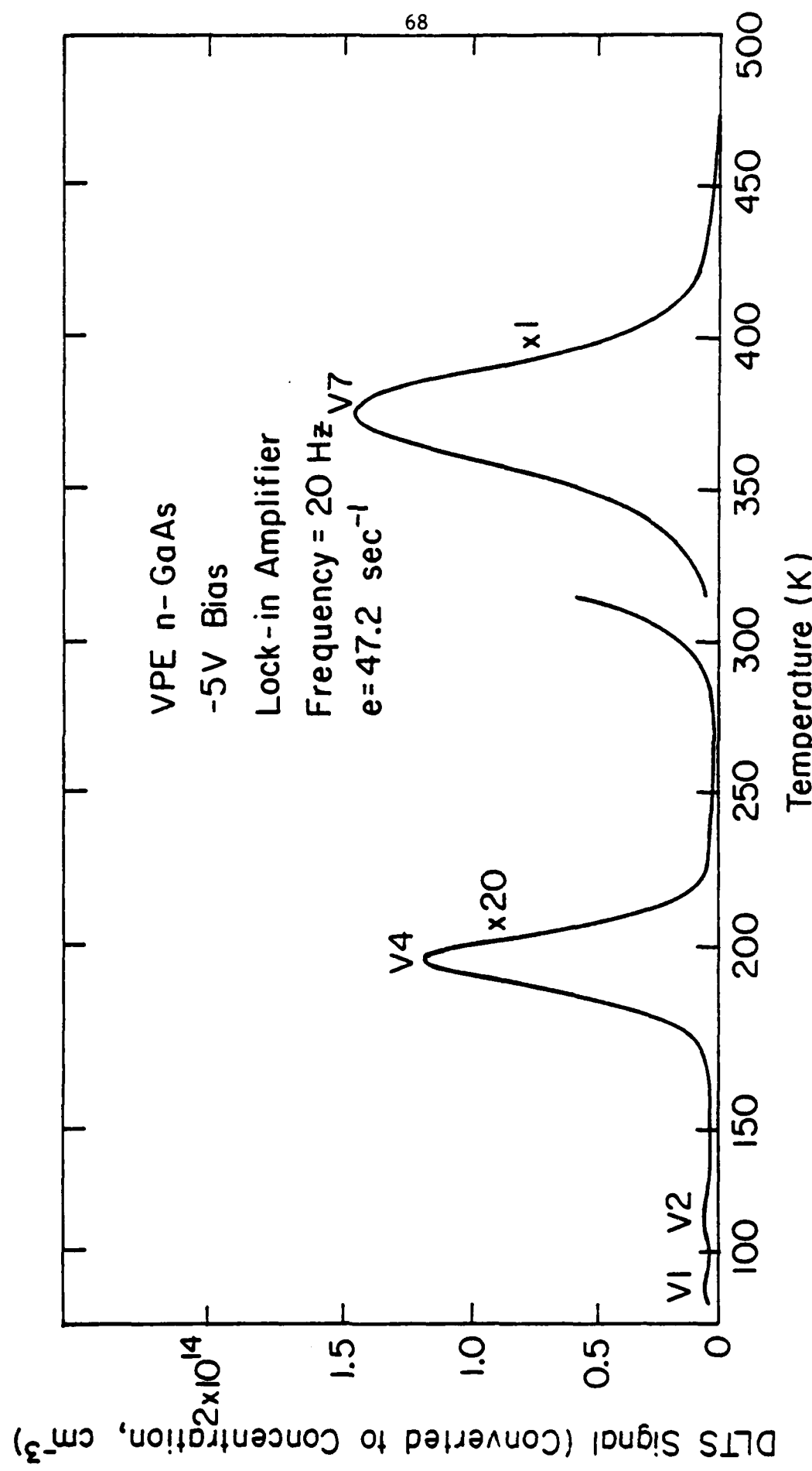


Fig. 4.3 DLTS spectrum of electron traps in VPE n-GaAs.

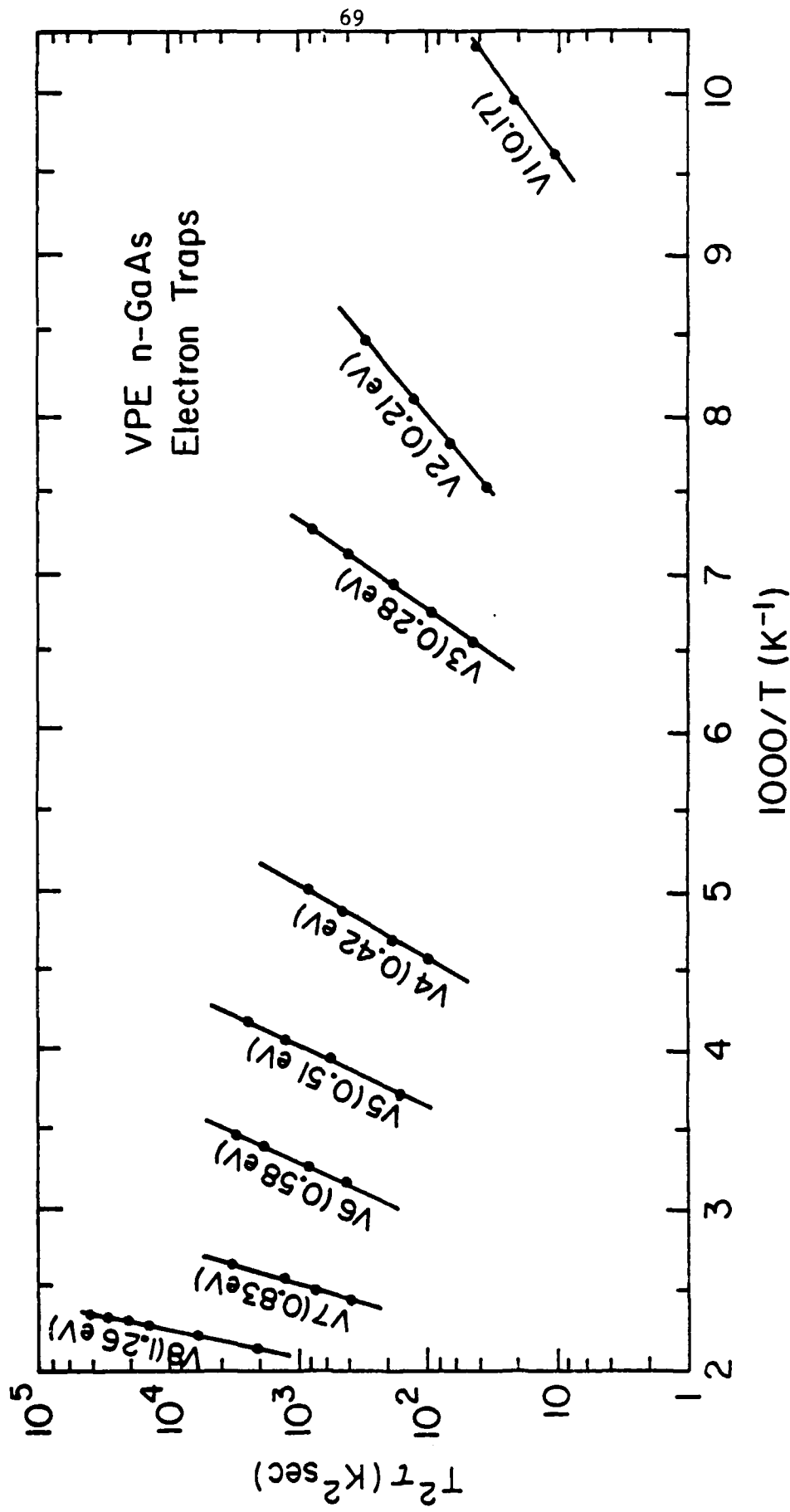


Fig. 4.4 Arrhenius plots of $T^2 T$ vs. $1000/T$ for electron traps in VPE n-GaAs under various experimental conditions.

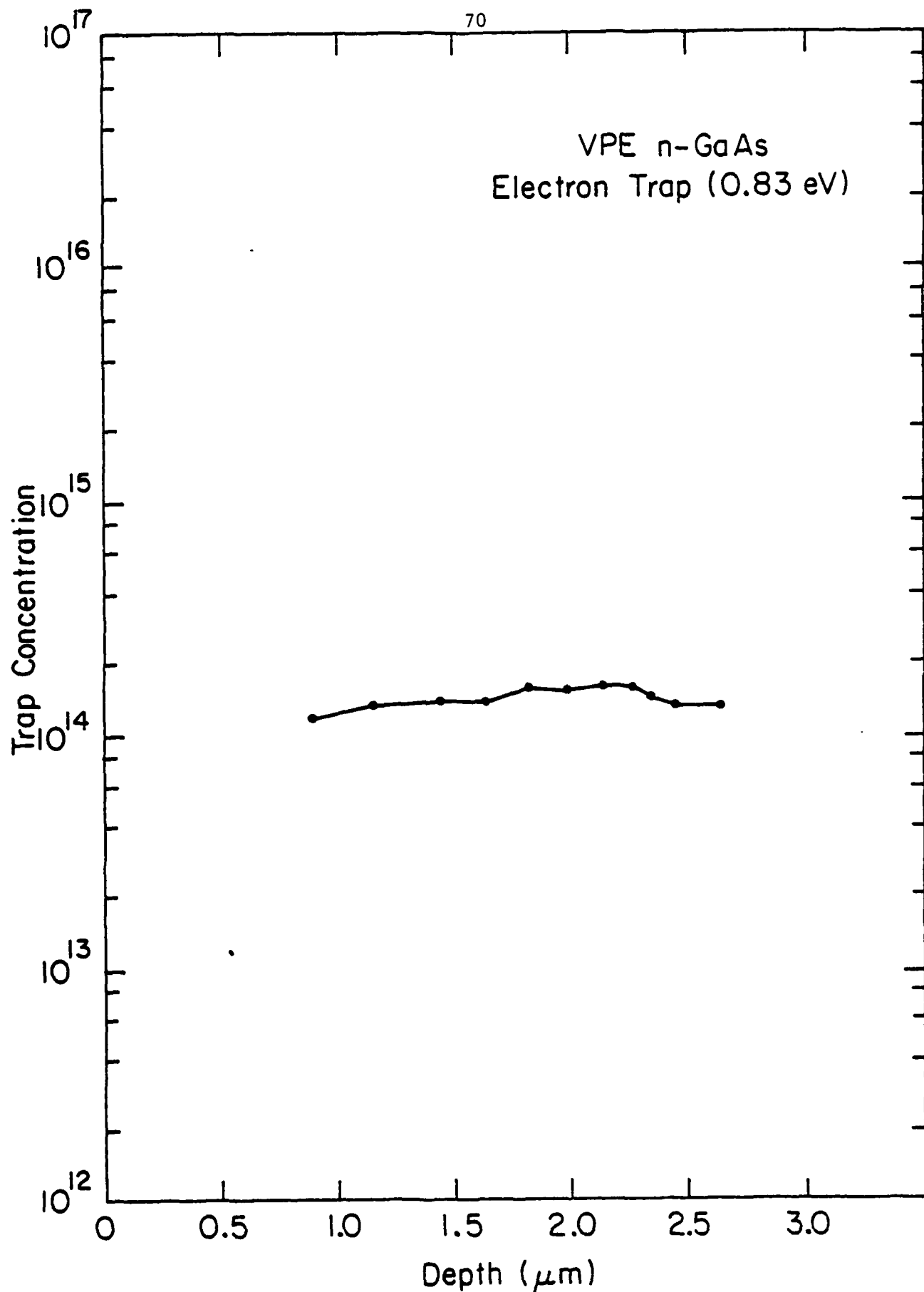


Fig. 4.5 Concentration profile of the main electron trap (0.83 eV) in VPE n-GaAs.

if the net donor concentration N_D^+ is assumed constant and the trap concentration in the small layer is taken as constant. The symbol δ denotes a small variation or change in the following parameter. In the calculation the built-in voltage V_{bi} is assumed to be 0.65 V, calculated from the relation [59]

$$V_{bi} = V_B - (E_c - E_{Fs})/e \quad (4.2)$$

where V_B is the barrier height and E_{Fs} is the Fermi-level in semiconductor. As shown in Fig. 4.5, the trap concentration can be assumed to be a constant value of $1.4 \times 10^{14} \text{ cm}^{-3}$.

The capture cross section for each trap at the observed temperature can be calculated from the thermal emission rate measurement by Eq. (2.13). The capture cross section for each trap calculated from the emission rate measurement is listed in Table 4.1 by assuming $m^* = 0.065 m_e$, $m_{dn} = 0.068 m_e$, and $g = 1$ where m_e is the electron mass. The capture cross section σ_a in Eq. (2.13) of $1.3 \times 10^{-13} \text{ cm}^{-2}$ for trap V7 is in good agreement with that reported by Mircea [22].

The capture cross section can also be obtained from the thermal capture rate measurement as discussed in detail in Sec. 2.3.4. Shown in Fig. 4.6 is a typical example taken from the VPE n-GaAs sample. The capture rate is determined from the DLTS peak heights as a function of the majority carrier pulse duration. Here, a Systron-Donner SD-110C pulse generator with pulse transition time of 5nsec is used. A pulse width of 1 μ sec is long enough to fill up this trap. In order to be sure that no competition of carrier capture from other traps takes place, a pulse of 20 μ sec duration is always used in the emission rate measurements in this study. From Eq. (2.15) we estimate that the carrier capture time con-

Table 4.1. Thermal Activation Energies and Capture Cross Sections of Electron Traps in VPE n-GaAs.

Trap	Activation Energy ΔE (eV)	Capture Cross- Section σ_∞ (cm^2)	Temperature Range (K)
V1	0.17	5×10^{-14}	95-105
V2	0.21	1.0×10^{-14}	115-135
V3	0.28	1.7×10^{-13}	135-155
V4	0.42	1.8×10^{-13}	190-220
V5	0.51	1.1×10^{-13}	240-270
V6	0.58	1.7×10^{-14}	280-330
V7	0.83	1.4×10^{-13}	370-420
V8	1.26	7.5×10^{-11}	425-470

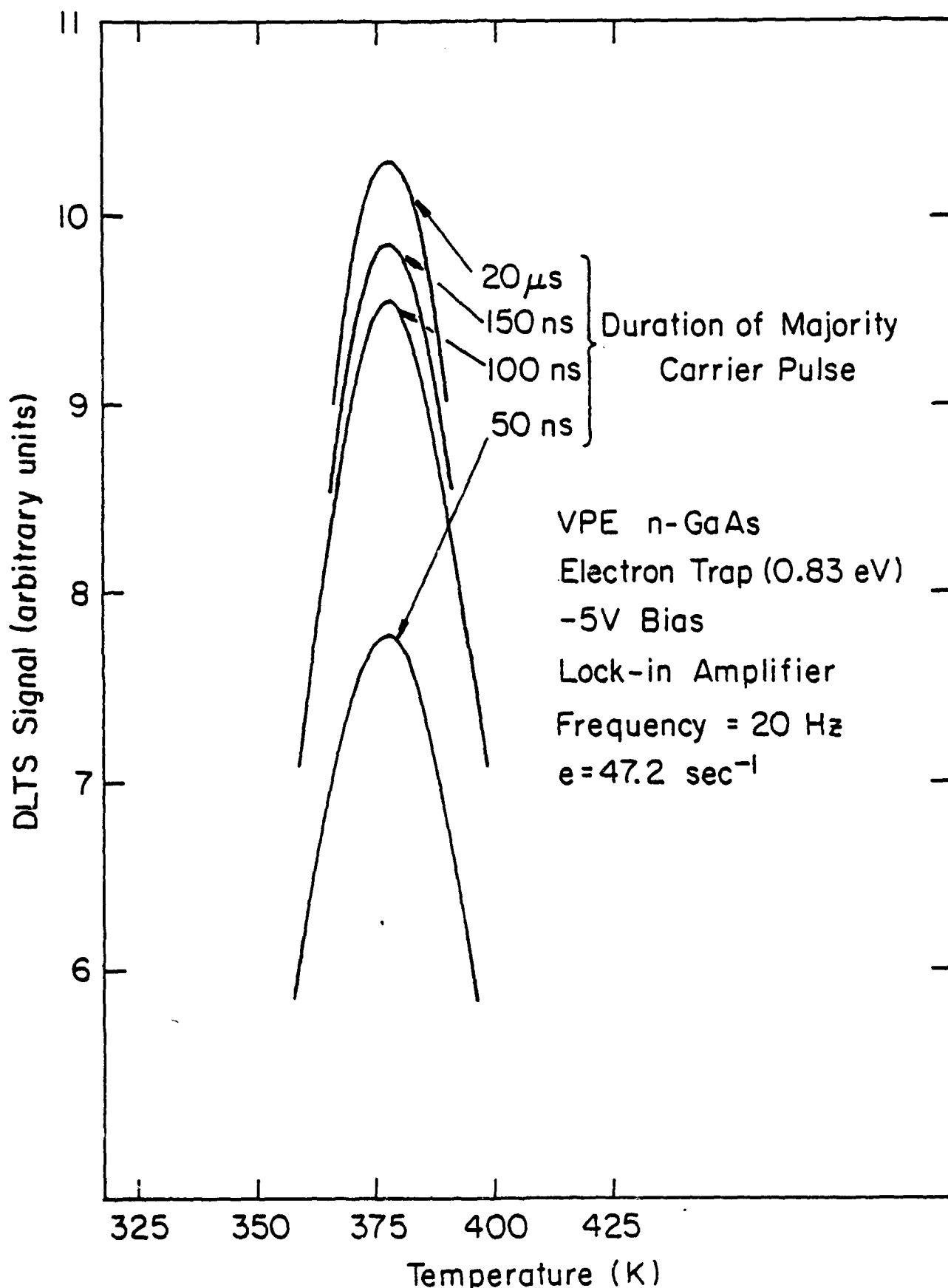


Fig. 4.6 Typical example of the dependence of trap peak heights on the duration of the majority carrier pulse.

stant for V7 is about 40nsec. Therefore, the capture cross section from the capture rate measurement at the observed temperature (378°K) is estimated to be $4 \times 10^{-16} \text{ cm}^2$. This value is in good agreement with that reported by Henry and Lang [33,58]. They observed an exponential temperature dependence of the capture cross section and estimated the capture activation energy W_σ to be $\sim 0.08 \text{ eV}$. Henry and Lang explained the strong temperature dependence by multiphonon emission (MPE) in which the energy is conserved via lattice relaxation. The capture cross section σ_n at the observed temperature is estimated from the emission rate measurement to be $1.1 \times 10^{-14} \text{ cm}^2$ from Eq. (2.12) for $\sigma_\infty = 1.3 \times 10^{-13} \text{ cm}^2$. Hence, there is a large difference between the capture cross sections obtained from capture rate and emission rate measurements. Mircea et al. [60] tried to explain this discrepancy by artificially introducing a temperature coefficient α in addition to W_σ such that

$$\Delta E = E_c - E_T + W_\sigma - \alpha T \quad (4.3)$$

This argument is not convincing, and has been challenged by Majerfeld et al [61]. They proposed that the transition occurs between the valence band the the L minimum instead of the Γ minimum. It has been reported [62] that photocapacitance measurements on GaAs under hydrostatic pressure suggest the dominance of optical transitions from trap levels to higher lying L and X minima rather than the Γ minimum. It has also been reported [63] that the hydrostatic pressure dependence of ΔE for the 0.83eV trap in GaAs as derived from thermal emission rate measurements is $3.8 \pm 0.3 \text{ meV/kbar}$. This value together with the value of $1.7 \pm 1 \text{ meV/kbar}$ obtained for optical transitions from the trap level to

the valence band [64] gives a pressure dependence of 5.5 ± 1.3 meV/kbar from the valence band to the final transition state. This suggests that the final transition state is in the L minimum rather than the Γ minimum. Majerfeld et al [61] estimated that the energy depth from trap level to the Γ minimum is about 0.54eV, using conventional C-V measurements. It has been shown that the energy separation between the L and Γ minima in GaAs is 0.29 ± 0.01 eV at 300°K [65]. The thermal activation energy of 0.83eV observed in DLTS emission rate measurements suggests that the transition is from the trap level to the L minimum. If this is true, then the effective mass values $m^* = 0.11 m_e$ and $m_{dn} = 0.55 m_e$ [33] for the L minimum should be used. The spin degeneracy g_n can be taken as 1/2 [66]. Therefore Eq. (2.13) becomes

$$e_n = 3.26 \times 10^{21} \times \frac{\left(\frac{m_{dn}}{m_e}\right)^{3/2}}{\left(\frac{m^*}{m_e}\right)^{1/2}} g_n \sigma_n T^2 \exp[-(E_c - E_T)/k_B T]$$

$$= 2.40 \times 10^{15} \sigma_n T^2 \exp(-0.83/k_B T)$$

From the observed emission rate and the corresponding temperature T, σ_n is estimated to be $1.9 \times 10^{14} \text{ cm}^2$. This value is in good agreement with that extrapolated at $T = \infty$ by Henry and Lang [33]. Here we do not use the correcting factor W_σ for the capture cross section. The capture cross section σ_n is about the same as σ_∞ obtained by Henry and Lang [33]. Therefore, the capture cross section does not have a temperature dependence. The apparent temperature dependence of the capture cross section obtained by Henry and Lang is due to their assumption that the available free carriers during capture are from the Γ minimum and with a value of net doping for a small trap concentration. Majerfeld et al [61] proposed that

the capture and emission processes are via the L minimum. The available free carrier concentration in the L minimum relative to that in Γ has a temperature dependence

$$n_L/n_\Gamma = (m_{dn}^L/m_{dn}^\Gamma)^{3/2} \exp(-\Delta E_{L\Gamma}/k_B T)$$

and

$$n_L + n_\Gamma = n$$

where the superscripts L and Γ stand for the L and Γ minima respectively, and $\Delta E_{L\Gamma}$ is the energy difference between L and Γ minima. Although the assumption that the carrier capture is also via the L minimum is obviously not the first-order effect, the growing evidence of this assumption has been reported for other compound alloys [67,68]. Whether the carrier capture is from the Γ minimum by the MPE process or via the L minimum still needs further study.

4.1.3 Annealing behavior of electron trap V7 in epitaxial n-GaAs

It has been reported that the V7 trap concentration decreases after heat treatment at $\sim 750^\circ\text{C}$ for about 30 minutes in an H_2 ambient without encapsulation [22]. Mircea et al. attributed this phenomenon to out-diffusion of the defect responsible for deep level, and estimated the out-diffusion activation energy and outdiffusion coefficient as a function of temperature. Shown in Fig. 4.7 is the DLTS spectrum of electron traps in the unencapsulated VPE sample after heat treatment in ultra high purity N_2 flow ambient at 750°C for 30 minutes. Indeed the trap concentration of V7 does decrease. The isothermal and isochronal annealing results averaged over 4-8 samples are summarized in Table 4.2. There is no significant change for samples annealed at temperatures lower than 700°C . We can

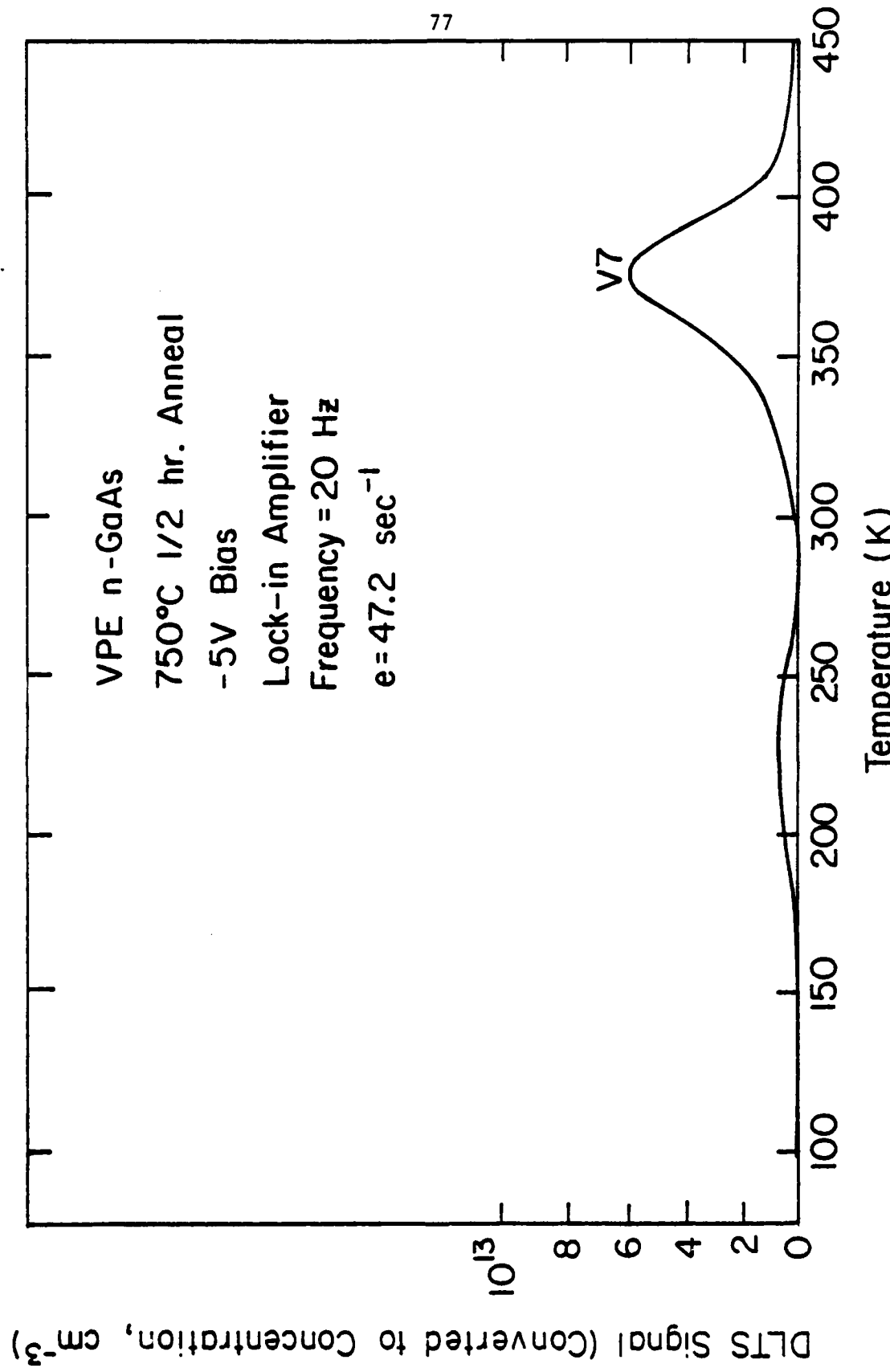


Fig. 4.7 DLTS spectrum of electron traps in unencapsulated VPE n-GaAs sample annealed at 750°C for 1/2 hr in N_2 ambient.

Table 4.2. Average Trap Concentrations in VPE n-GaAs for Various Annealing Conditions.

Encapsulation	Anneal Ambient	Anneal Temperature (°C)	Anneal Period (min)	Trap Concentration (cm ⁻³)
X	X	X	X	1.51×10^{14}
X	N ₂	700	10	1.26×10^{14}
X	N ₂	750	10	1.07×10^{14}
X	N ₂	750	30	5.80×10^{12}
Si ₃ N ₄	N ₂	700	30	1.48×10^{14}
Si ₃ N ₄	N ₂	800	30	4.01×10^{14}
Si ₃ N ₄	N ₂	800	60	5.40×10^{14}
SiO ₂	N ₂	700	30	1.52×10^{14}
SiO ₂	N ₂	800	30	3.34×10^{14}
SiO ₂	N ₂	800	60	2.91×10^{14}
X	As overpressure	750	30	1.41×10^{14}

successfully fabricate Schottky barriers on the samples annealed at temperature below 800°C, and obtain reasonable leakage current, forward and reverse breakdown voltages. The DLTS spectrum shown in Fig. 4.8 is for a sample annealed at 750°C for 1/2 h with As overpressure. The samples were sealed in a quartz ampule at 4×10^{-6} torr with enough As powder to ensure an As overpressure during the anneal. The result shows that the trap concentration does not change significantly. This suggests that the annealing behavior cannot be explained simply by outdiffusion of a defect. It also seems peculiar that the heat treatment in the studies by Mircea et al. [22] was not done with any dielectric encapsulation. It is well known that compound semiconductors tend to decompose due to the incongruent vaporization of compound elements at temperatures above 600°C [42]. We therefore examined the annealing behavior of encapsulated samples to study these effects.

Shown in Fig. 4.9 and Fig. 4.10 are the DLTS spectra for the samples annealed at 800°C for 1/2 h with high quality Si_3N_4 and SiO_2 encapsulations, respectively. It is very surprising that the trap concentrations in both cases do increase instead of decrease. Shown in Table 4.2 are the average trap concentrations after isothermal and isochronal annealing. It is obvious that the annealing behaviors are opposite for samples with and without encapsulation. Therefore, it is reasonable to explain the annealing behavior by assuming that the electron trap of 0.83 eV is related to the generation of Ga vacancies rather than a simple outdiffusion mechanism. The trap concentration is apparently related to the Ga vacancy concentration. For the annealed unencapsulated samples the higher (longer) the anneal temperature (time), the more As vacancies are created. Therefore, the effective Ga vacancy concentration

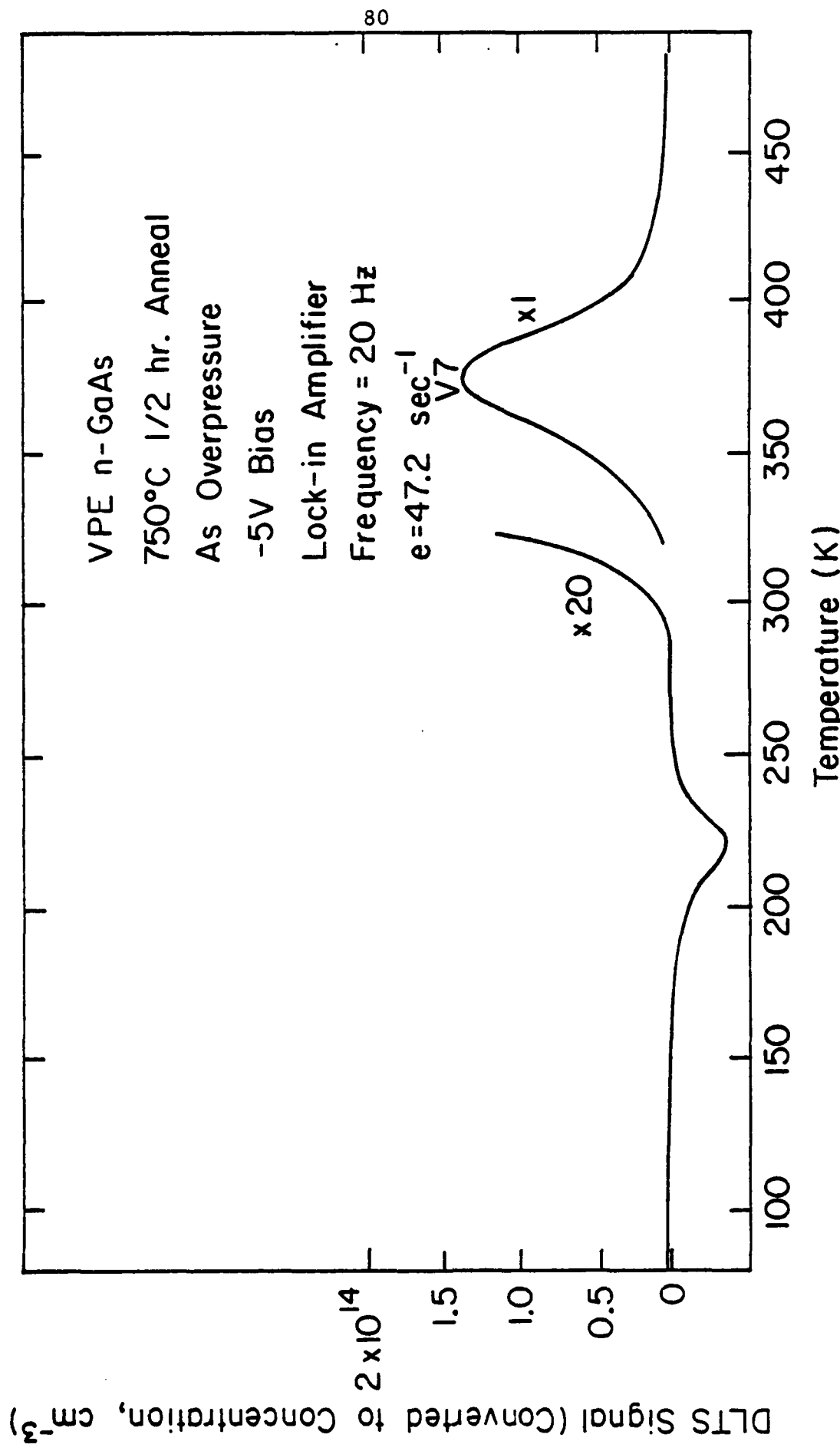


Fig. 4.8 DLTS spectrum of electron traps in unencapsulated VPE n-GaAs sample annealed at 750°C for 1/2 hr with As overpressure.

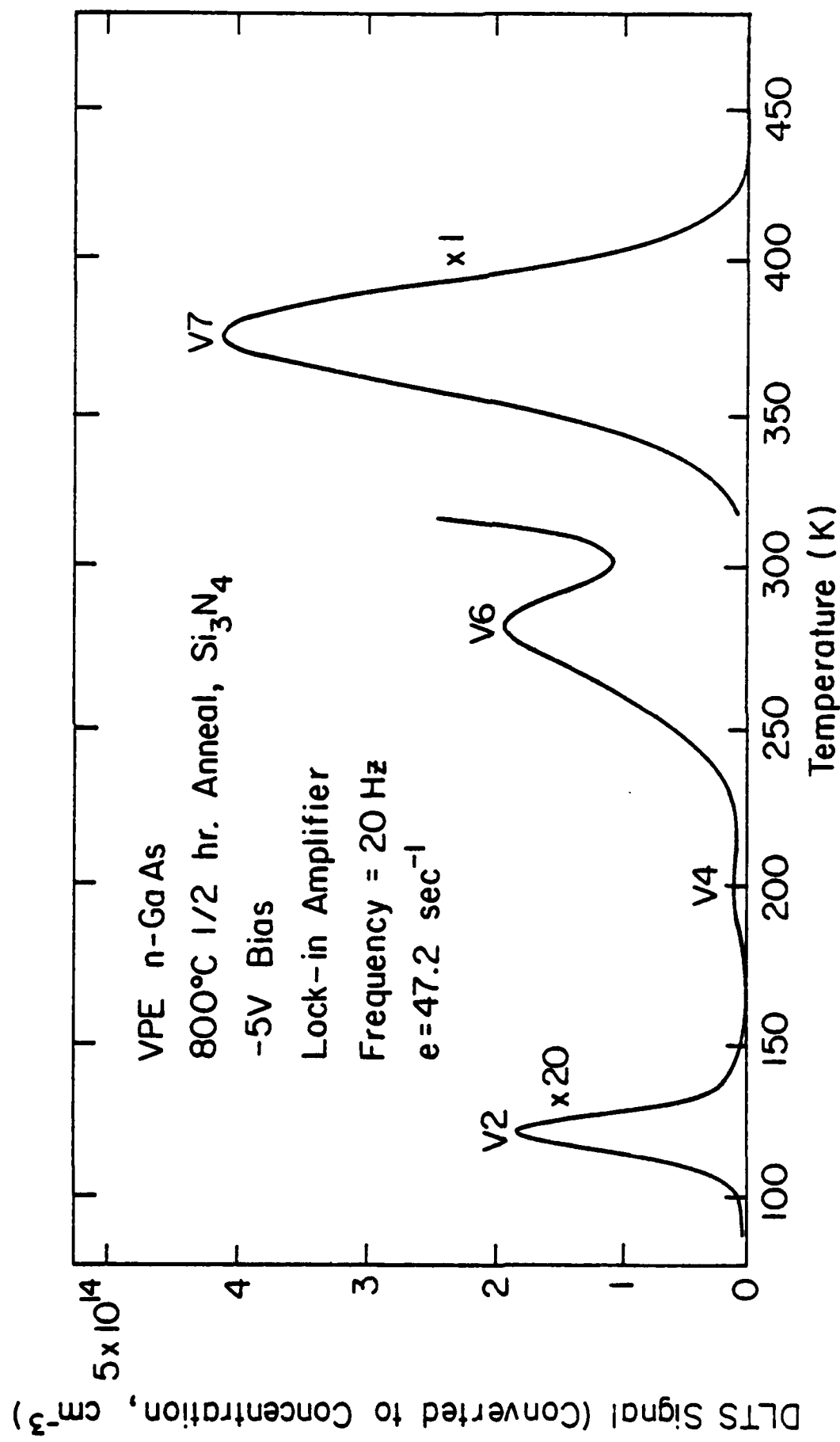


Fig. 4.9 DLTS spectrum of electron traps in Si_3N_4 encapsulated VPE n-GaAs sample annealed at 800°C for 1/2 hr.

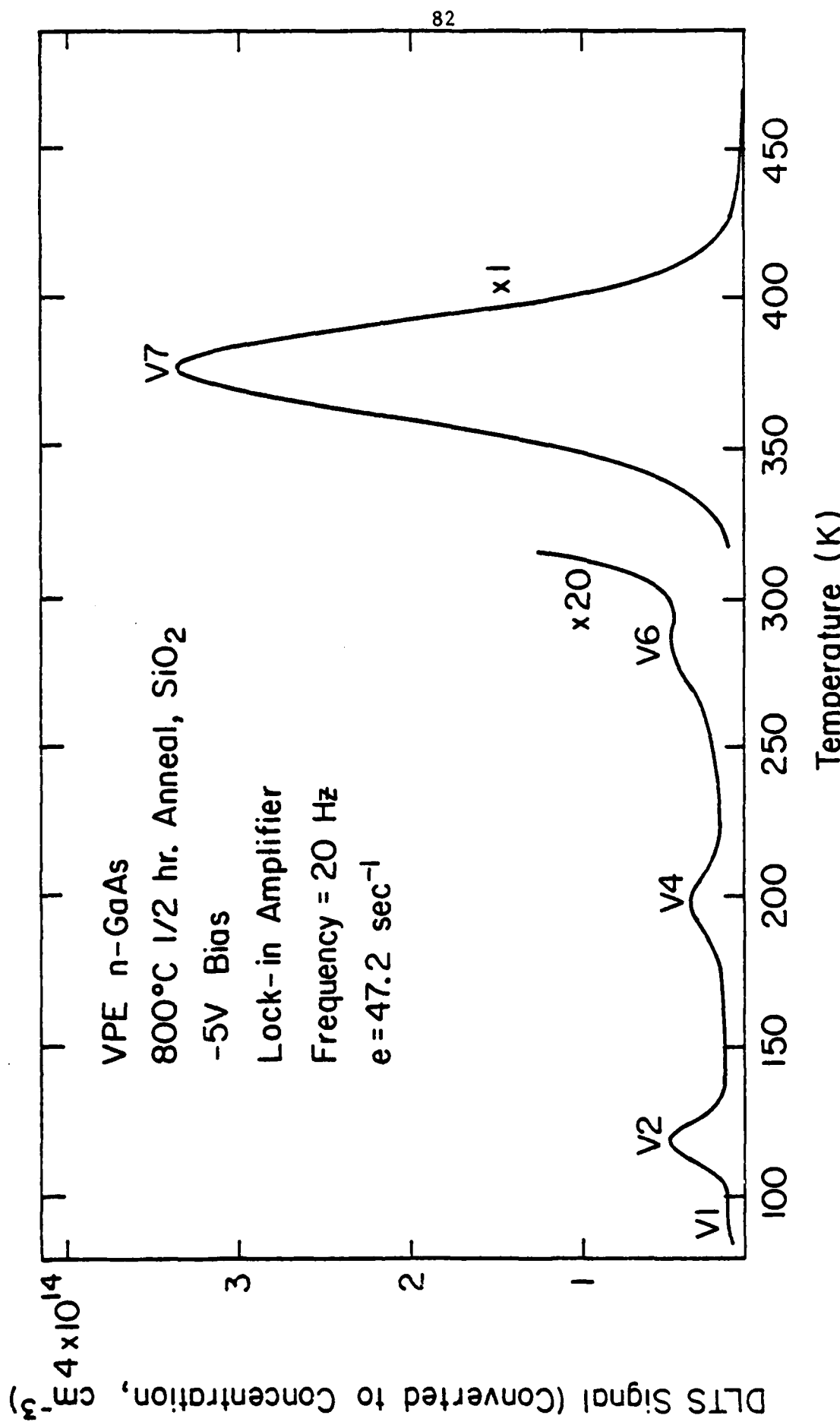


Fig. 4.10 DLTS spectrum of electron traps in SiO_2 encapsulated VPE n-GaAs sample annealed at 800°C for 1/2 hr.

decreases, as does the trap concentration. For encapsulated samples, As outdiffusion is suppressed as the equilibrium vapor pressure is built up between the dielectric layer and the GaAs. It is also known that Ga tends to diffuse into the dielectric layer, particularly SiO_2 . Therefore, the Ga vacancy density will increase for higher temperatures or longer anneal periods. This is confirmed by the example of As overpressure. With As overpressure the As outdiffusion is prevented and the Ga outdiffusion at 750°C or below is not significant. Therefore no significant vacancy generation effect is observed. For higher temperature As overpressure experiments, we cannot fabricate good Schottky barriers due to the resulting surface deterioration. This prevents possible observation of increases in trap concentration at higher anneal temperatures.

Although Ga outdiffusion into the SiO_2 layers is much more likely than that into Si_3N_4 layers for high temperature anneal [45], appreciable As outdiffusion has also been observed [45]. Therefore, for samples encapsulated with SiO_2 and annealed at 800°C for either 1/2 h or 1 h, the trap concentration really depends on the effective concentration of the Ga vacancy. This can probably explain a larger trap concentration observed in the Si_3N_4 encapsulated sample compared with the SiO_2 encapsulated one at the same annealing condition.

It has been reported that the 0.83 eV trap does not exist in typical LPE [53, 69] or MBE [70] material. In fact, LPE GaAs material is typically free of electron traps [53]. Since LPE GaAs growth employs a Ga-rich environment [71], traps involving Ga vacancies should be suppressed. As shown in Fig. 4.11, high-quality LPE material is

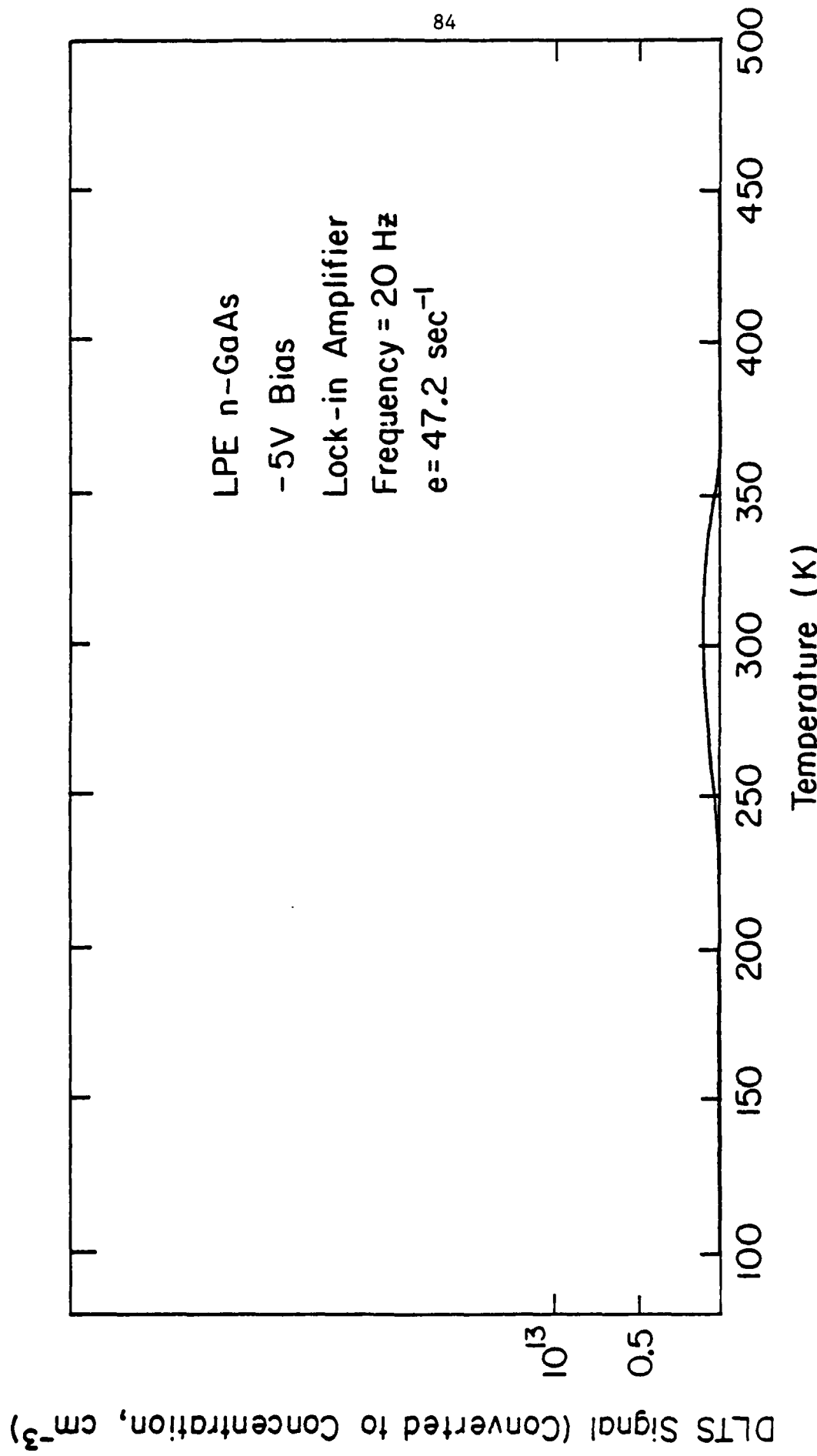


Fig. 4.11 DLTS spectrum of electron traps in LPE n-GaAs.

observed to be quite free of electron traps. The VPE GaAs growth process, on the other hand, usually employs As-rich conditions, which should result in a large concentration of Ga vacancies. For the MBE n-GaAs material used in this study, the growth process is only slightly As rich [72]. Shown in Fig. 4.12 is the DLTS spectrum of electron traps in the MBE samples grown in the first few runs of the Riber system. The 0.83 eV is not observable. Although there has been a report on electron traps in MBE GaAs [70], we believe that the DLTS signal in our system has a much better signal to noise (S/N) ratio, which allows better estimation of energy levels as well as concentration. The Arrhenius plot of $T^2\tau$ vs $1000/T$ for each trap is shown in Fig. 4.13. The capture cross section for each trap obtained from emission rate measurement is listed in Table 4.3. Although the electron trap of 0.83 eV is not observable in LPE and MBE n-GaAs material, we can produce this trap level by changing the stoichiometric ratio near the surface layer as a result of annealing. Shown in Fig. 4.14 is the electron trap spectrum in MBE n-GaAs sample encapsulated with SiO_2 and annealed at 800°C for 1/2 hr. As expected, the trap M6 (0.83 eV) becomes observable due to the annealing effect on the encapsulated sample. Shown in Fig. 4.15 is the spectrum for LPE n-GaAs sample encapsulated with Si_3N_4 and annealed at 800°C for 1/2 h. It is surprising that a small amount of the 0.83 eV trap level is detected. A detailed study of annealing effect on MBE and LPE n-GaAs material is being undertaken in this laboratory and will not be addressed here.

We believe that the above experimental results support the hypothesis of electron trap V7 being related to the Ga vacancy. To

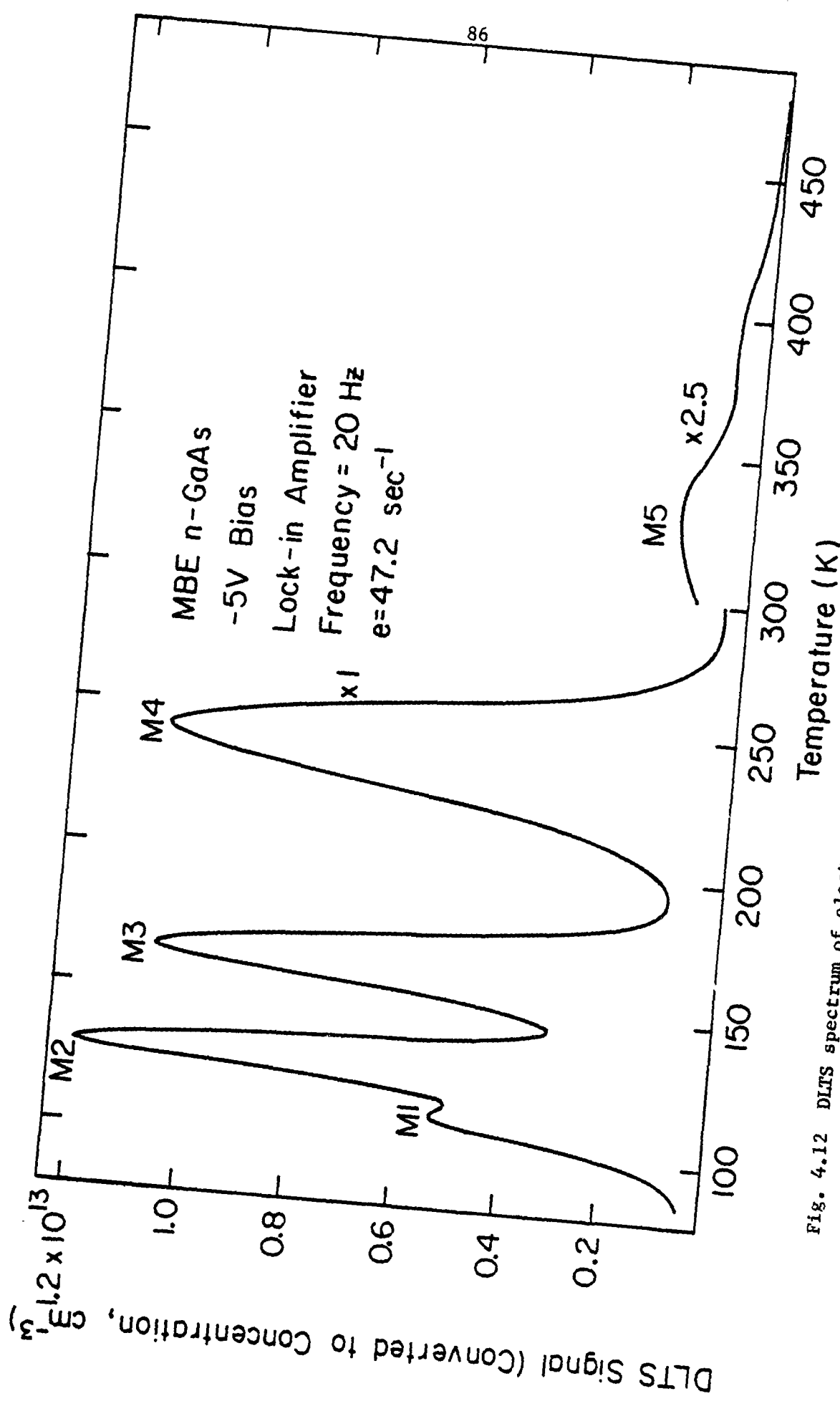


Fig. 4.12 DLTS spectrum of electron traps in MBE n-GaAs.

RD-A124 886

STUDIES OF ELECTRON TRAPS IN GALLIUM ARSENIDE AND
GALLIUM ARSENIDE PHOSPH. (U) ILLINOIS UNIV AT URBANA
COORDINATED SCIENCE LAB D S DAY MAR 80 R-877

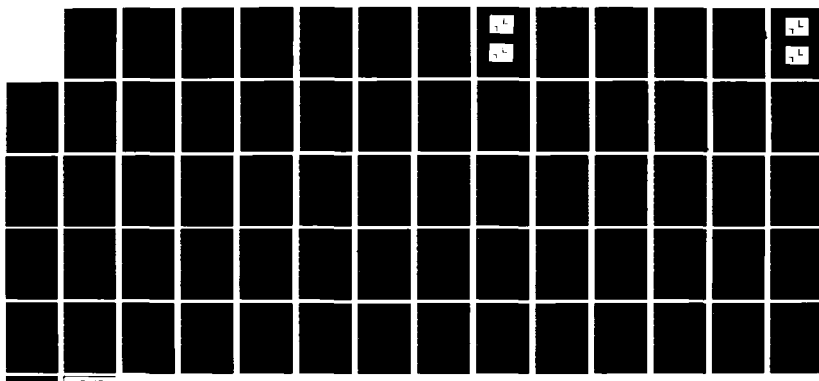
2/2

UNCLASSIFIED

N88814-79-C-0424

F/G 28/12

NL

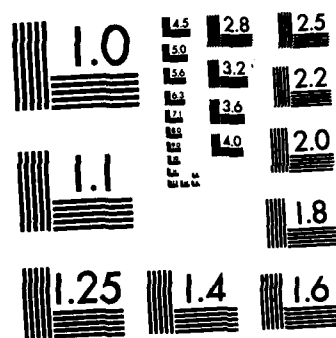


END

FILED

1

DTIC



MICROCOPY RESOLUTION TEST CHART
NATIONAL BUREAU OF STANDARDS-1963-A

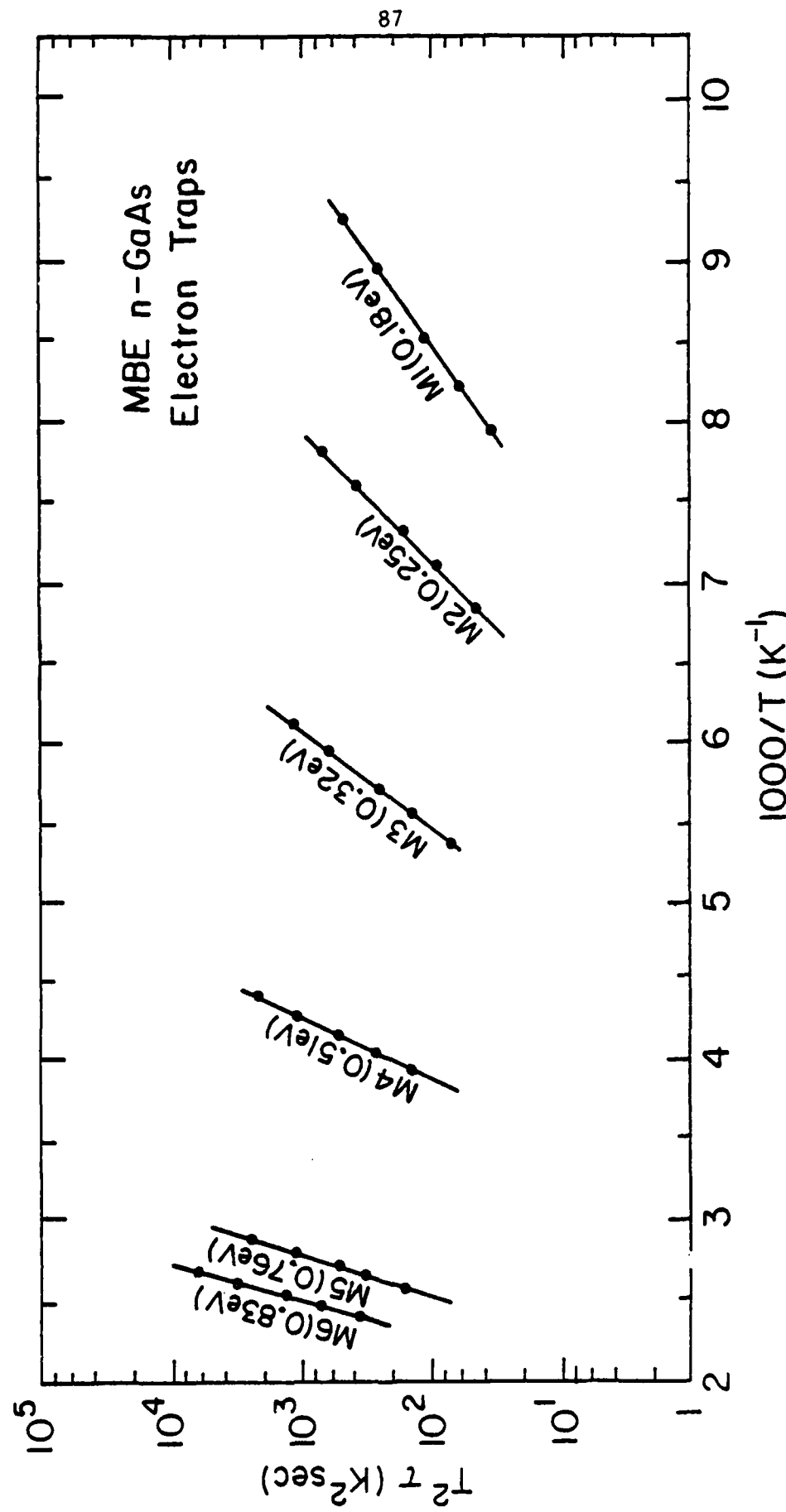


Fig. 4.13 Arrhenius plots of T_2^2 vs $1000/T$ for electron traps in MBE n-GaAs under various experimental conditions.

Table 4.3. Thermal Activation Energies and Capture Cross Sections of Electron Traps in MBE n-GaAs.

Trap	Activation Energy ΔE (eV)	Capture Cross- Section σ_∞ (cm^2)	Temperature Range (K)
M1	0.18	9.7×10^{-16}	105-130
M2	0.25	3.1×10^{-14}	125-150
M3	0.32	2.6×10^{-14}	160-190
M4	0.51	5.1×10^{-13}	225-260
M5	0.75	2.3×10^{-13}	340-390
M6	0.83	1.8×10^{-13}	370-420

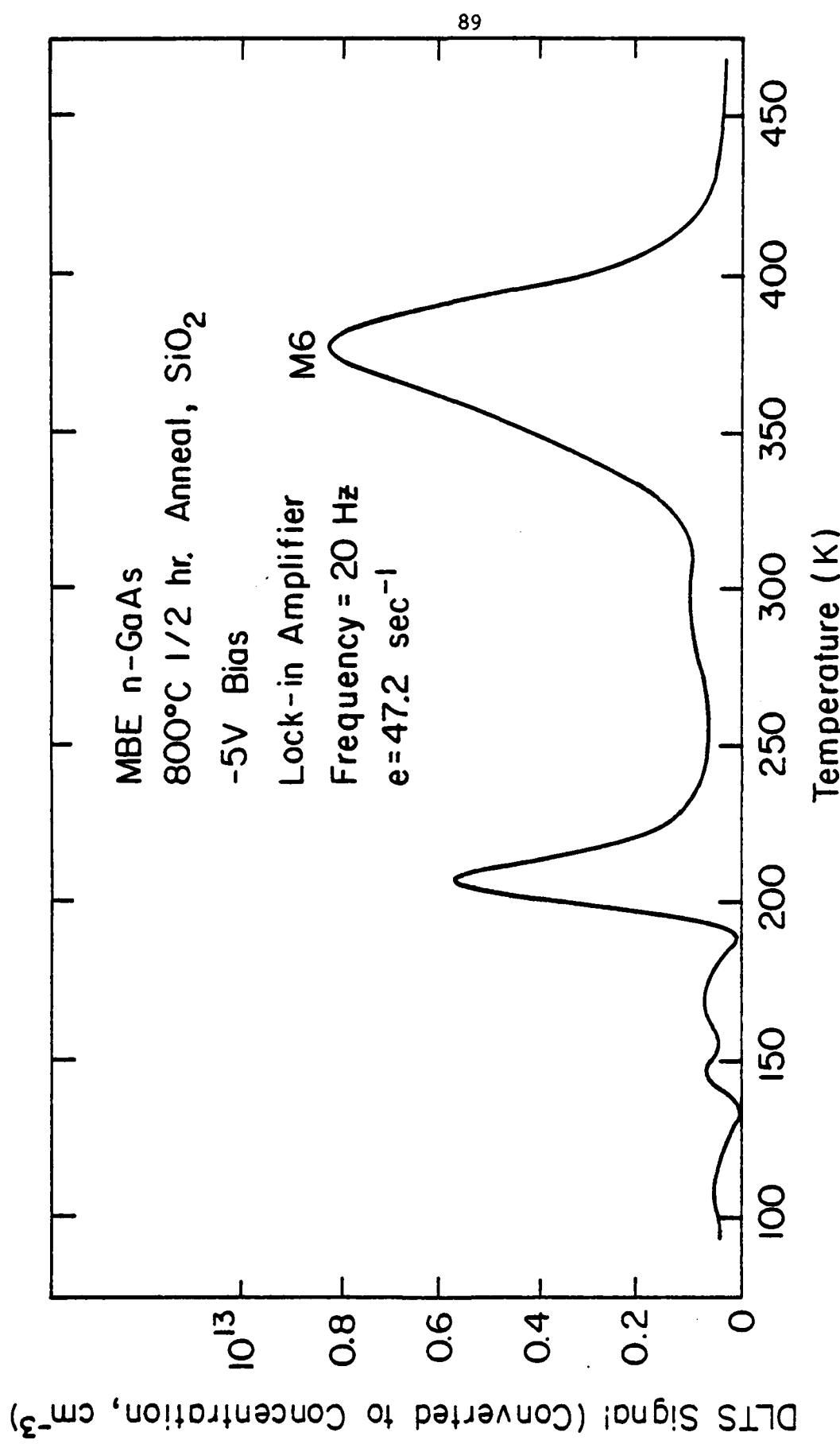


Fig. 4.14 DLTS spectrum of electron traps in SiO_2 encapsulated MBE n-GaAs sample annealed at 800°C for 1/2 hr.

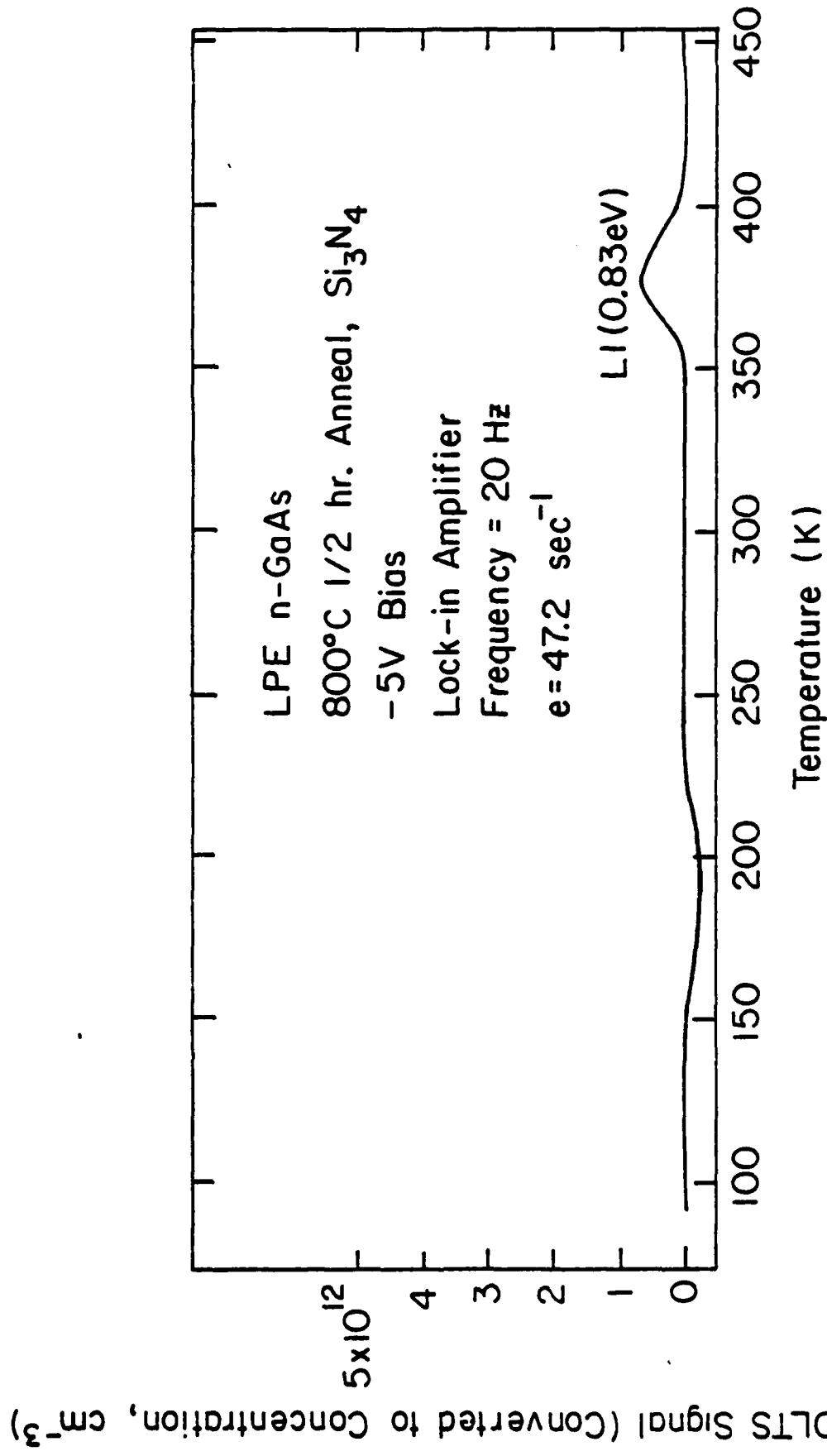


Fig. 4.15 DLTS spectrum of electron traps in Si_3N_4 encapsulated LPE n-GaAs annealed at 800°C for $1/2$ hr.

further test this hypothesis we have carried out experiments utilizing ion implantation as a research tool.

4.1.4 Study of electron trap V7 in ion implanted VPE n-GaAs.

As mentioned in Section 2.4, ion implantation has been a powerful tool for semiconductor research because of its doping uniformity, controllability, and reproducibility.

Shown in Fig. 4.16 is the spectrum of electron traps in VPE GaAs implanted with B^+ and annealed with Si_3N_4 encapsulation at $800^\circ C$ for 1/2 hr. The acceleration voltage is 250 keV and the dose is $10^{14} cm^{-2}$. The projected range R_p and its standard deviation ΔR_p can be obtained from the tables in Appendix D. The peak concentration is estimated to be $2.5 \times 10^{18} cm^{-3}$. It has been reported that the carrier compensation due to the implanted B atoms is not significant for such high dose implants and high temperature anneal [73]. We do not observe significant compensation effect from the I-V characteristics shown in Fig. 4.17(a), or in C-V characteristics of the Schottky barrier. Therefore, the net donor concentration is assumed to be approximately the original doping $1.2 \times 10^{15} cm^{-3}$. The decrease of the trap concentration compared with Fig. 4.9 may be due to Boron incorporation into Ga vacancy sites. In order to be sure that the implanted ions fit into the Ga substitutional sites, we carried out Be implants into n-GaAs [74] (Fig. 4.18). The implantation energy is 250 keV and the dose is $10^{14} cm^{-2}$. The detailed planar $p^+ n$ GaAs diode fabrication procedure has been described elsewhere [74]. Although the observed junction region is about 1.2 μm [44, 75] away from the surface, the net donor concentration and the trap concentration previous to the implant can still be

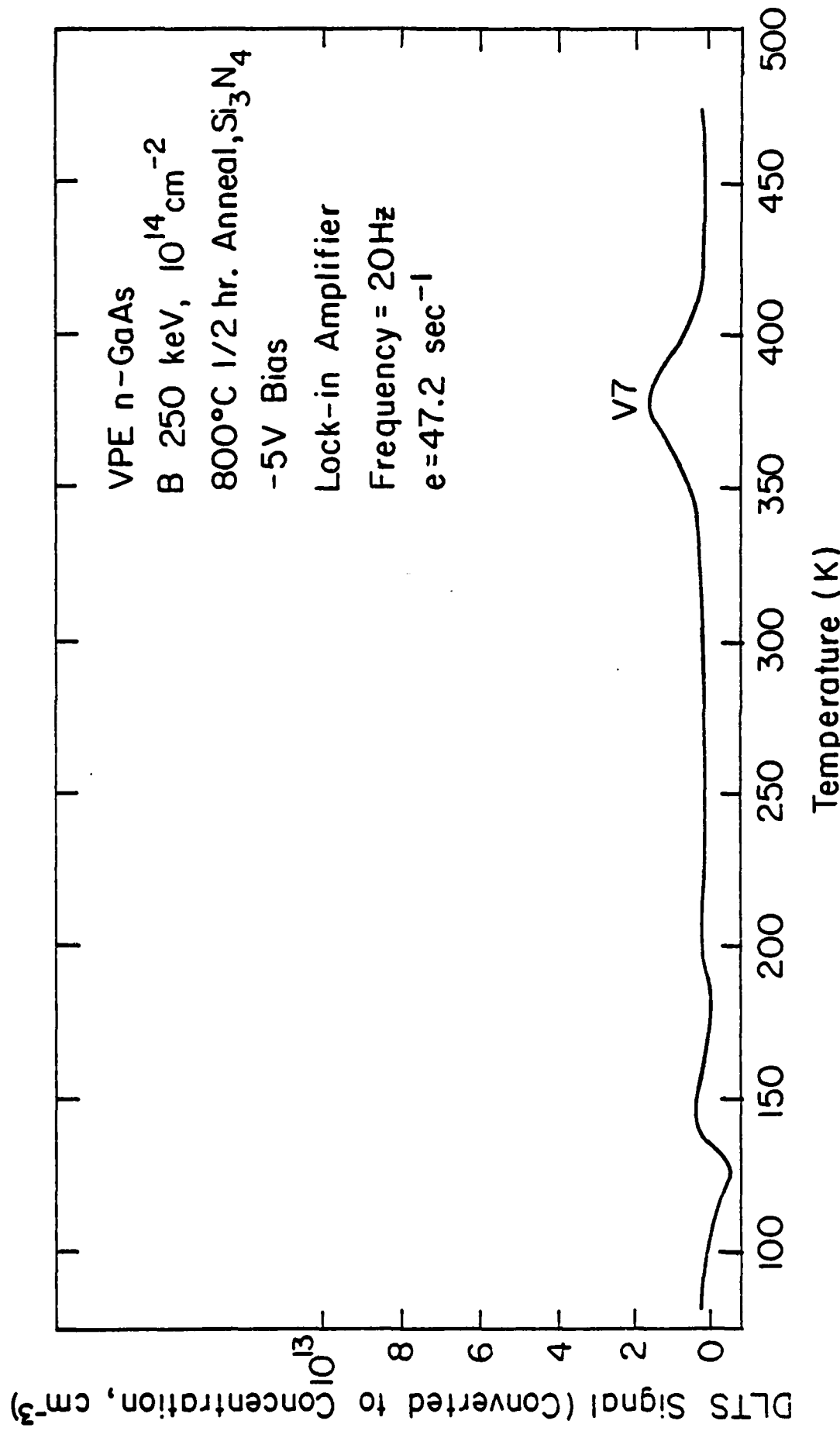
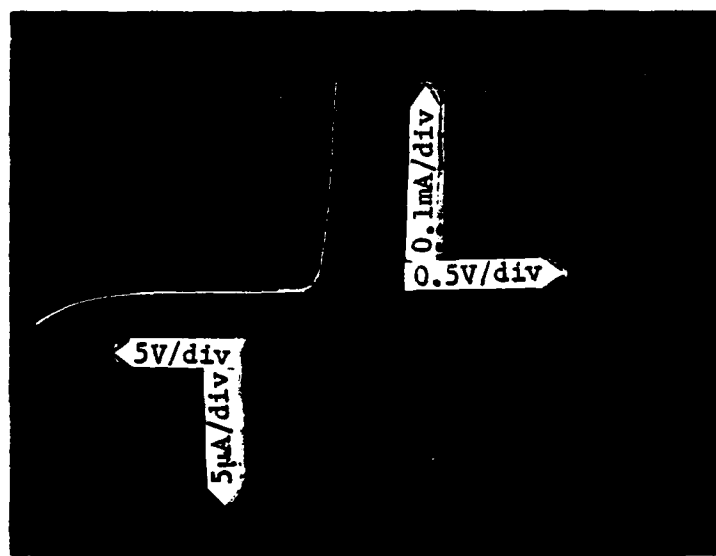


Fig. 4.16 DLTS spectrum of electron traps in B implanted VPE n-GaAs.

(a)



(b)

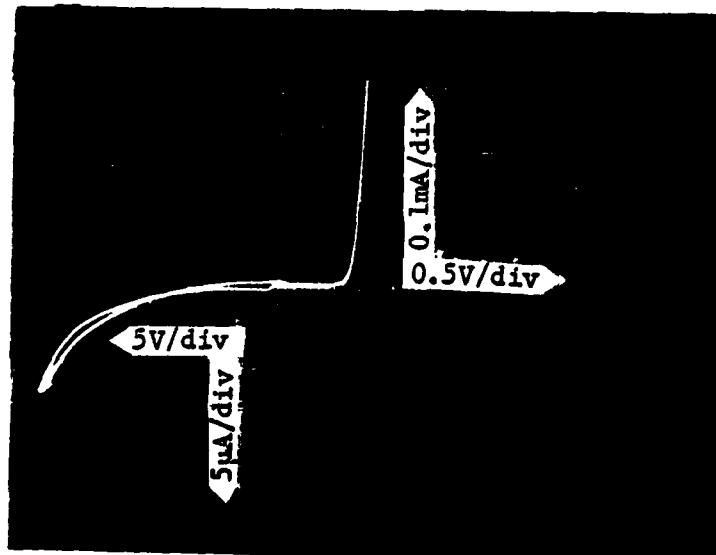


Fig. 4.17 I-V characteristics of Schottky barriers on
(a) B implanted VPE n-GaAs;
(b) Ga implanted VPE n-GaAs.

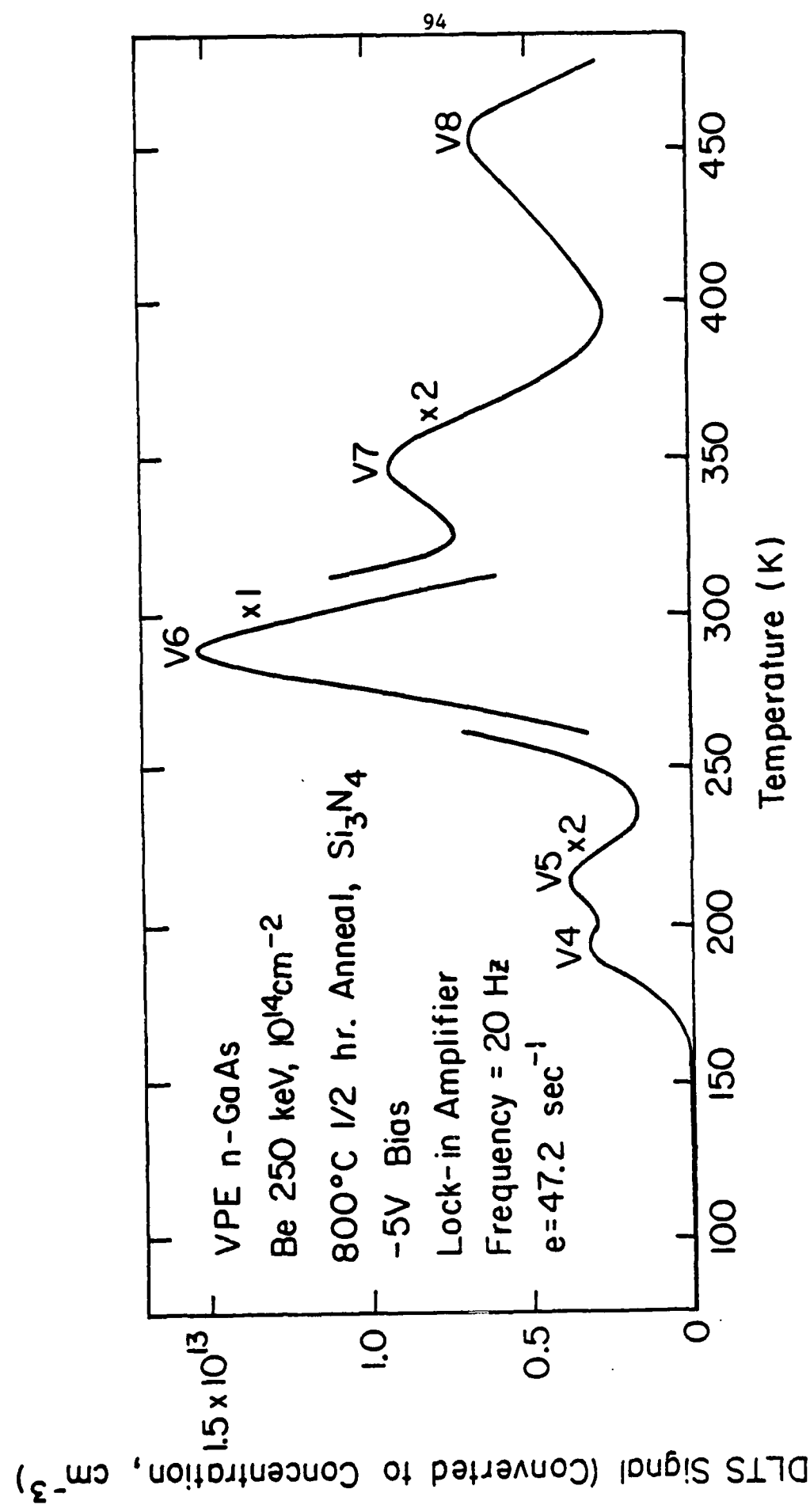


Fig. 4.18 DLTS spectrum of electron traps in Be implanted VPE n-GaAs.

assumed to be about the same as that in the surface layer. Again a significant decrease of the V7 trap concentration is observed compared with Fig. 4.9. As for the trap V6 (0.58eV), it has been reported that this trap is related to the radiation damage caused by Be implant into VPE n-GaAs [76]. We have strong evidence from Fig. 4.9 and Fig. 4.10 that this trap does exist in the unimplanted material. Therefore, the defect responsible for V6 can result from the annealing of unimplanted material as well as from radiation damage. We have also performed Ga implants into n-GaAs with 250 keV implantation energy and $2 \times 10^{13} \text{ cm}^{-2}$ dose. As shown in Fig. 4.19, we observed a very small negative peak around the temperature for the V7 trap at the present rate window $\epsilon = 47.2 \text{ sec}^{-1}$. For a Schottky barrier, only the majority carrier (electron) traps can be observed if the Schottky barrier is good. Shown in Fig. 4.17(b) is the I-V characteristics of the Schottky barrier on Ga-implanted n-GaAs. The forward threshold voltage is larger than that in Fig. 4.2 and the reverse I-V characteristic shows hysteresis. This larger threshold voltage together with the small negative DLTS peak may be due to the imperfect Schottky barrier caused by the heavy ion implant. Nevertheless, the DLTS results on the samples implanted with B, Be and Ga convince us that the trap V7 is probably related to the Ga vacancy.

As mentioned previously, it has been conjectured that level V7 is related to oxygen in n-GaAs. There has also been a contradictory report that this level is not related to oxygen [77]. This latter conclusion is drawn from the fact that the V7 trap concentration by DLTS is greater than the oxygen content estimated by SIMS measurement. It would be difficult to draw this conclusion if the oxygen content

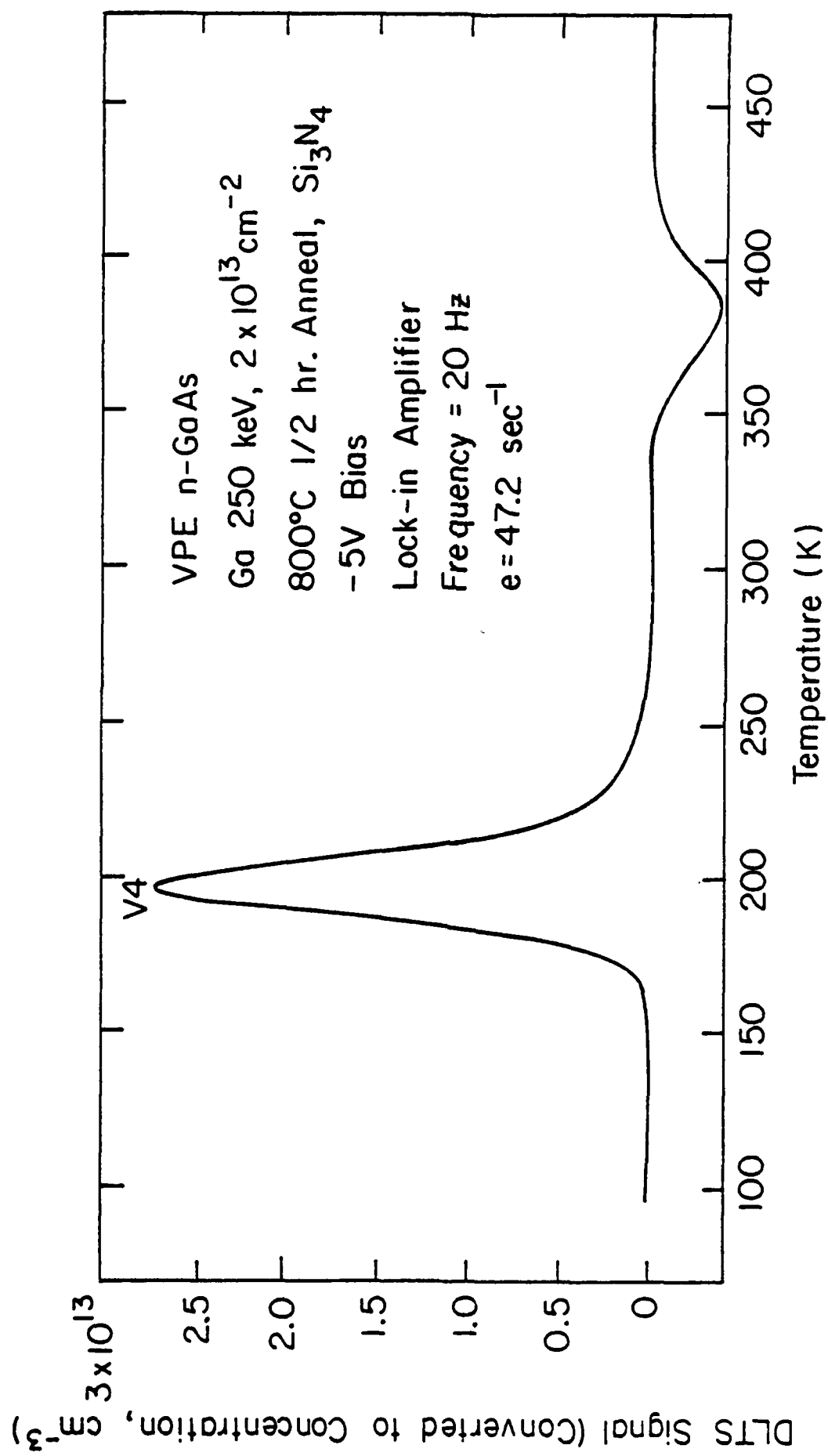
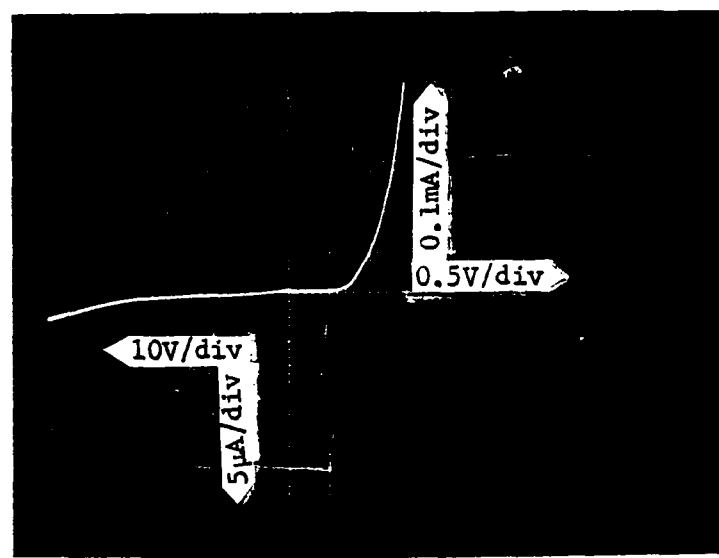


Fig. 4.19 DLTS spectrum of electron traps in Ga implanted VPE n-GaAs.

happened to be larger than the trap concentration. To investigate this controversy, we have done oxygen implants into GaAs with implantation energy of 250 keV and dose of 10^{14} cm^{-2} in order to see whether the oxygen implant has any effect on this level. It has been reported [78] that oxygen implants into n-GaAs would result in high resistivity material at anneal temperatures higher than 500°C. There is also a report [79] that oxygen implants will not necessarily create high resistivity layers when performed on high quality epitaxial GaAs material. Indeed, we did not observe significant semi-insulating properties in the I-V characteristics shown in Fig. 4.20(a) and the C-V characteristics. Shown in Fig. 4.21 is the DLTS spectrum of the sample implanted with oxygen and annealed at 800°C for 1/2 hr. Comparing this figure with Fig. 4.9, we observe that the implanted oxygen content does not affect the V7 trap concentration, and we therefore conclude that oxygen is not involved in V7, the main electron trap in VPE GaAs. In order to see whether the incorporation of group V elements affects this deep level, an implant of N into GaAs with 250 keV and 10^{14} cm^{-2} was performed. The implanted sample was encapsulated with an SiO_2 layer and annealed at 800°C for 1/2 hr. Again, we have good Schottky barriers with I-V characteristics shown in Fig. 4.20(b) and do not observe the compensation effect previously reported [80]. The DLTS result shown in Fig. 4.22 indicates that the trap concentration increases significantly compared with Fig. 4.9. This may be due to the fact that nitrogen fits into As substitutional sites as a resonance state with respect to the Γ minimum [81]. Therefore, the effective concentration of the Ga vacancy increases and the V7 trap concentration increases proportionally.

(a)



(b)

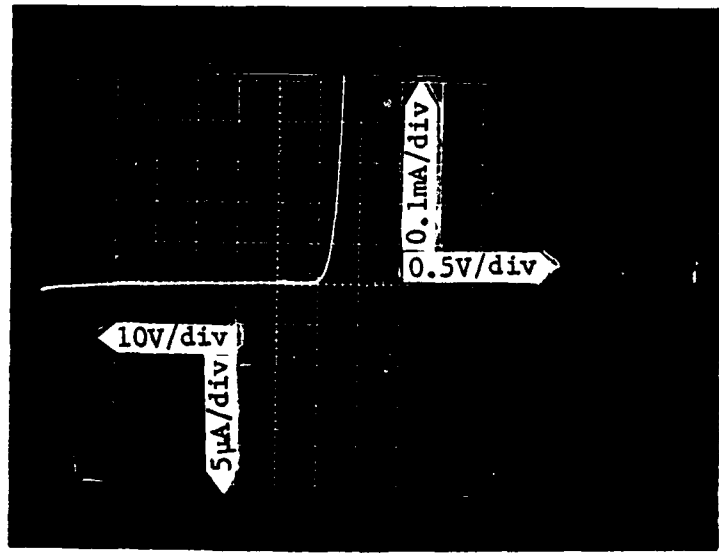


Fig. 4.20 I-V characteristics of Schottky barriers on (a) O implanted VPE n-GaAs; (b) N implanted VPE n-GaAs.

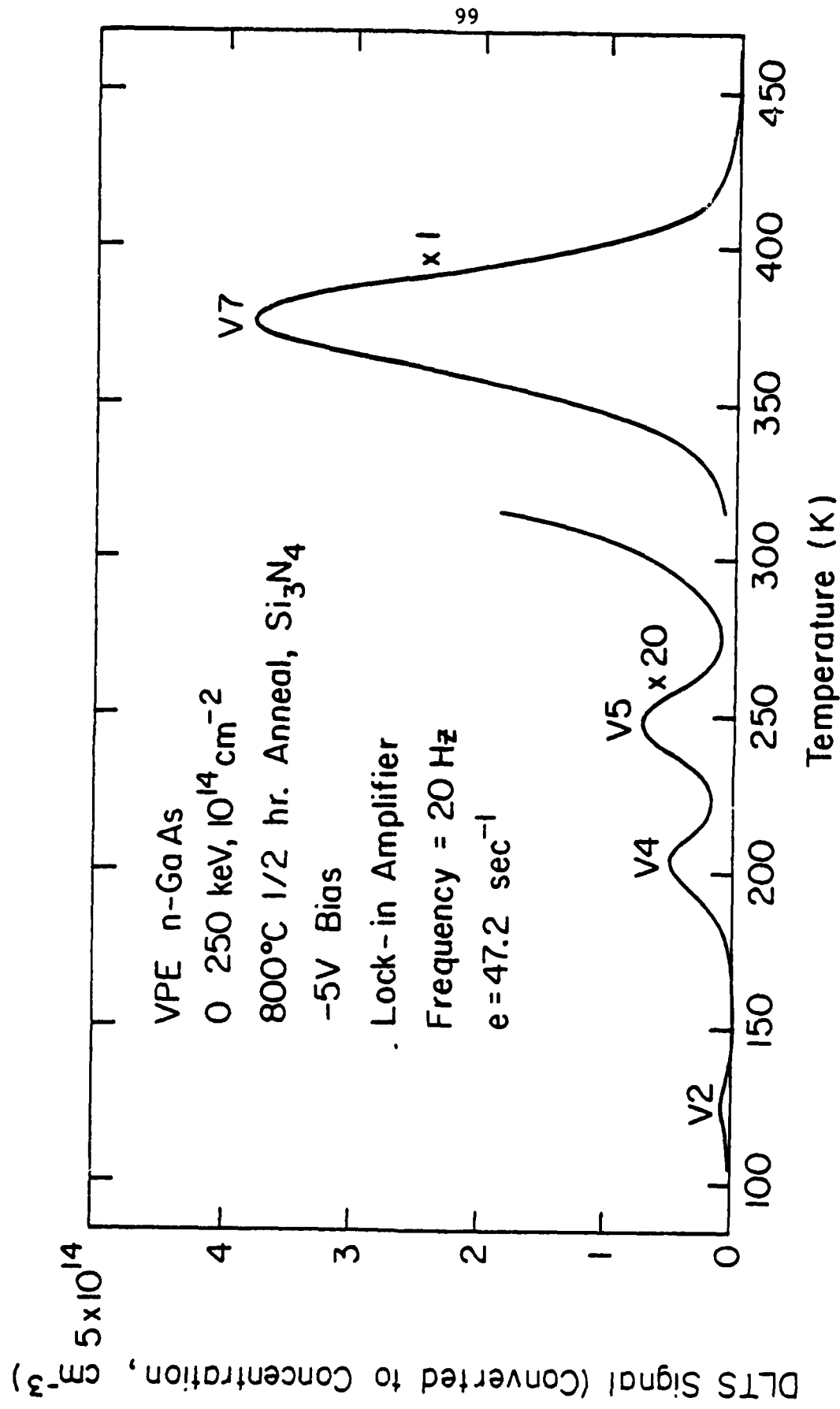


Fig. 4.21 DLTS spectrum of electron traps in O implanted VPE n-GaAs.

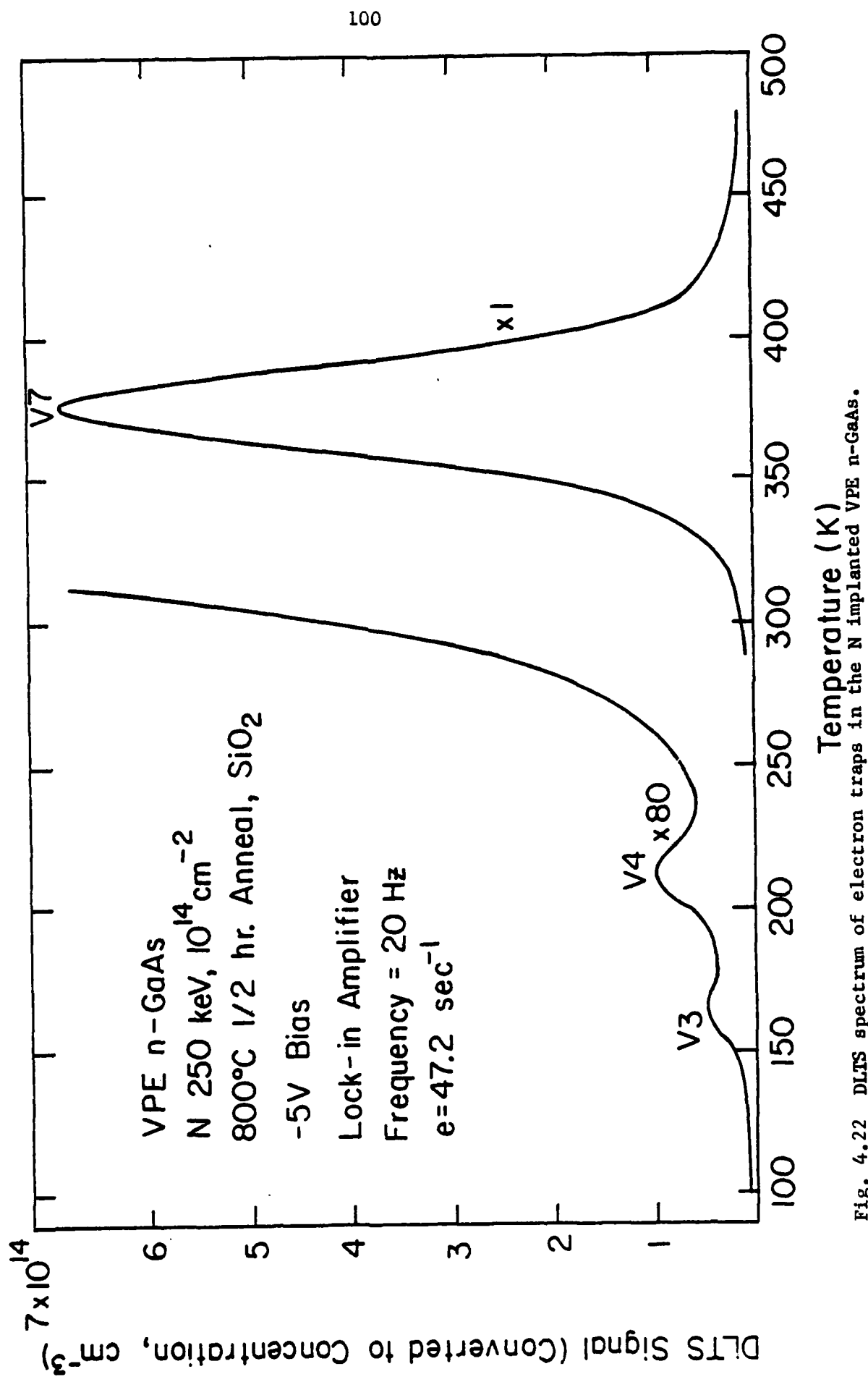


Fig. 4.22 DLTS spectrum of electron traps in the N implanted VPE n-GaAs.

In the study of the main electron trap in VPE n-GaAs we have examined the annealing behavior of this deep level and the effect of the implanted species. In the annealing study, we found that the trap concentration change is consistently related to the Ga vacancy concentration. In the implantation study we observed that the trap concentration changes depending on whether the implanted species is incorporated into Ga or As substitutional sites. From these DLTS results, we believe at this time that the main electron trap (V7) probably involves the Ga vacancy.

4.2 Studies of Electron Traps in VPE n-GaAs_{1-x}P_x Ternary Alloy

The GaAs_{1-x}P_x ternary alloy has been used extensively in the visible light emitting diode (LED) industry. The addition of nitrogen doping in this alloy yields a marked improvement as electroluminescence (EL) efficiency in the indirect energy bandgap region [82]. Although the radiative recombination mechanism in the GaAs_{1-x}P_x alloy or GaAs_{1-x}P_x:N alloy system has been extensively studied [81-85], there are only limited reports [24-28] on the deep levels in this material by the deep level transient spectroscopy method. The nonradiative recombination centers in GaAs_{1-x}P_x alloy have been believed very important to the luminescence efficiency [25,26,28,33]. In this chapter, we will examine the electron traps in the GaAs_{1-x}P_x alloy system for several compositions.

4.2.1 Material preparation and device fabrication

All the vapor phase epitaxial (VPE) GaAs_{1-x}P_x crystals used in this work were provided by the Monsanto Company (St. Louis) and were grown by an open tube AsH₃-PH₃ vapor transport method [86]. For alloy compositions $X < 0.50$ the layers were grown on n⁺ (100) -oriented GaAs

substrates, while for $X \geq 0.50$, n^+ (100) -oriented Gap substrates were used. During the first 10 to 50 μm of growth, the ternary composition x is graded at $1\%/\mu\text{m}$ from that of the substrate to the desired composition x in order to minimize the effects of lattice mismatch. Even with this composition grading, however, misfit dislocations appear in the epitaxial layer. The indirect-gap ($x \geq 0.46$) $\text{GaAs}_{1-x}\text{P}_x$ crystals have been doped with nitrogen during the final $10\mu\text{m}$ of growth by adding NH_3 to the dopant gas mixture [86]. The N doping in these crystals is estimated to be $\sim 10^{19}\text{ cm}^{-3}$ [86]. The $\text{GaAs}_{1-x}\text{P}_x$ wafers used in this work were of compositions $40\pm 1\%$, $65\pm 1\%$, $85\pm 1\%$ and 100% P on the column V sub-lattice. The $x = 0.40$ epilayer was doped with Te up to $\sim 10^{17}\text{ cm}^{-3}$, while the others were doped with S up to $\sim 5.5-7.5 \times 10^{16}\text{ cm}^{-3}$. The "nitrogen free" samples used in this study were prepared by etching away the N doped layer using a GaP etchant made by Transene Co. The etch rate is $\sim 1.5\mu\text{m}/\text{min}$ at 80°C . An etch period of ~ 8 min is appropriate for obtaining a virtually N free epilayer, as checked by photoluminescence [87]. All the N-doped samples were etched to remove $\sim 3.5\mu\text{m}$ of the surface layer to avoid composition variation [83].

Ni and Au-Ge eutectic alloy were evaporated on the backside of the processed substrate, with layer thickness of $1000\text{\AA}-2000\text{\AA}$, and then sintered at 450°C for 1 minute to make ohmic contacts. Al of $\sim 1000\text{\AA}-2000\text{\AA}$ was evaporated on the epitaxial $\text{GaAs}_{1-x}\text{P}_x$ layer to form Schottky barriers. Two Schottky barriers were cleaved from the same sample and mounted on the same To-18 header used in the DLTS system with the two-diode method described in Section 3.1.

4.2.2. Electron traps in VPE n-GaP

Electron traps in VPE n-GaP have been reported by several authors [24-28], and summarized by Lang [52] and by Mircea et al. [53]. Additional information is required, including capture cross sections, along with the emission rate to make sure that deep levels observed under different experimental conditions correspond to the same defect. In this section, we will report the thermal activation energies as well as the capture cross sections for the traps observed under various conditions in our study.

Shown in Fig. 4.23 is the DLTS spectrum of electron traps in N-doped VPE n-GaP. The thermal activation energies are as indicated in Table 4.4. The capture cross sections σ_∞ obtained from Eq. (2.13) are also listed in Table 4.4. Here, it is assumed that $m^* = 0.365 m_e$ and $m_{dn} = 1.20 m_e$ according to the equation [88].

$$m^* = (0.35 + 0.015x) m_e \quad (4.4)$$

and $m_{dn} = 1.20 m_e$ for x minimum

The energy levels are in good agreement with those reported by Tell et al. [27]. However, the calculated capture cross section σ_∞ is much larger than that obtained by the capture rate measurement at the observed temperature [27]. This might be explained by multiphonon emission [33] (MPE) according to Eq. (2.12), in which an activation energy for the carrier capture is required. As shown in Fig. 4.24, it is interesting to notice that the levels E_{12} and E_{13} are not detectable or resolvable in the N-free sample, and the level E_{21} does not have the same energy as E_{11} . We have examined several samples and obtained the same results. In order to see whether this change is due to the addition of nitrogen,

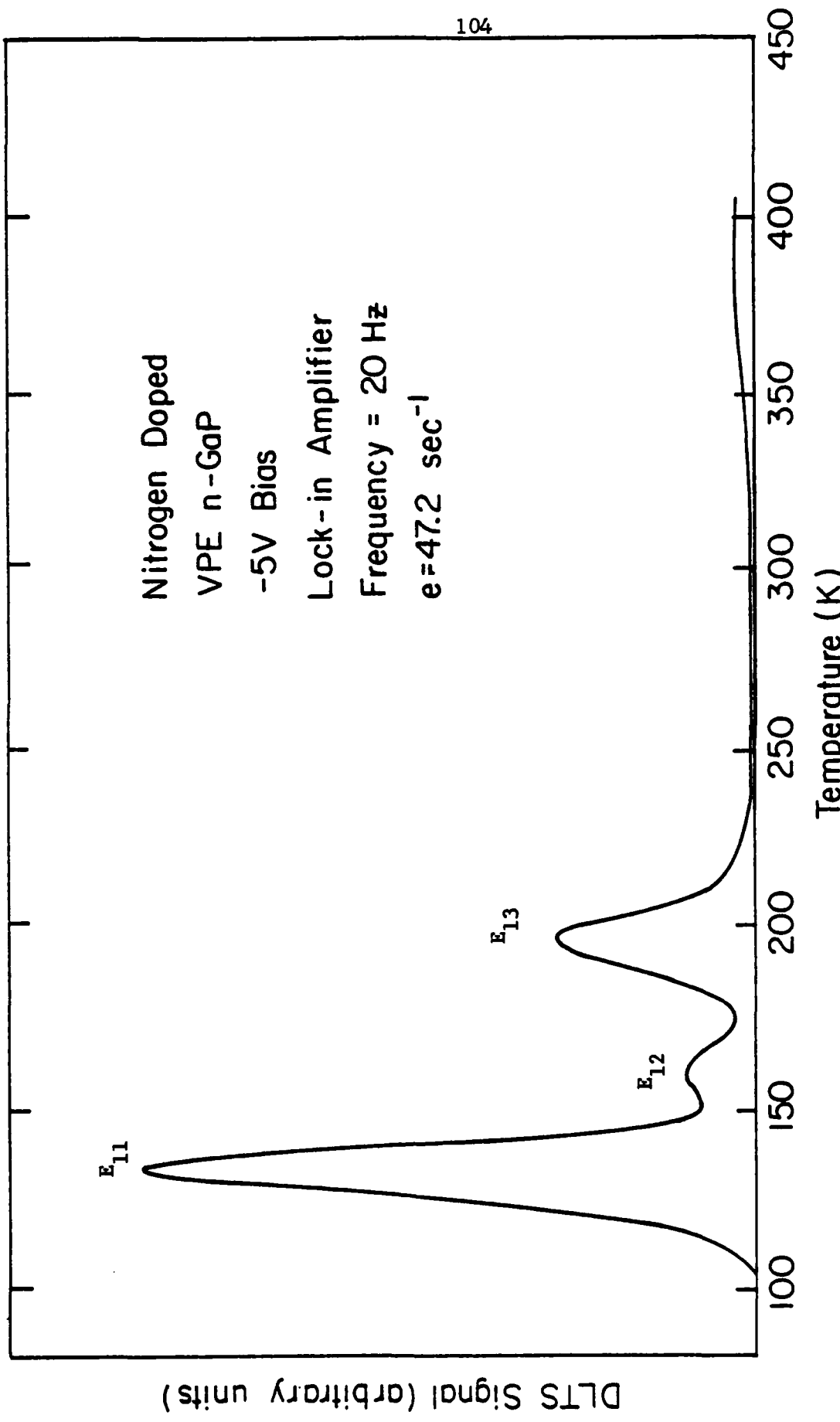


Fig. 4.23 DLTS spectrum of electron traps in N-doped GaP.

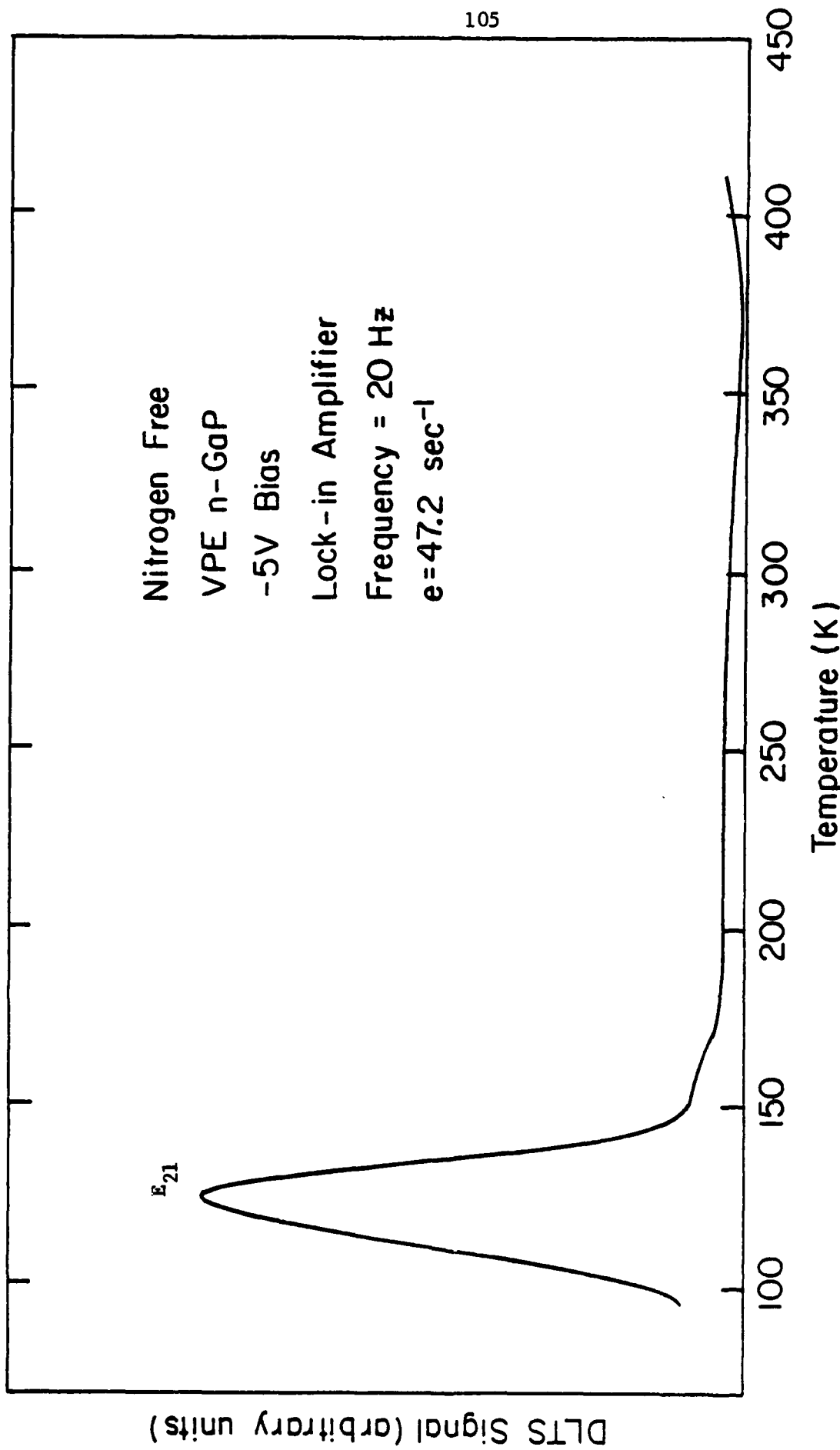


Fig. 4.24 DLTS spectrum of electron traps in N-free GaP.

N implants at 200 keV with N peak concentrations of $1 \times 10^{18} \text{ cm}^{-3}$ and $5 \times 10^{18} \text{ cm}^{-3}$ were performed. Shown in Fig. 4.25 is the spectrum for a N implanted sample with $1 \times 10^{18} \text{ cm}^{-3}$ peak concentration the energy level for E_{31} is estimated to be 0.23 eV, which is between the activation energies of E_{11} and E_{21} . If the levels E_{11} , E_{21} , and E_{31} were indeed from the same origin but modified by the existence of N doping, it would be worthwhile and interesting to establish the relation between the activation energy shift and the N doping. The level E_{32} is estimated to be 0.57 eV. Levels similar to E_{12} and E_{13} in the N-doped sample are not detected in the N-implanted samples. This could be due to the fact that the N concentration in the implanted sample is not as high as in the N-doped sample. Shown in Fig. 4.26 is the spectrum for the sample implanted with N peak concentration of $5 \times 10^{18} \text{ cm}^{-3}$ at 200 keV and annealed at 850°C in Ar ambient for 1/2 hr with SiO_2 encapsulation. The level E_{41} is estimated to be 0.24 eV. The activation energy for E_{42} is obtained as 0.55 eV. There are two broad peaks which are probably due to radiation damage. The energy levels for these broad peaks have not been determined. Similar broad peaks have been observed in 1 MeV electron irradiated GaP samples [24]. It seems that there are peaks between E_{41} and E_{42} in the spectrum. These peaks might be related to the levels E_{12} and E_{13} observed in the N-doped samples. Further studies should be made in order to verify that E_{12} and E_{13} are related to the existence of high N doping instead of being material dependent.

4.2.3 Electron traps in VPE n-GaAs_{0.15}P_{0.85}

Shown in Fig. 4.27 is the DLTS spectrum for N-doped GaAs_{0.15}P_{0.85}. The activation energies as well as the capture cross

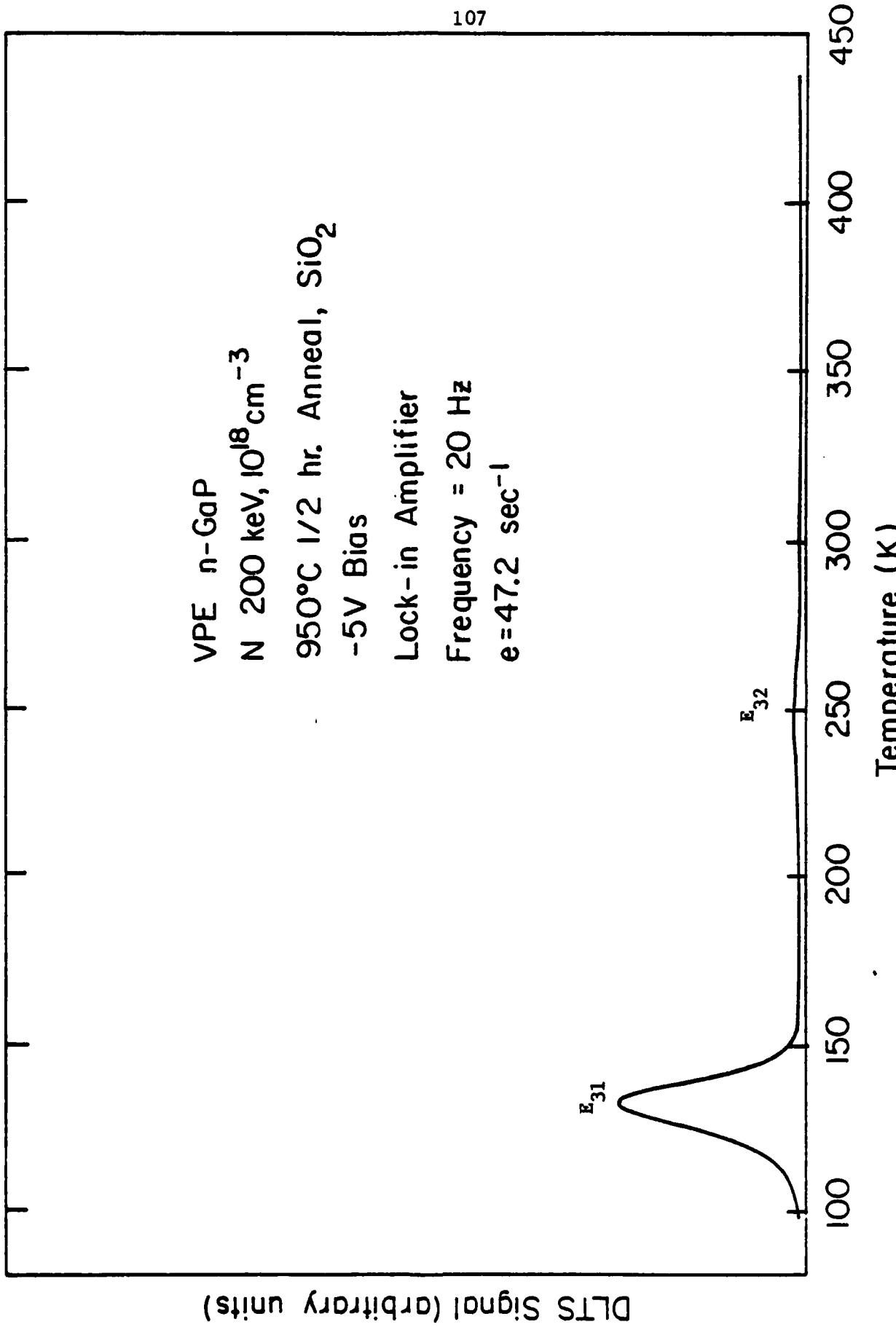


Fig. 4.25 DLTS spectrum of electron traps in N implanted GaP with 10^{18} cm^{-3} peak concentration.

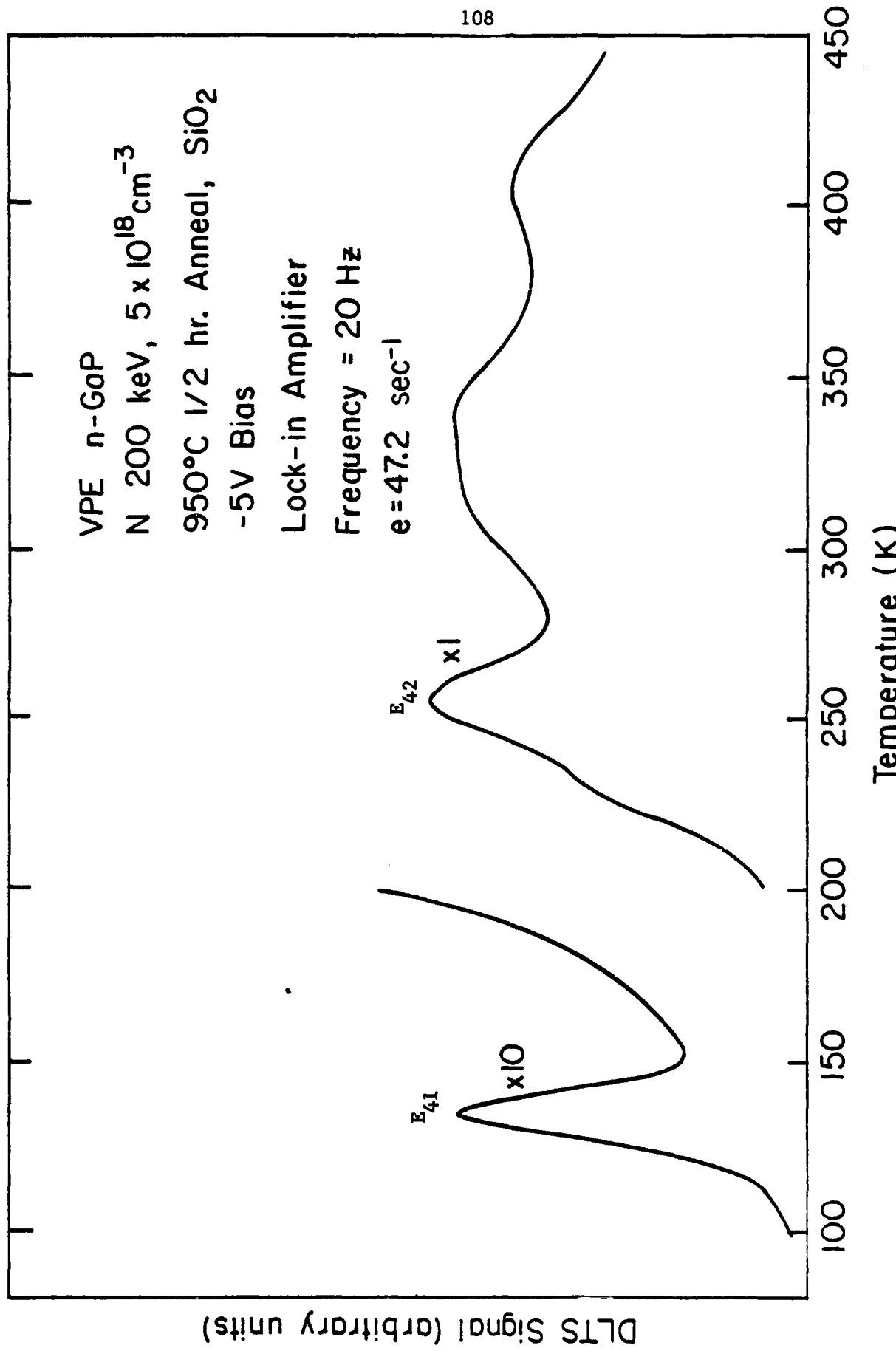
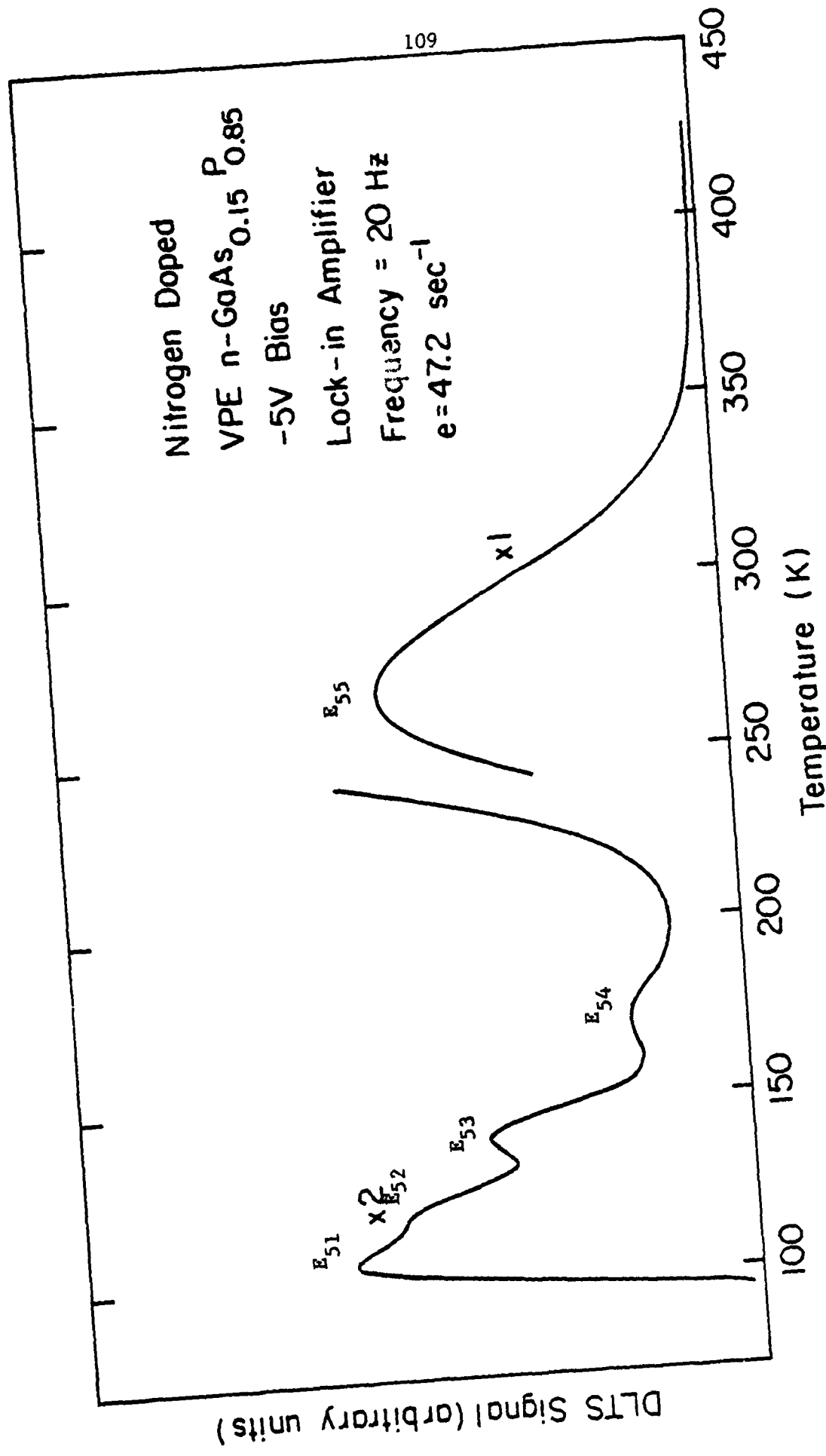


Fig. 4.26 DLTS spectrum of electron traps in N implanted GaP with $5 \times 10^{18} \text{ cm}^{-3}$ peak concentration.



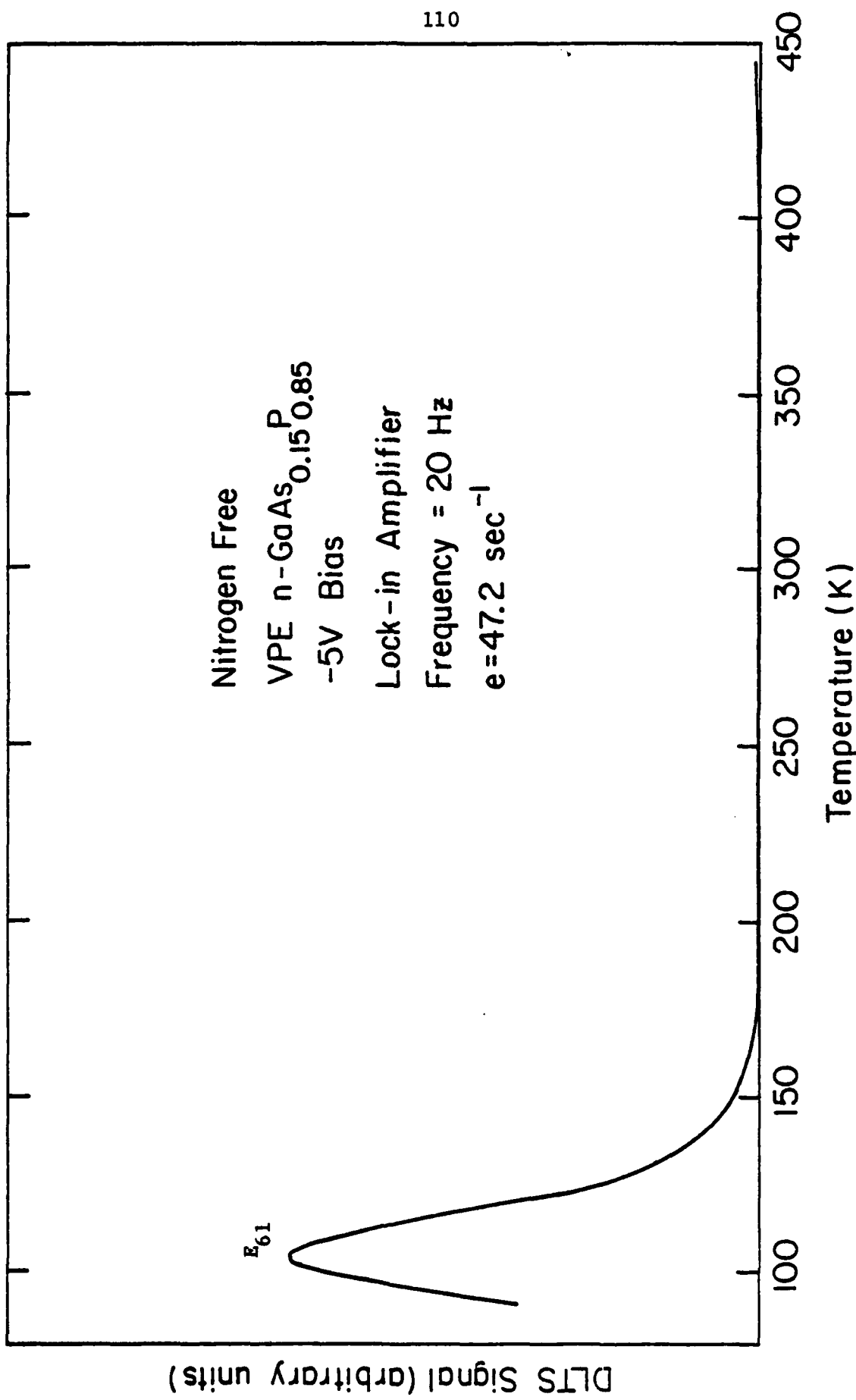


Fig. 4.28 DLTS spectrum of electron traps in N-free GaAs_{0.15}P_{0.85}.

sections for the levels E_{53} , E_{54} , and E_{55} are listed in Table 4.4. The capture cross section calculation is based on Eq. (2.13) and Eq. (4.4). Presently we cannot resolve the energy levels for E_{51} and E_{52} . We can estimate their activation energies by assuming the parameters in Eq. (2.13) such that [66]

$$e_n = k e^{-\Delta E/k_B T} \quad (4.5)$$

where k is a constant for all levels in this sample, i.e. assuming the same capture cross section σ_n . With these assumptions, the energy levels for E_{51} and E_{52} would be 0.19 eV and 0.22 eV, respectively. As shown in Fig. 4.28, levels corresponding to E_{52} - E_{55} in the N-doped samples are again not observable in the N-free sample.

4.2.4 Electron traps in VPE n-GaAs_{0.35}P_{0.65}

Shown in Fig. 4.29 is the DLTS spectrum of electron traps in N-doped GaAs_{0.35}P_{0.65}. Two overlapping levels are observed, and we cannot resolve their activation energies. However, as shown in Fig. 4.30, the energy level for E_{81} is estimated to be 0.41 eV in the N-free sample. Again, the spectrum in the N-doped sample is different from the N-free sample. The evidence supports that E_{72} and E_{81} may be from the same origin. The energy level of E_{81} is very close to that obtained for the sulfur-related deep level [28], which was not detected in GaP but was observable in the alloys with composition $0.20 \leq x \leq 0.65$. Shown in Fig. 4.31 is the spectrum for samples implanted at 200 keV with N peak concentration of $1 \times 10^{18} \text{ cm}^{-3}$ and annealed at 950°C for 1/2 hr with SiO₂ encapsulation. The levels E_{91} and E_{92} are very similar to the levels E_{71} and E_{72} in the N-doped samples. The level E_{91} is estimated to be 0.26 eV below the conduction band. There is a small peak of 0.59 eV in

Table 4.4 Thermal Activation Energies and Capture Cross Sections for Traps in VPE n-GaAs_{1-x}P_x Alloys

Trap	Activation Energy (eV)	Capture Cross-Section (cm ²)	Temperature Range (°K)
E ₁₁	0.24	2.07x10 ⁻¹⁶	135-160
E ₁₂	0.27	3.28x10 ⁻¹⁷	160-185
E ₁₃	0.46	1.49x10 ⁻¹⁴	205-240
E ₂₁	0.19	1.95x10 ⁻¹⁷	125-160
E ₃₁	0.23	9.35x10 ⁻¹⁷	130-160
E ₃₂	0.57	2.52x10 ⁻¹⁴	250-285
E ₄₁	0.24	2.07x10 ⁻¹⁶	135-160
E ₄₂	0.55	4.0x10 ⁻¹⁵	255-295
E ₅₃	0.25	3.24x10 ⁻¹⁶	135-160
E ₅₄	0.32	5.13x10 ⁻¹⁶	170-200
E ₅₅	0.52	3.20x10 ⁻¹⁶	265-320
E ₈₁	0.41	4.38x10 ⁻¹⁴	180-210
E ₉₁	0.26	7.06x10 ⁻¹⁶	135-165
E ₉₃	0.59	9.89x10 ⁻¹⁴	245-280
D ₁	0.13	9.20x10 ⁻¹⁷	95-130
D ₂	0.18	2.69x10 ⁻¹⁶	125-160
D ₃	0.29	1.59x10 ⁻¹⁵	140-165

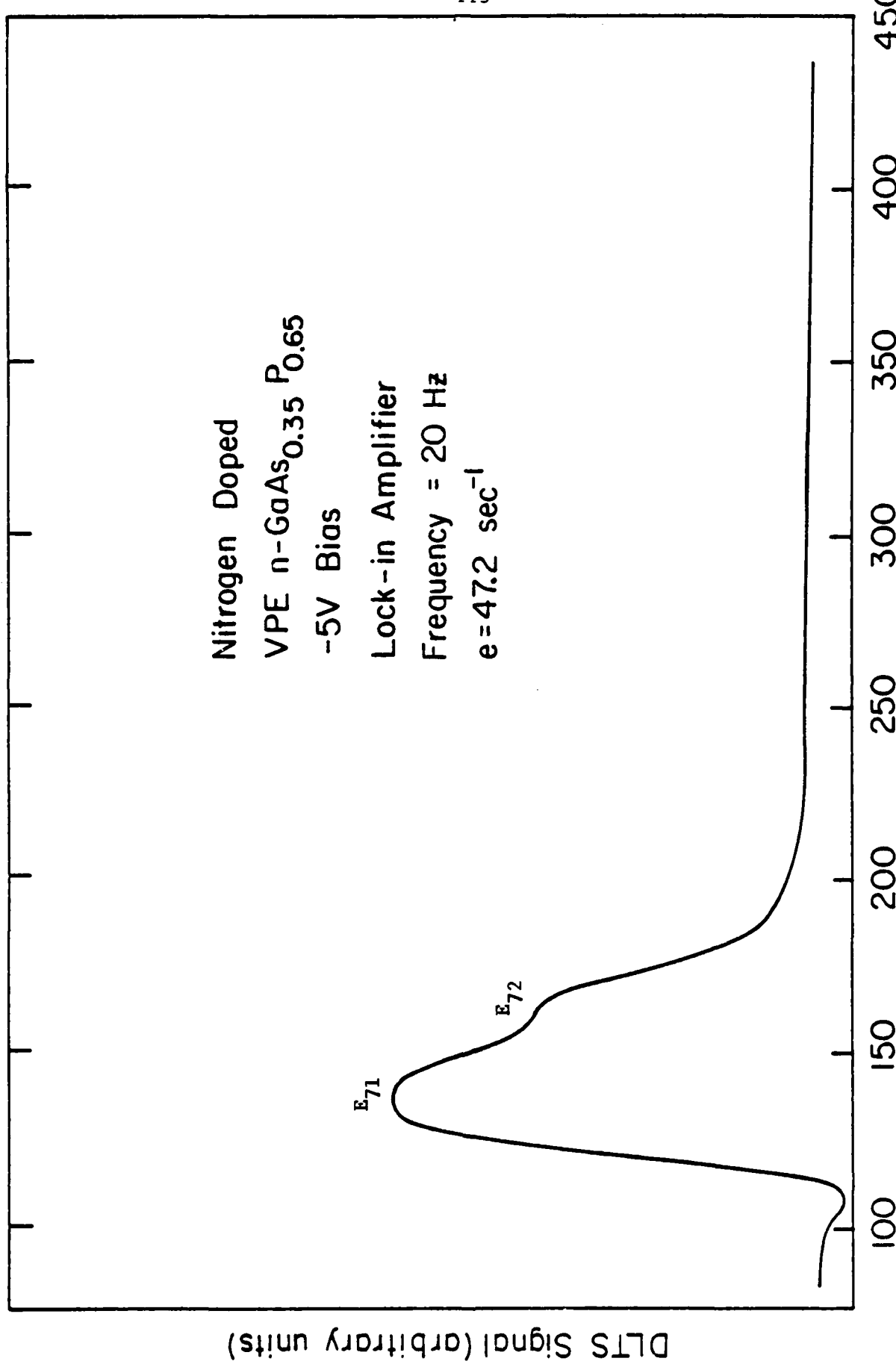


Fig. 4.29 DLTS spectrum of electron traps in N-doped GaAs_{0.35}P_{0.65}.

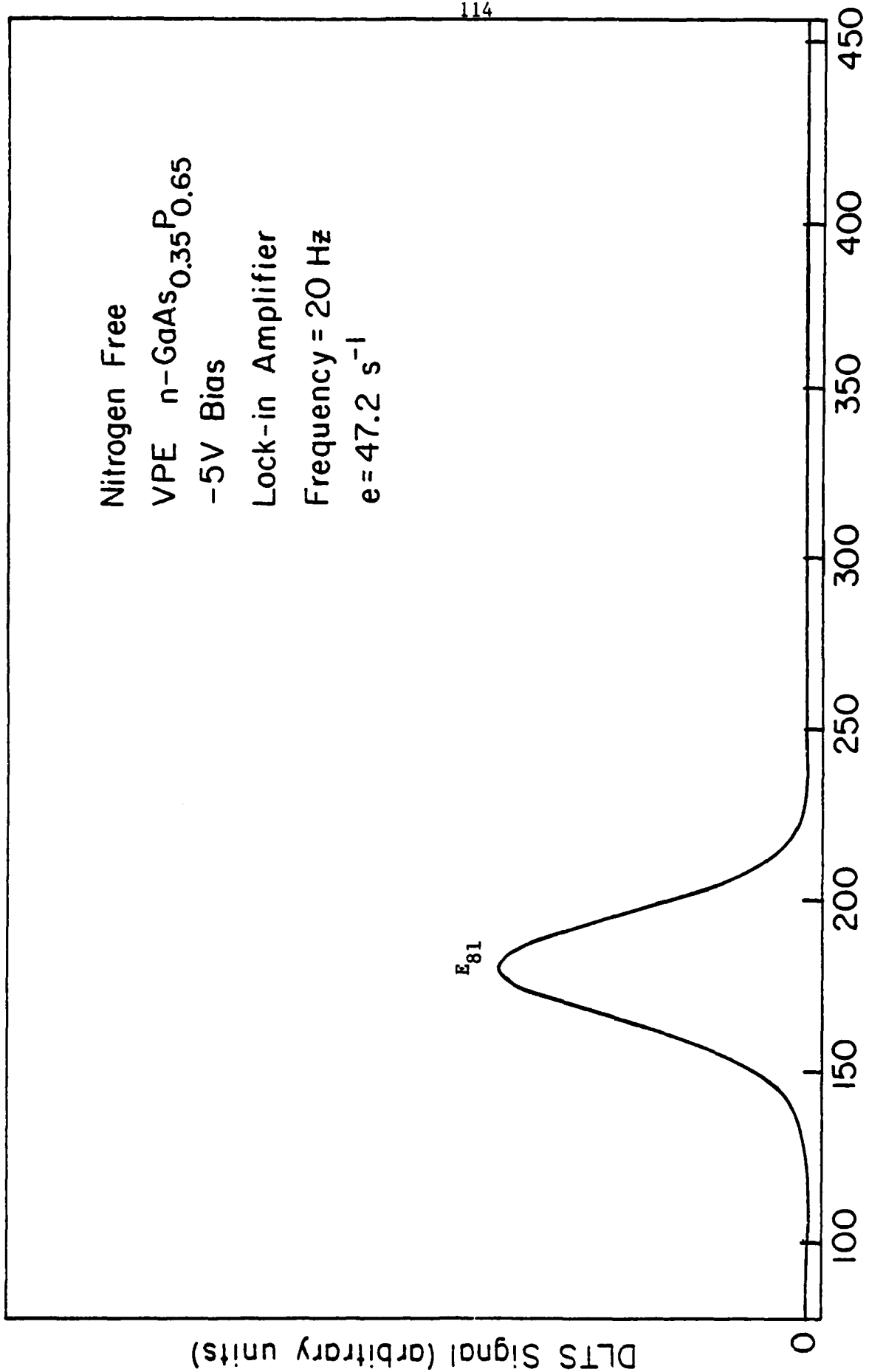


Fig. 4.30 DLTS spectrum of electron traps in N-free GaAs_{0.35}P_{0.65}.

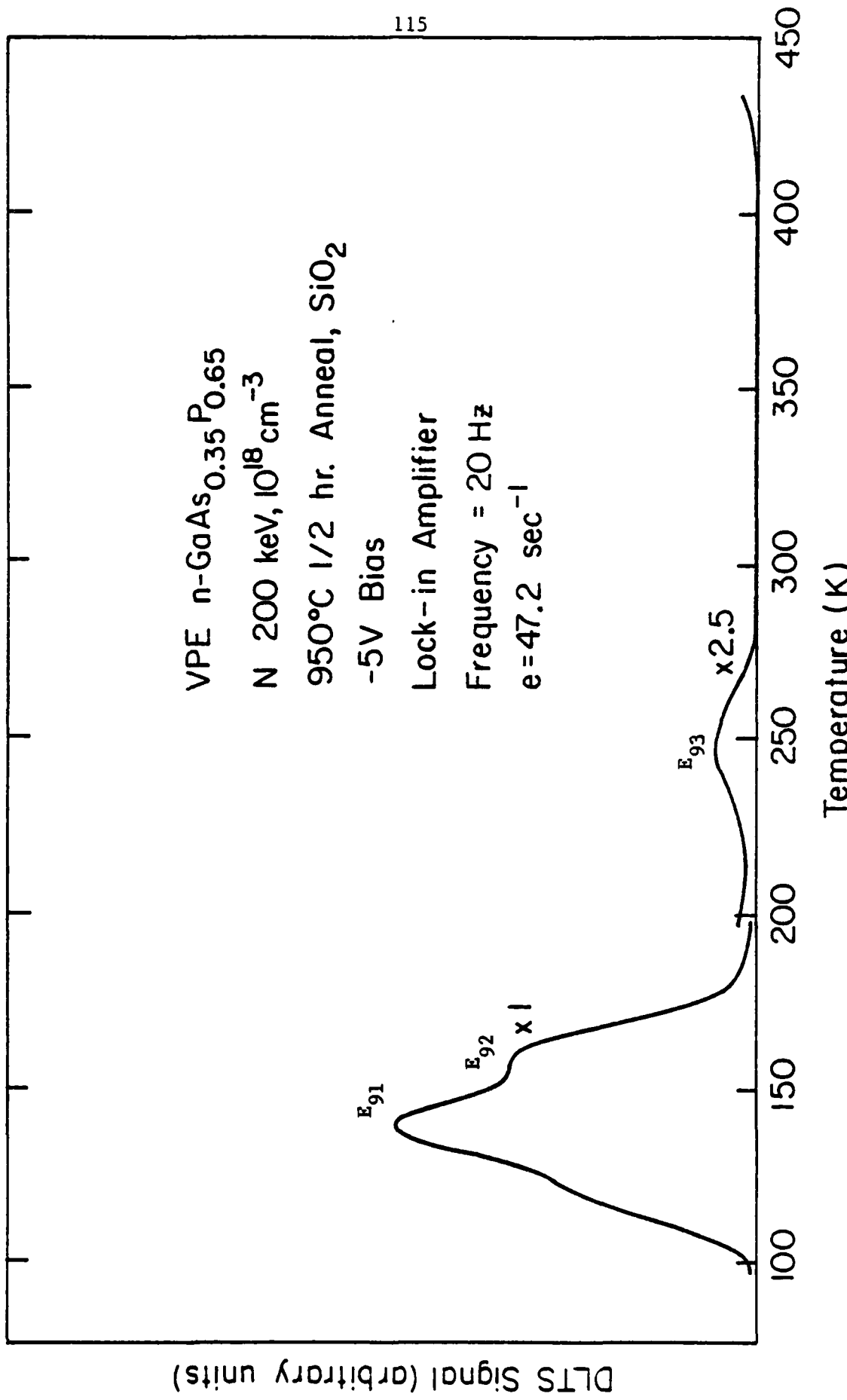


Fig. 4.31 DLTS spectrum of electron traps in N implanted GaAs_{0.35}P_{0.65} with 10¹⁸ cm⁻³ peak concentration.

the medium temperature range and an even smaller peak at the high temperature range. These two peaks are assumed to be related to the N-implant. Shown in Fig. 4.32 is the spectrum for samples implanted at 200 keV with N peak concentration of $5 \times 10^{18} \text{ cm}^{-3}$. We can see that there is a very broad peak due to radiation-induced damage. The levels E'_{91} and E'_{92} are assumed to be the same as E_{91} and E_{92} in Fig. 4.31, because they occur at the same temperature for a given rate window.

4.2.5 Electron traps in VPE n-GaAs_{0.60P_{0.40}}

Since GaAs_{0.60P_{0.40}} is a direct bandgap alloy and the epilayer is doped with Te without the addition of N, we expect a DLTS spectrum different from that for the indirect bandgap alloys, in terms of activation energies and capture cross sections. As shown in Fig. 4.33 the energy levels are estimated to be 0.13, 0.18 and 0.29 eV for D_1 - D_3 . The capture cross sections are calculated from Eq. (2.13) by assuming $m^* = 0.089 m_e$ and $m_{dn}^* = 0.089 m_e$ following the equation [89]

$$m^* = (0.068 + 0.052 x) m_e \quad (4.5)$$

and $m^* = m_{dn}$

for the Γ band minimum.

In this section we have examined the electron traps in VPE n-GaAs_{1-xP_x} alloys with several compositions. It is observed that the DLTS spectra for the unimplanted GaAs_{1-xP_x} alloys are similar to each other. It would be interesting to establish a relationship among them and a unified theoretical explanation for the variations in the activation energies. There are differences in DLTS spectra among the N-doped, N-free, and N-implanted samples for the same alloy composition. The existence of nitrogen might play an important role in the formation

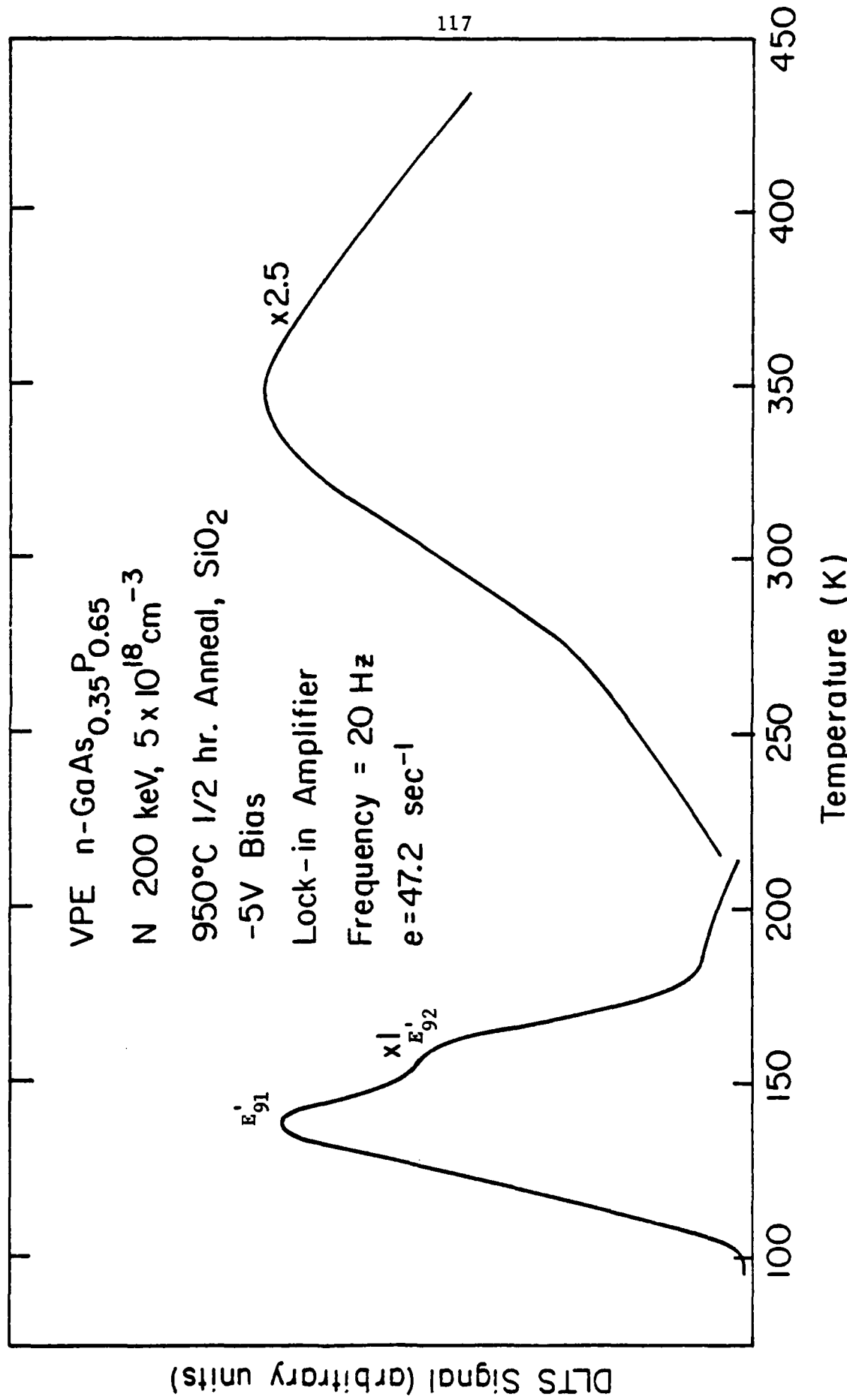


Fig. 4.32 DLTS spectrum of electron traps in N implanted GaAs_{0.35}P_{0.65} with $5 \times 10^{18} \text{ cm}^{-3}$ peak concentration.

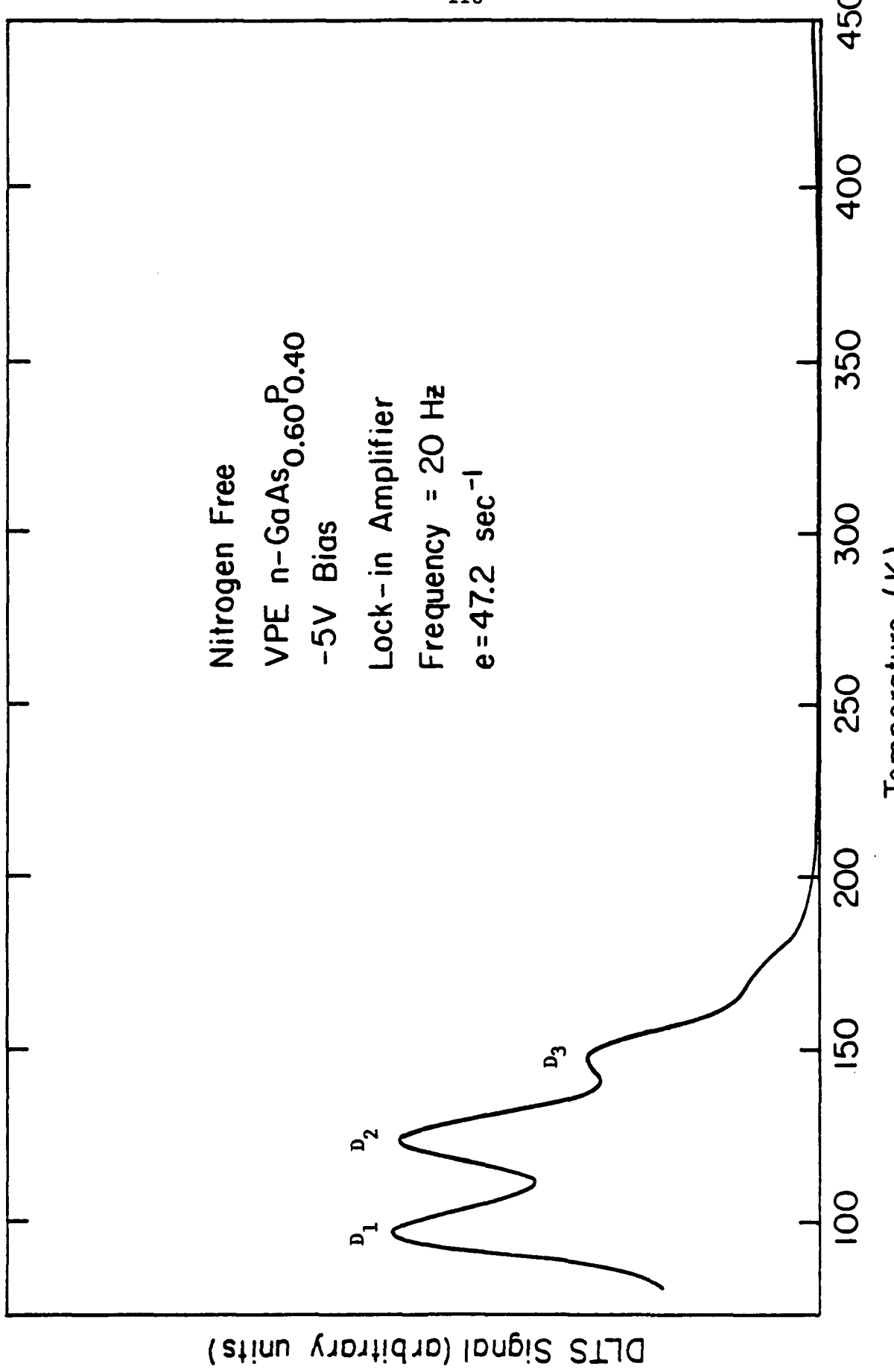


Fig. 4.33 DLTS spectrum of electron traps in GaAs_{0.60}P_{0.40}*

of deep levels in $\text{GaAs}_{1-x}\text{P}_x$ alloys. Deep levels caused by the radiation-induced damage are observable in the N-implanted samples even annealed at 950°C for 1/2 hr with SiO_2 encapsulation. This study is intended as an initial survey, which is necessary for further investigations of this material.

5. SUMMARY AND CONCLUSION

In this work, detailed studies of the various types of deep level transient spectroscopy systems have been made. A special DLTS system has been developed, employing a two-diode method to balance the diode leakage currents at any temperature range. Using this DLTS system, we have studied the main electron trap in VPE n-GaAs. The results suggest that this deep level involves a Ga vacancy. We have also examined the electron traps in VPE GaP and several $\text{GaAs}_{1-x}\text{P}_x$ ternary alloys. In the following sections the results and conclusions of this work are summarized, and suggestions for further investigations are noted.

5.1 DLTS Studies

The typical DLTS system using a commercial capacitance meter (shown in Fig. 3.1) is simple to operate. It is also easy to calibrate the magnitude of the capacitance transient. This system has the drawback of pulse distortion caused by the pulse transformer in addition to the slow system response time. The system shown in Fig. 3.2 eliminates the use of the pulse transformer. Pulse distortion is critical in the capture rate measurement where a pulse with fast transition is required. The slow response time of a commercial capacitance meter together with the system overloading problem during the pulse period make it necessary to gate-off the signal during the initial period of the capacitance transient in order to avoid spurious electrical effects. As a consequence, the capacitance transient after gating-off loses significant information if the gate-off period is comparable to the periodic pulsing period. Special caution and correction for data analysis are required if a lock-in amplifier is used to preset the rate window. In a system employing a

dual-channel boxcar averager, it is possible to avoid problems arising from this gate-off requirement by setting the first sampling instant to occur after the gate-off period.

In this work, the gate-off effect in the lock-in amplifier case has been studied in detail. The basic operation of a lock-in amplifier for the DLTS system has been described in Appendix A. Three operation modes are suggested, dealing mainly with the lock-in phase setting which is critical to the data analyses, including thermal emission time constant and trap concentration calculations. The maximum signal mode and the truncated-transient phase reference mode show considerable shifts in the rate window relationship τ_{\max}/T_0 as a function of lock-in frequency as shown in Fig. 3.14. The bias-pulse phase reference mode is much less frequency sensitive, and this is clearly the best choice for those who prefer lock-in operation. In a system employing the dual-channel boxcar averager, the measurements are typically made using a relatively wide gate rather than the generally assumed narrow gate, because the signal-to-noise (S/N) ratio is better for larger gate widths. The thermal emission time constant corresponding to the temperature where the DLTS peak occurs can be solved exactly from Eq. (3.3). As a relatively good approximation to this exact calculation, the midpoint of the gate can be used to calculate the thermal emission time constants by Eq. (3.4).

The improved DLTS system shown in Fig. 3.5 was originated from that invented by Lang [8], and has a fast response time of $1-2\mu\text{sec}$. Using this system, the gate-off effect in the lock-in amplifier case is negligible because the gate-off time is about the same as the pulse duration, which is small compared to the typical lock-in period. However,

it is difficult to use this system to study devices which have large leakage currents. The leakage current is highly temperature sensitive, and is often encountered in implanted junctions if the post-implant annealing condition is not adequate. A DLTS system using a two-diode method has been developed for such functions. The experimental results show that the two-diode version is essential for accurate measurements on diodes exhibiting large leakage currents.

5.2 Studies of Electron Traps in GaAs

A variety of electron traps in VPE n-GaAs have been reported by several authors [22,23,52-55]. The dominant trap with an activation energy of 0.83eV has not yet been identified conclusively. This level has been conjectured to be related to either a Ga vacancy or an oxygen impurity. The capture cross sections we obtained from emission rate and capture rate measurements further support the model proposed by Majerfeld et al [61] that the transition is between the deep level and the L minima instead of the Γ minimum. The trap concentration decreases in the unencapsulated sample after anneal at 700-750°C for $\frac{1}{2}$ hr, while it is unchanged in the unencapsulated sample after anneal at 750°C with As over pressure for $\frac{1}{2}$ hr. The trap concentration increases in the Si_3N_4 or SiO_2 encapsulated sample after anneal at 800°C for $\frac{1}{2}$ hr. From isothermal and isochronal anneals under various ambient or encapsulations, this dominant trap concentration seems to be related to the Ga vacancy.

Samples implanted with B, Be, Ga, O, and N are also investigated. From the B, Be, and Ga implants, we find that the trap concentrations are much lower in the implanted and annealed samples than those in the unimplanted samples which are annealed at the same condition. These results

are apparently due to the fact that the implanted species tend to occupy Ga vacancy sites substitutionally. For the O implant, we find that the trap concentration does not change significantly compared to the unimplanted sample through the same annealing process. This indicates that this dominant trap is not related to O. We find that the trap concentration increases with N implantation, apparently due to the incorporation of N into As vacancy sites. From this study, we suggest that the dominant electron trap in VPE n-GaAs is related to the Ga vacancy.

5.3 Studies of Electron Traps in $\text{GaAs}_{1-x} \text{P}_x$ Alloys

Studies of electron traps in GaP have been reported by several authors [24-28, 52, 53]. However, the discrepancy of the energy levels obtained under different experimental conditions is still unresolved. The lack of experimental information in GaP as well as the $\text{GaAs}_{1-x} \text{P}_x$ ternary alloy motivated us to do further studies by the DLTS method. For GaP, we find that the DLTS spectra are different for N-doped and N-free samples. From N implanted material we observe a level with activation energy between those in the N-free and N-doped samples. Further study is necessary to verify whether these levels are from the same physico-chemical origin, perhaps modified by the presence of nitrogen. There are two electron traps observed in the N-doped samples but not detectable in the N-free sample or the N-implant sample with $1 \times 10^{18} \text{ cm}^{-3}$ peak concentration. It is possible that these two traps are overwhelmed by the radiation damage in the N-implanted sample. In that case, these two levels might be related to the N doping. We also find deep levels related to radiation-induced damage in the sample implanted at 200 keV with $5 \times 10^{18} \text{ cm}^{-3}$ N peak concentration, even after 950°C anneal for $\frac{1}{2}$ hr. with SiO_2

encapsulation.

For the $\text{GaAs}_{0.15}\text{P}_{0.85}$ alloy, we also find that the DLTS spectra for the N-doped and N-free samples are different. For $\text{GaAs}_{0.35}\text{P}_{0.65}$, a level with activation energy close to that previously reported as a sulfur-related deep level [28] is observed in the N-free sample. However, this level is not clearly resolved in the N-doped $\text{GaAs}_{0.35}\text{P}_{0.65}$, and is not detectable in the GaP and $\text{GaAs}_{0.15}\text{P}_{0.85}$ material which is doped with S as a shallow donor. We also observe deep levels in this alloy associated with radiation-induced damage in the sample implanted at 200 keV with N peak concentration of $5 \times 10^{18} \text{ cm}^{-3}$ after high temperature anneal. For the $\text{GaAs}_{0.60}\text{P}_{0.40}$, which is a direct bandgap material, a DLTS spectrum with levels shallower than those in GaP is obtained. Although the deep levels in $\text{GaAs}_{1-x}\text{P}_x$ alloys are quite divergent, there are common features, such as the similarity in the DLTS spectra for the unimplanted samples and the difference between the N-doped and N-free samples with the same alloy composition.

5.4 Suggestions for Further Investigations

As pointed out in Section 4.1.3, the main electron trap V7 (0.83eV) in VPE n-GaAs is not detected in the typical LPE and MBE n-GaAs. However, it is observed in the LPE and MBE samples annealed at 800°C for $\frac{1}{2}$ hr with Si_3N_4 or SiO_2 encapsulation. A detailed annealing study should be made to establish a unique explanation of this level in epitaxial n-GaAs. It is also interesting to see whether this level will be created by changing the stoichiometric ratio of Ga to As during the MBE crystal growth.

The role of oxygen in GaAs and $\text{GaAs}_{1-x}\text{P}_x$ is not clear yet. It is worthwhile to do a systematic study on oxygen implanted samples with

available alloy compositions by the DLTS and photoluminescence methods to obtain the thermal and optical properties of oxygen in the alloys. The effect of nitrogen doping on the deep level behavior in $\text{GaAs}_{1-x}\text{P}_x$ should also be investigated further. It would be a great achievement to establish a theoretical explanation for the deep level formation in this compound alloy, based upon a combination of DLTS results with the extensive optical data of Wolford et al. [81,87].

REFERENCES

1. W. Shockley and W. T. Read, Jr., Phys. Rev., 87, 835 (1952).
2. R. N. Hall, Phys. Rev., 87, 387 (1952).
3. C. T. Sah and W. Shockley, Phys. Rev., 109, 1103 (1958).
4. C. H. Henry, J. Electron. Mater., 4, 1037 (1975).
5. C. T. Sah, L. Forbes, L. L. Rosier, and A. F. Tasch, Jr., Solid State Electron., 13, 759 (1970).
6. C. T. Sah, Solid State Electron., 19, 975 (1976).
7. H. Kukimoto, C. H. Henry, and F. R. Merritt, Phys. Rev. B, 7, 2486 (1973).
8. D. V. Lang, J. Appl. Phys., 45, 3023 (1974).
9. G. L. Miller, D. V. Lang, and L. C. Kimerling, Ann. Rev. Mater. Sci., 7, 377 (1977).
10. K. L. Wang and A. O. Ewvaraye, J. Appl. Phys., 47, 4574 (1976).
11. N. M. Johnson, Appl. Phys. Lett., 34, 802 (1979).
12. B. Hamilton and A. R. Peaker, Solid State Electron., 21, 1513 (1978).
13. J. F. Gibbons, Proc. IEEE, 60, 1062 (1972).
14. L. C. Kimerling and J. M. Poate, Inst. Phys. Conf. Ser., No. 23, 126 (1975).
15. A. G. Klimenko, E. A. Klimenko, and V. I. Donin, Sov. J. Quantum Electron., 5, 1289 (1976).
16. G. A. Kachurin, N. B. Pidachin, and L. S. Smirnov, Sov. Phys. Semicond., 9, 946 (1976).
17. A. Gat, J. F. Gibbons, T. J. Magee, J. Peng, V. R. Deline, P. Williams, and C. A. Evans, Jr., Appl. Phys. Lett., 32, 276 (1978).
18. G. A. Kachurin, E. V. Nidaev, A. V. Khodyachikh, and L. A. Kovaleva, Sov. Phys. Semicond., 10, 1128 (1976).
19. J. C. C. Fan, J. P. Donnelly, C. O. Bozler, and R. L. Chapman, Inst. Phys. Conf. Ser., No. 45, 472 (1979).
20. T. I. Kamins and A. G. Greenwald, Appl. Phys. Lett., 35, 3, 282 (1979).
21. T. Yu, K. J. Soda and B. G. Streetman, unpublished.

22. A. Mircea and A. Mitonneau, *Appl. Phys.*, 8, 15 (1975).
23. F. Hasegawa and A. Majerfeld, *Electron. Lett.*, 12, 52 (1976).
24. D. V. Lang and L. C. Kimerling, *Appl. Phys. Lett.*, 28, 248 (1976).
25. C. H. Henry and P. Dapkus, *J. Appl. Phys.*, 47, 4067 (1976).
26. B. W. Wessels, *J. Appl. Phys.*, 48, 1656 (1977).
27. B. Tell, and F. P. J. Kuijpers, *J. Appl. Phys.*, 49, 5938 (1978).
28. R. A. Craven and D. Finn, *J. Appl. Phys.*, 50, 6334 (1979).
29. C. T. Sah, in "Semiconductor Silicon 1977," *Electrochem. Soc.* (1977).
30. L. C. Kimerling, *IEEE Trans. Nucl. Sci.*, NS-23, 1497 (1976).
31. G. L. Miller, J. V. Ramirez, and D. A. H. Robinson, *J. Appl. Phys.*, 46, 2638 (1975).
32. J. T. Schott, H. M. Deangelis, and W. R. White, *Air Force Cambridge Research Laboratories Report AFCRL-TR-76-0024* (1976).
33. C. H. Henry and D. V. Lang, *Phys. Rev. B*, 15, 989 (1977).
34. M. Lax, *Phys. Rev.*, 119, 1502 (1960).
35. A. G. Milnes, Deep Impurities in Semiconductors, Wiley, New York (1973).
36. J. F. Gibbons, W. S. Johnson, and S. W. Mylroie, Projected Range Statistics, 2nd edition, Halstead Press, Stroudsburg, Penn. (1975).
37. S. Lindhard, M. Scharff, and H. Schiott, *Mat. Fys. Medd. Dan. Vid. Selsk.*, 33, 1 (1963).
38. J. F. Gibbons, *Proc. IEEE*, 56, 295 (1968).
39. M. Schulz, *Appl. Phys.*, 4, 91 (1974).
40. M. Y. Tsai, *Ph.D. Thesis (University of Illinois)*, Coordinated Science Laboratory Report R-824 (1978).
41. D. S. Day, K. J. Scia, and B. G. Streetman, unpublished.
42. S. T. Picraux, in "Ion Implantation in Semiconductors and Other Material," B. L. Crowder, Editor, p., 641, Plenum Press, New York (1973).
43. M. J. Helix, K. V. Vaidyanathan, B. G. Streetman, H. B. Dietrich, and P. K. Chatterjee, *Thin Solid Films*, 55, 143 (1978).

44. M. J. Helix, Ph.D. Thesis (University of Illinois), Coordinated Science Laboratory Report R-858 (1979).
45. K. V. Vaidyanathan, M. J. Helix, D. J. Wolford, B. G. Streetman, R. J. Blattner, and C. A. Evans, Jr., J. Electrochem. Soc., 124, 178 (1977).
46. D. S. Day, M. Y. Tsai, B. G. Streetman, and D. V. Lang, J. Appl. Phys., 50, 5093 (1979).
47. G. Bemski, Phys. Rev., 111, 1515 (1958).
48. M. G. Buehler and W. E. Phillips, Solid State Electron., 19, 777 (1976).
49. C. T. Sah and V. G. K. Reddi, IEEE Trans. ED-11, 345 (1964).
50. D. V. Lang, J. Appl. Phys., 45, 3014 (1974).
51. D. S. Day, M. J. Helix, K. Hess, and B. G. Streetman, Rev. Sci. Instrum., 50, 1571 (1979).
52. D. V. Lang, Inst. Phys. Conf. Ser. No. 31, 70 (1977).
53. A. Mircea and D. Bois, Inst. Phys. Conf. Ser. No. 46, 82 (1979).
54. F. Hasegawa and A. Majerfeld, Electron. Lett., 11, 286 (1975).
55. Tsugunori Okumura, Masahiko Takikawa, and Toshiaki Ikoma, Appl. Phys. 11, 187 (1976).
56. N. M. Kolchanova, G. N. Talakin, and E. A. Kretova Sov. Phys. - Semicond. 4, 174 (1970).
57. A. Mircea, A. Mitonneau, L. Hollan, and A. Briere, Appl. Phys. 11, 153 (1976).
58. C. H. Henry and D. V. Lang, Proc. 12th Intern. Conf. Phys. Semicond. 411 (1974).
59. S. M. Sze, "Physics of Semiconductor Devices", John Wiley & Son, Inc. (1969).
60. A. Mircea, A. Mitonneau, and J. Vannimenus, J. Phys. (Paris) 38, L 41 (1977).
61. A. Majerfeld and P. K. Bhattacharya, Appl. Phys. Lett. 33, 259 (1958).
62. A. M. White, P. J. Dean, and P. Porteous, J. Appl. Phys. 47, 3230 (1976).
63. A. Zyibersztein, R. H. Wallis, and J. M. Besson, Appl. Phys. Lett. 32, 764 (1978).

64. A. M. White, P. Porteous, W. F. Sherman, and A. A. Stadtmuller, J. Phys. C10, L 473 (1977).
65. D. E. Aspnes, Inst. Phys. Conf. Ser. No. 33b, 110 (1977).
66. J. A. Van Vechten and C. D. Thurmond, Phys. Rev. B14, 3539 (1976).
67. P. K. Bhattacharya, A. Majerfeld, and A. K. Saxena, Inst. Phys. Conf. Ser. No. 45, 199 (1979).
68. O. Wada, A. Majerfeld, and N. M. M. Choudhury, J. Appl. Phys. 51, 423 (1980).
69. D. V. Lang and R. A. Logan, J. Electron. Mater., 4, 1053 (1975).
70. D. V. Lang, A. Y. Cho, A. C. Gossard, M. Illegems, and W. Wiegmann, J. Appl. Phys., 47, 2558 (1976).
71. G. E. Stillman, "Microstructure Science, Engineering, and Technology", National Academy of Science (1979).
72. H. Morkoç, Private Communication.
73. B. Toulouse, P. N. Favennec, A. Guivar'h, and G. Pelous, Inst. Phys. Conf. Ser. No. 45, 501 (1979).
74. M. J. Helix, K. V. Vaidyanathan, and B. G. Streetman, IEEE J. Solid State Circuit, SC-13, 426 (1978).
75. W. V. Mclevige, M. J. Helix, K. V. Vaidyanathan, and B. G. Streetman, J. Comas, and L. Plew, Solid State Communication, 25, 1003 (1978).
76. N. D. Wiley, J. Comas, and R. N. Shelby, Inst. Phys. Conf. Ser. No. 46, 487 (1979).
77. A. M. Huber, N. T. Linh, M. Valladon, J. L. Debrun, G. M. Martin, A. Mitonneau, and A. Mircea, J. Appl. Phys., 50, 4022 (1979).
78. P. N. Favennec, J. Appl. Phys., 47, 2532 (1976).
79. B. Deveaud and P. N. Favennec, Inst. Phys. Conf. Ser. No. 45, 492 (1978).
80. D. E. Davies, J. K. Kennedy, and A. C. Yang, Appl. Phys. Lett., 23, 11, 615 (1973).
81. D. J. Wolford, W. Y. Hsu, J. D. Dow, and B. G. Streetman, J. Lum., Vol. 18/19, 863 (1979).
82. W. O. Groves, A. H. Herzog, and M. G. Crawford, Appl. Phys. Lett., 19, 184 (1971).

83. M. G. Crawford, G. E. Stillman, J. A. Rossi, and N. Holonyak, Jr., *Phys. Rev.*, 168, 867 (1968).
84. N. Holonyak, Jr., D. R. Scifres, R. D. Burnham, M. G. Crawford, W. O. Groves, and A. H. Herzog, *Appl. Phys. Lett.*, 19, 254 (1971).
85. M. G. Crawford, R. W. Shaw, A. H. Herzog, and W. O. Groves, *J. Appl. Phys.*, 43, 4075 (1972).
86. M. G. Crawford, and W. O. Groves, *Proc. IEEE*, 61, 862 (1973).
87. D. J. Wolford, *Ph.D. Thesis (University of Illinois)*, Coordinated Science Laboratory Report R-862 (1979).
88. R. J. Stirn, "Semiconductors and Semimetals", Academic Press, vol. 8, 49 (1972).
89. B. W. Hakki, *J. Appl. Phys.*, 42, 4981 (1971).

APPENDIX A

Lock-in Amplifier Operation and Numerical Computation
Program for the DLTS System

A.1 Lock-in Amplifier Operation

The PAR HR-8 lock-in amplifier has a tuned amplifier to pick up the fundamental Fourier component of the input signal, a mixer which generates a square wave weighting function to multiply with the input fundamental component, and an output stage to take the time average of the mixer output. There is a phase control to adjust the relative phase of the input fundamental component to the mixer weighting function. As depicted in Fig. A.1, it is easy to understand the operation of a lock-in amplifier.

The Fourier components of a periodic function $f(t)$ over the interval $-\frac{1}{2} T_o \leq t < \frac{1}{2} T_o$ are

$$f(t) = \frac{1}{2} a_o + \sum_{n=1}^{\infty} \left[a_n \cos\left(\frac{2\pi n t}{T_o}\right) + b_n \sin\left(\frac{2\pi n t}{T_o}\right) \right]$$

or

$$f(t) = \frac{1}{2} a_o + \sum_{n=1}^{\infty} c_n \sin\left(\frac{2\pi n t}{T_o} + \phi_n\right),$$

where

$$a_n = \frac{2}{T_o} \int_{-T_o/2}^{T_o/2} f(t) \cos\left(\frac{2\pi n t}{T_o}\right) dt,$$

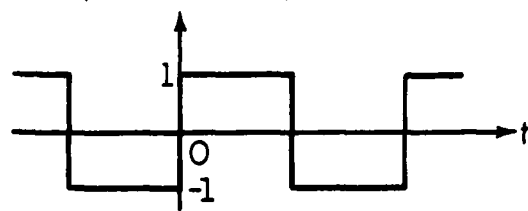
$$b_n = \frac{2}{T_o} \int_{-T_o/2}^{T_o/2} f(t) \sin\left(\frac{2\pi n t}{T_o}\right) dt,$$

and

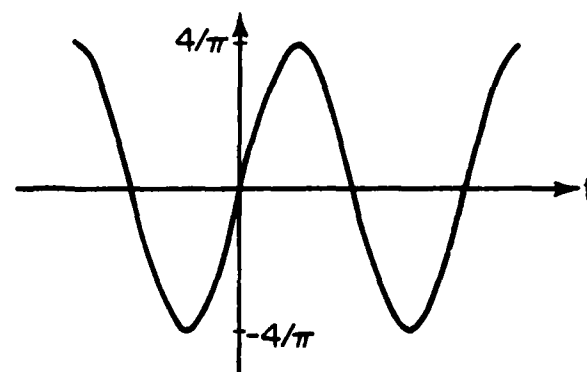
$$c_n = (a_n^2 + b_n^2)^{1/2}, \quad \phi_n = \tan^{-1}\left(\frac{a_n}{b_n}\right)$$

Figure A.1 shows a square wave input, its fundamental component, and the mixer outputs with various lock-in phase settings. The fundamental component is $f_1(t) = c_1 \sin \frac{2\pi t}{T} = \frac{4}{\pi} \sin \frac{2\pi t}{T}$. If we multiply $f_1(t)$ with a

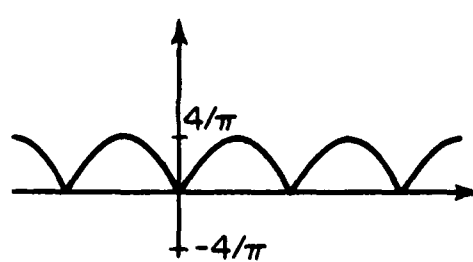
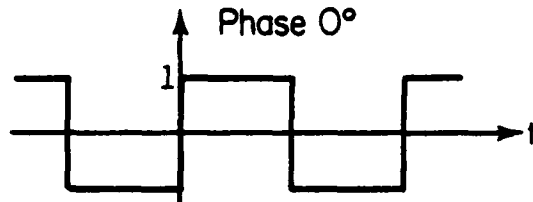
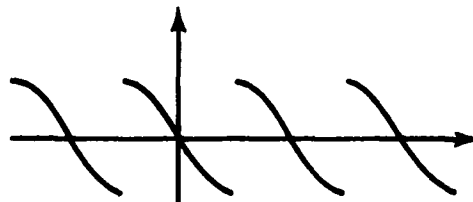
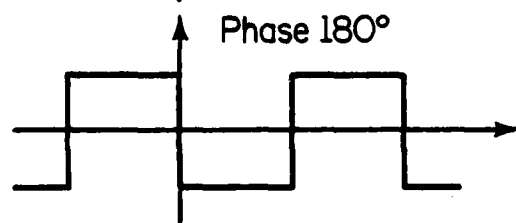
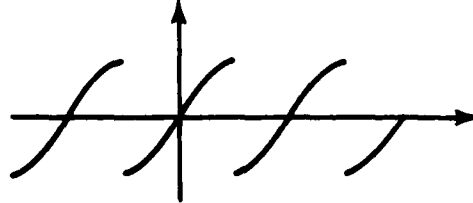
Square Wave Input



Fundamental Fourier Component



Mixer Output

Mixer Weighting Function
and Phase ControlPhase 0° Phase 90° Phase 180° Phase 270° 

LP-1607

Fig. A.1. Operation of lock-in amplifier phase control (Schott [32]).

weighting function $w(t)$ in phase with the input, the time average of the mixer output $f_1(t) w(t)$ is

$$S_o = \frac{1}{T_o} \int_{-T_o/2}^{T_o/2} f_1(t) w(t) dt$$

$$= \frac{8}{\pi^2}$$

The HR-8 lock-in amplifier has a calibrated square wave to calibrate the amplification gain. If the input square wave has the rms value of its fundamental component equal to the lock-in sensitivity setting, the lock-in output is full scale. The peak to peak value of a square wave is 2.22 times the rms value of its fundamental component. Therefore, the rms value of $f_1(t)$ is $2/2.22 = 0.901$. The amplification gain G can be calculated as

$$G \times \frac{8}{\pi^2} / 0.901 = 1 \quad (\text{full scale})$$

$$G = 1.11$$

If the input signal is a periodic exponential train as shown in Fig. A.2,

$$f(t) = \exp\left(-\frac{t_d}{\tau}\right) \exp\left(-\frac{t + T_o/2}{\tau}\right), \quad -\frac{T_o}{2} \leq t < \frac{T_o}{2}$$

The coefficients c_1 and ϕ_1 are

$$c_1 = \exp\left(\frac{-t_d}{\tau}\right) \left[\exp\left(\frac{-T_o}{\tau}\right) - 1 \right] / \left[\left(\frac{T_o}{2\tau}\right)^2 + \pi^2 \right]^{1/2}$$

$$\phi_1 = \tan^{-1} \frac{\frac{T_o}{2}}{2\pi\tau}$$

If the mixer weighting function is set as shown in Fig. A.2, the output $S_o(t_d, \theta, \tau)$ is

$$S_o(t_d, \theta, \tau) = \frac{1}{T_o} \int_{-T_o/2}^{T_o/2} c_1 \sin\left(\frac{2\pi t}{T_o} + \phi_1\right) w(t) dt$$

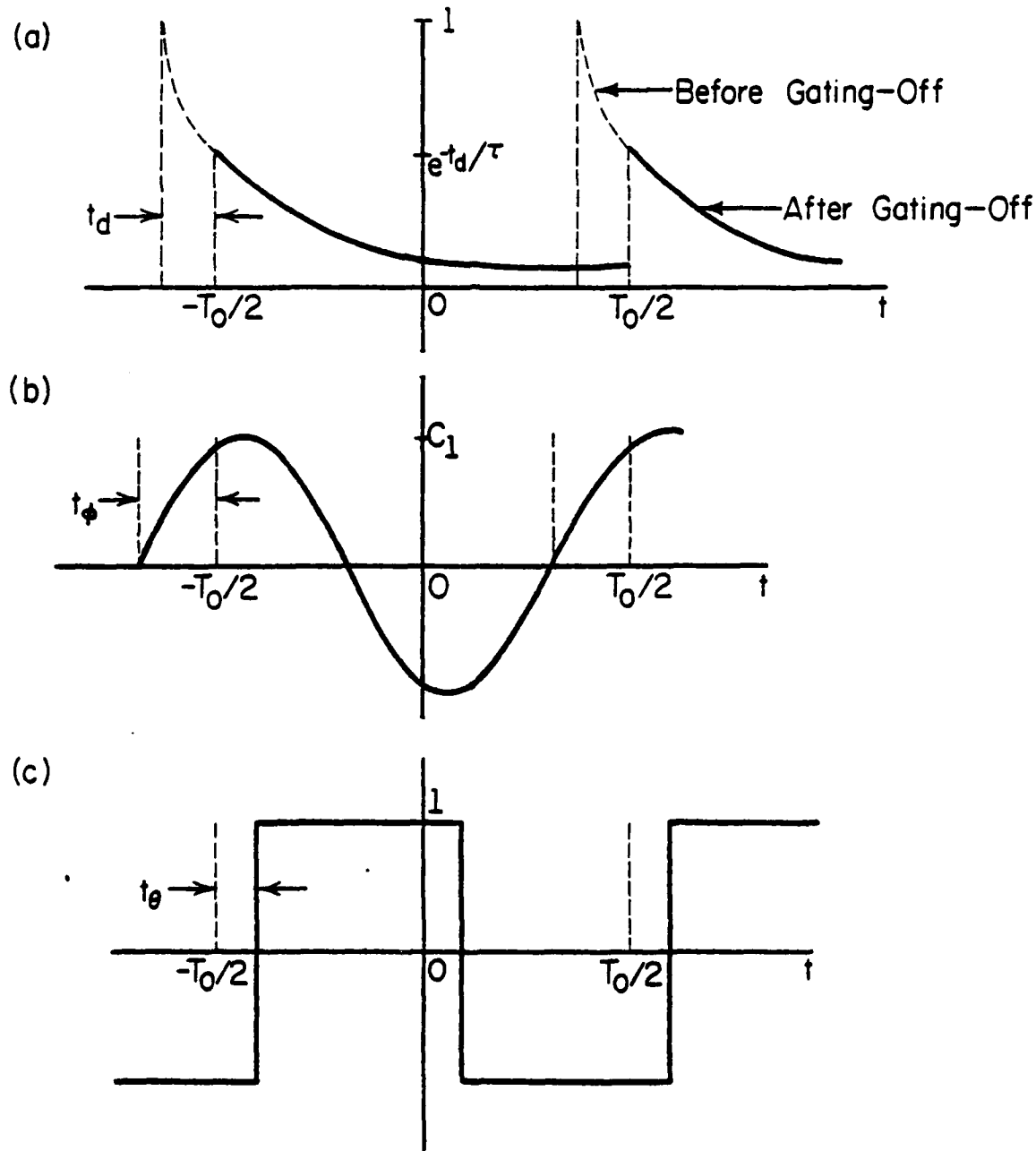


Fig. A.2. Phase adjustment and gate-off effect in the lock-in amplifier case; (a) normalized exponential capacitance transient before and after gating-off; (b) fundamental Fourier component of the transient, $c_1 \sin(2\pi t/T_0 + \phi)$; (c) lock-in amplifier mixer weighting function for phase setting θ (same as Fig. 3.13).

$$= \frac{2}{\pi} \cdot \frac{\exp(-t_d/\tau)[1 - \exp(-T_o/\tau)]}{[(T_o/2\tau)^2 + \pi^2]^{1/2}} \cos(\phi_1 + \theta). \quad (A.1)$$

Where $\theta = \frac{t_\theta}{T_o} \times 360$

The output signal S_o is a function of t_d , θ , and τ . Since t_d is fixed and τ is a function of trap energy level and temperature, only θ can be adjusted freely. There are three convenient ways to adjust lock-in phase setting--maximum signal mode, truncated transient phase reference mode, and bias-pulse phase reference mode. The first mode corresponds to adjusting the lock-in phase to give a maximum DLTS peak for each lock-in frequency. This mode can be easily understood by setting $\theta = -\phi_1$, i.e. the weighting function $w(t)$ is in phase with the fundamental component. The second mode is obtained by setting $w(t)$ in phase with the exponential train after gate-off, i.e. $t_\theta = 0$. In the third mode one sets $w(t)$ in phase with the leading edge of the bias pulse or the exponential train before gating off, i.e. $t_\theta = -t_d$.

The DLTS peak will occur at the τ_{\max} value for which $\frac{dS_o}{d\tau} \Big|_{\tau_{\max}} = 0$ for each mode. During mathematical manipulation, one has to notice that $\cos(\phi_1 + \theta)$ is a function of τ . Generally, it is the numerical solution to

$$\begin{aligned} & \exp(-T_o/\tau) \{ [(\frac{2t_d}{T_o} + 2)((\frac{T_o}{2\tau})^2 + \pi^2) + \frac{T_o}{2\tau}] \cos(\theta + \phi_1) + \pi \sin(\theta + \phi_1) \} \\ & - [(\frac{2t_d}{T_o} ((\frac{T_o}{2\tau})^2 + \pi^2) + \frac{T_o}{2\tau}) \cos(\theta + \phi_1) - \pi \sin(\theta + \phi_1) = 0 \end{aligned} \quad (A.2)$$

The appropriate numerical computation program is given in Section A.3.

A.2. Obtaining ΔC from Lock-in Peak Height

The analog voltage output from the capacitance bridge is $\frac{\Delta C}{S_B} \exp(-t/\tau)$, where S_B is the conversion factor in pF/Volt. As discussed in Section A.1, the actual lock-in peak output is $1.11 \times S_o(\tau_{\max})$. ΔC can be calculated from

$$1.11 \times S_o(\tau_{\max}) \times \left(\frac{\Delta C}{S_B} / S_L \right) = V_L / 10$$

where S_L is lock-in sensitivity

V_L is DLTS peak height

$$\text{then } \Delta C = \frac{S_L \times S_B \times V_L}{11.1 \times S_o(\tau_{\max})}$$

A simplified case is obtained for each mode if $t_d/T_o \ll 1$. For the first mode where $\theta = -\phi_1$,

$$\tau_{\max} \approx 0.3485 T_o$$

$$\theta = -\phi_1 \approx -24.5^\circ$$

$$S_o(\tau_{\max}) \approx 0.1738$$

$$\text{and } \Delta C = 0.518 \times S_L \times S_B \times V_L$$

For the second mode where $\theta = 0$

$$\tau_{\max} = 0.424 T_o$$

$$S_o(\tau_{\max}) = 0.1607$$

$$\text{and } \Delta C = 0.560 \times S_L \times S_B \times V_L$$

The third mode, where $t_d = -t_d = 0$, is the same as the second mode.

A.3 Numerical Computation Program

```

00100 C TO EXECUTE THIS PROGRAM YOU HAVE TO TYPE DLTSLO.FOR, SYS:IMSL/SEAR
00200 C EXTERNAL F
00300 C THIS PROGRAM IS TO CALCULATE THE OPTIMUM THERMAL EMISSION
00400 C TIME CONSTANT, PHASE ANGLE PHI, AND NORMALIZED LOCK-IN
00500 C OUTPUT FOR EACH OF THE THREE MODES
00600 C MAXIMUM-SIGNAL MODE IS THE CASE PHI= -THETA,
00700 C TRUNCATED-TRANSIENT PHASE REFERENCE MODE IS THE CASE
00800 C THETA=0.
00900 C BIAS PULSE PHASE REFERENCE MODE IS THETA=-DELAY/PERIOD
01000 C *360
01100 C ASSIGN N=1,2,3 FOR EACH CASE
01200 C TAUMAX : OPTIMUM TIME CONST, CAP : CAPACITANCE, PHI : PHASE
01300 C ANGLE OF FIRST HARMONIC, THETA : PHASE SETTING
01400 C COMMON A,BN,XL,XR,EPS,NSIG,XAPP,ITMAX,PI
01500 C PI=3.14159
01600 C WRITE(5,10)
01700 10 FORMAT(' DELAY = GATE-OFF PERIOD = ',$,)
01800 READ(5,20) DELAY
01900 20 FORMAT(G)
02000 WRITE(5,30)
02100 30 FORMAT(' LOCK IN PERIOD = ',$,)
02200 READ(5,20) PERIOD
02300 WRITE(5,50)
02400 50 FORMAT(' N=1 FOR FIRST MODE, N=2 FOR SECOND MODE
02500 C N=3 FOR THIRD MODE, INPUT N= ',$,)
02600 READ(5,20) BN
02700 DELAY=DELAY-.05
02800 DO 300 I=1,41
02900 DELAY=DELAY+.05
03000 A=DELAY/PERIOD
03100 XL=0.
03200 XR=3.0
03300 ITMAX=200
03400 EPS=.0001
03500 NSIG=4
03600 CALL ZFALSE(F,EPS,NSIG,XL,XR,XAPP,ITMAX,IER)
03700 TYPE 60 IER
03800 60 FORMAT(' IER = ',I4)
03900 TYPE 70, DELAY, PERIOD, A
04000 PRINT 70, DELAY, PERIOD, A
04100 70 FORMAT(' DELAY = ',F7.3/' PERIOD = ', F8.3/' A= ',F6.4)
04200 TYPE 80, XAPP
04300 PRINT 80, XAPP
04400 80 FORMAT(' XAPP = ',G)
04500 TAUMAX = PERIOD/(2*XAPP)
04600 TYPE 90, TAUMAX
04700 PRINT 90, TAUMAX
04800 FORMAT(' TAUMAX = ',G)
04900 90 PHI=ATAN(XAPP/PI)*180/PI
05000 C CAP IS THE LOCK-IN OUTPUT FOR UNIT TRANSIENT
05100 IF(BN-2.0) 150,160,170
05200 150 THETA=-1.*PHI
05300 GO TO 200
05400 160 THETA=0.
05500 GO TO 200
05600 170 THETA=-360*A
05700 200 CAP=2/PI*EXP(-2*A*XAPP)*(EXP(-2*XAPP)-1.)/(XAPP**2+PI**2)
05800 **0.5*COSD(THETA+PHI)
05900 TYPE 100, THETA, PHI, CAP
06000 PRINT 100, THETA, PHI, CAP
06100 100 FORMAT(' THETA = ',G/' PHI = ',G/' CAP = ',G/)
06200 300 CONTINUE
06300 STOP
06400 END
06500

```

```

00100
00200      FUNCTION F(X)
00300      COMMON A,BN
00400      PI=3.14159
00500      IF(BN<2.0) 10,20,30
00600      10      F=EXP(-2*X)*((2*A+2)*(X**2+PI**2)+X)-2*A*(X**2+PI**2)-X
00700      GO TO 50
00800      20      F=EXP(-2*X)*((2*A+2)*(X**2+PI**2)+X)*COSD(180/
00900      C      (X**2+PI**2)**0.5)+PI*SIND(180/(X**2+PI**2)**0.5)
01000      C      -(2*A*(X**2+PI**2)+X)*COSD(180/(X**2+PI**2)**0.5)
01100      C      )-PI*SIND(180/(X**2+PI**2)**0.5)
01200      GO TO 50
01300      30      F=EXP(-2*X)*((2*A+2)*(X**2+PI**2)+X)*COS(ATAN(X/PI)-
01400      C      A**2*PI)+PI*SIN(ATAN(X/PI)-A**2*PI)-(2*A*(X**2+PI**2)+X)
01500      C      *COS(ATAN(X/PI)-A**2*PI)-PI*SIN(ATAN(X/PI)-A**2*PI)
01600      RETURN
01700      END

```

APPENDIX B

Dual-channel Boxcar Averager Operation and
Numerical Computation Program for the DLTS System

B.1 Dual-channel Boxcar Averager Operation

In a DLTS system employing a dual channel boxcar averager, transient signals are fed into the integrators with sampling instants at t_1 and t_2 . For a finite gate width w the output for each channel is

$$S_1(\tau) = \frac{1}{w} \int_{t_1}^{t_1+w} e^{-t/\tau} dt$$

$$S_2(\tau) = \frac{1}{w} \int_{t_2}^{t_2+w} e^{-t/\tau} dt$$

The output signal is

$$\begin{aligned} S(\tau) &= S_1(\tau) - S_2(\tau) \\ &= \frac{\tau}{w} (1 - e^{-w/\tau}) (e^{-t_1/\tau} - e^{-t_2/\tau}) \end{aligned} \quad (B.1)$$

Hence the DLTS peak will occur at τ_{\max} where $\frac{dS(\tau)}{d\tau} \Big|_{\tau_{\max}} = 0$. Therefore τ_{\max} is the numerical solution to

$$\begin{aligned} e^{-(t_1-t_2)/\tau} [1 + (t_1/\tau) - e^{-w/\tau} (1 + w/\tau + t_1/\tau)] \\ - [1 + (t_2/\tau) - e^{-w/\tau} (1 + w/\tau + t_2/\tau)] = 0 \end{aligned} \quad (B.2)$$

The numerical computation program is given in Section B.3.

B.2 Obtaining ΔC from the Boxcar Peak Height

The PAR 164 integrator has a sensitivity of 100mV for a full scale output of 10 volts. If the capacitance transient is $\Delta C e^{-t/\tau}$, then the DLTS peak V_L (volts) should be

$$\frac{V_L}{10} \times 0.1 = \frac{\Delta C}{S_B} \times S(\tau_{\max})$$

where S_B is the conversion factor of the capacitance bridge. ΔC can be calculated from

$$\Delta C = 0.01 \times V_L \times S_B / S(\tau_{\max})$$

For a simplified case where $w = 0$,

$$\tau_{\max} = (t_2 - t_1) / \ln(t_2/t_1)$$

and $S(\tau_{\max})$ can be calculated from equation (B.1).

B.3 Numerical Computation Program

```

00100  C  TO EXECUTE THIS PROGRAM YOU HAVE TO TYPE EX DLTSBO.FOR,SYS:
00200  C  BOXCAR
00300  C  IMSL/SEAR
00400  C  THIS PROGRAM IS TO CALCULATE OPTIMUM TIME CONSTANT, BOXCAR DLTS
00500  C  PEAK FOR FINITE GATE WIDTH
00600  C  EXTERNAL F
00700  C  COMMON A,W,T1,T2,XL,XR,EPS,NSIG,XAPP,ITMAX,IER
00800  C  WRITE(5,30)
00900  30  FORMAT(1$'ENTER THE RATIO A = T2/T1 ',,$)
01000  C  READ(5,40) A
01100  40  FORMAT(5)
01200  C  ITMAX=100000
01300  C  EPS=.001
01400  C  NSIG=4
01500  C  DO 200 I=1,10
01600  C  P=0.1*I
01700  C  TYPE 50, P
01800  C  PRINT 50, P
01900  50  C  FORMAT(' TAU1 NEGLECTS PULSE WIDTH, TAU2 ASSUMES MIDPOINT,
02000  C  TAUUMAX IS TRUE VALUE, GATE WIDTH PERCENT = ',G)
02100  C  THE FOLLOWING CALCULATION ASSUME T1 FROM 0.1 TO 50 (ANY UNIT)
02200  C  DO 150 J=1,500
02300  C  TC IS TO CHECK T1 AND T2 ARE WITHIN THE RANGES
02400  C  T1=0.1*J
02500  C  W=P*(A-1)*T1
02600  C  T2=A*T1
02700  C  TAU1=(T2-T1)/ ALOG(T2/T1)
02800  C  TAU2=(T2-T1)/ ALOG((T2+W/2.)/(T1+W/2.))
02900  C  X1=1./TAU1
03000  C  X2=1./TAU2
03100  C  TYPE 60, X1, X2
03200  60  C  FORMAT(' XL SHOULD BE LESS THAN X2, XR GREATER THAN X1 ',
03300  C  ' X1 = ',G,' X2 = ',G)
03400  C  XL=X2/1.05
03500  C  XR=X1*1.05
03600  C  TYPE 70, XL, XR
03700  70  C  FORMAT(' XL = ',G,' XR = ',G)
03800  C  TC=(50-W)/A
03900  C  IF(T1.GT.TC) GO TO 200
04000  C  CALL ZFALSE(F,EPS,NSIG,XL,XR,XAPP,ITMAX,IER)
04100  C  TYPE 80,XAPP
04200  C  PRINT 80, XAPP
04300  80  C  FORMAT(' XAPPP = ',G)
04400  C  TYPE 90, IER
04500  90  C  FORMAT(' IER = ',G)
04600  C  TAUUMAX=1./XAPP
04700  C  TYPE 100, T1, TAUUMAX, TAU1, TAU2
04800  C  PRINT 100, T1, TAUUMAX, TAU1, TAU2
04900  100  C  FORMAT(' T1 = ',F8.4,3X,' TAUUMAX = ', F7.3,33X,' TAU1 = ',F7.3,
05000  C  3X,' TAU2 = ',F7.3/)
05100  C  CONTINUE
05200  150  C  CONTINUE
05300  C  END
05400  C  FUNCTION F(X)
05500  C  COMMON A,W,T1
05600  C  F=EXP((A-1)*T1*X)*(1+T1*X-EXP(-W*X)*(1+W*X+T1*X))-((1+A*T1*
05700  C  X)-EXP(-W*X)*(1+W*X+A*T1*X))
05800  C  RETURN
05900  C  END

```

APPENDIX C

Computer Programs for Calculating Thermal Activation Energies and Capture Cross Sections for DLTS Systems Using Either the Lock-in Amplifier or the Boxcar Averager.

```

00100  C      TO EXECUTE THIS PROGRAM---TYPE 'LSFLOC'
00200  C      THIS PROGRAM USES THE ORTHOGONAL POLYNOMIAL TO LEAST SQUARE
00300  C      FIT THE DATA ON THE ARRHENIUS PLOT AND CALCULATE THE ENERGY
00400  C      LEVEL AS WELL AS THE CAPTURE CROSS SECTION
00500  C      COMMON/POLY/NTERMS,B(10),C(10),D(10)
00600  C      DIMENSION X(10),F(10),W(10),ERROR(10),PJM1(10),PJ(10)
00700  C      DIMENSION T(10),FREQ(10),TAU(10),ASLOPE(10)
00800  C      REAL A(80)
00900  C      WRITE(5,50)
01000  50      FORMAT(1X,ENTER ONE LINE COMMENT  ',,$)
01100  C      READ(5,60) A
01200  60      FORMAT(80A1)
01300  C      PRINT 70
01400  70      FORMAT(1X,*****)
01500  C      PRINT 80,A
01600  80      FORMAT(1X,80A1)
01700  C      WRITE(5,100)
01800  100     FORMAT(1X,NPOINT= NUMBER OF THE DATA POINTS =',,$)
01900  C      READ(5,200) NPOINT
02000  200     FORMAT(G)
02100  C      DO 1 I=1,NPOINT
02200  C      W(I)=1.
02300  C      WRITE(5,300) I
02400  300     FORMAT(1X,T('I1,')= TEMPERATURE      ',,$)
02500  C      READ(5,200) T(I)
02600  C      X(I)=1./T(I)
02700  C      WRITE(5,500) I
02800  500     FORMAT(1X,FREQ('I1,')= FREQUENCY OF LOCK-IN  ',,$)
02900  C      READ(5,200) FREQ(I)
03000  C      TAU(I)=.424/FREQ(I)
03100  C      TTTAU=T(I)**2*TAU(I)
03200  C      XX=1000*X(I)
03300  C      PRINT 250,FREQ(I),T(I),TTTAU,XX
03400  250     FORMAT(1X,FREQ='F6.1,1HZ ','TEMP='F8.2,'K',' T**2*TAU='
03500  C      F10.4,'T**2*SEC ','1000/T ='F8.4)
03600  1       C      F(I)=8.625E-5*ALOG(T(I)**2*TAU(I))
03700  C      WRITE(5,530)
03800  530     FORMAT(1X,THE EFFECTIVE MASS OF ELECTRON AND HOLE IN SILICON
03900  C      ARE 1.968, .5587 ; IN GAAS ARE .068, .5 '/')
04000  C      WRITE(5,550)
04100  550     FORMAT(1X,EFFECTIVE MASS = ',,$)
04200  C      READ(5,200)EFFMAS
04300  C      NTERMS=2
04400  C      CALL ORTPOL(NPOINT, X,F,W,ERROR,PJM1,PJ)
04500  C      TYPE 601,(J,B(J),C(J),D(J),J=1,NTERMS)
04600  601     C      FORMAT('J='I1,'B(J)='E16.8,' C
04700  C      (J)='E16.8,' D(J)='E16.8/ )
04800  C      TYPE 751
04900  751     C      FORMAT(' EMISIN(I) IS THE EMISSION PROPORTIONAL
05000  C      CONSTANT WHICH SHOULD BE CONST ',/)
05100  C      PRINT 751
05200  C      DO 2 I=1,NPOINT
05300  C      ASLOPE(I)=(F(I)+D(2)*B(1)-D(1))*T(I)
05400  C      TYPE 801,I,ASLOPE(I)
05500  801     C      FORMAT(' ASLOPE('I1') = ',E16.8)
05600  C      PRINT 801,I,ASLOPE(I)
05700  2       C      CONTINUE
05800  C      CONST=EXP((D(2)*B(1)-D(1))/8.625E-5)
05900  C      TYPE 701,CONST
06000  C      PRINT 701,CONST
06100  701     C      FORMAT(' CONSTANT=(3K/M**).5* NC*SIGMA='E16.8)
06200  C      SIGMA=CONST*3.071986E-22/EFFMAS
06300  C      TYPE 901,SIGMA
06400  C      PRINT 901,SIGMA
06500  901     C      FORMAT(' CAPTURE CROSS SECTION = ',E16.8/)
06600  C      TYPE 951,D(2)
06700  951     C      FORMAT(' THERMAL EMISSION ENERGY = ',E16.8/)
06800  C      PRINT 951,D(2)
06900  C      END
07000

```

```

00100
00200
00300
00400
00500
00600
00700
00800
00900      9
01000
01100
01200
01300
01400      10
01500
01600
01700      11
01800
01900
02000
02100
02200      12
02300
02400      20
02500
02600
02700
02800
02900
03000      21
03100
03200
03300      22
03400
03500
03600
03700
03800
03900
04000      27
04100
04200

SUBROUTINE ORTPOL(NPOINT,X,F,W,ERROR,PJM1,PJ)U
COMMON/POLY/INTERMS,B(10),C(10),D(10)
DIMENSION X(10),W(10),F(10),ERROR(10),PJM1(10),PJ(10)U
DIMENSION S(10),T(10),FREQ(10),TAU(10)
DO 9 J=1,INTERMS
  B(J)=0.
  D(J)=0.
  S(J)=0.
  C(1)=0.
  DO 10 I=1,NPOINT
    D(1)=D(1)+F(I)*W(I)
    B(1)=B(1)+X(I)*W(I)
    S(1)=S(1)+W(I)
    D(1)=D(1)/S(1)
    DO 11 I=1,NPOINT
      ERROR(I)=F(I)-D(1)
      IF(INTERMS .EQ. 1)      RETURN
      B(1)=B(1)/S(1)
      DO 12 I=1,NPOINT
        PJM1(I)=1.
        PJ(I)=X(I)-D(1)
        J=1
        J=J+1
        DO 21 I=1,NPOINT
          P=PJ(I)*W(I)
          D(J)=D(J)+ERROR(I)*P
          P=P*PJ(I)
          B(J)=B(J)+X(I)*P
          S(J)=S(J)+P
          D(J)=D(J)/S(J)
        DO 22 I=1,NPOINT
          ERROR(I)=ERROR(I)-D(J)*PJ(I)
          IF(J .EQ. INTERMS) RETURN
          B(J)=B(J)/S(J)
          C(J)=S(J)/S(J-1)
          DO 27 I=1,NPOINT
            P=PJ(I)
            PJ(I)=(X(I)-B(J))*PJ(I)-C(J)*PJM1(I)
            PJM1(I)=P
            GO TO 20
          END

```

```

00100  C      TO EXECUTE THIS PROGRAM---TYPE 'LSFBOX'
00200  C      THIS PROGRAM USES THE ORTHOGONAL POLYNOMIAL TO LEAST SQUARE
00300          FIT THE DATA ON THE ARRHENIUS PLOT AND CALCULATE THE ENERGY
00400          LEVEL AS WELL AS THE CAPTURE CROSS SECTION
00500          DIMENSION X(10),F(10),T(10),TAU(10),ASLOPE(10)
00600          REAL A(80)
00700          WRITE(5,50)
00800  50      FORMAT(1, ENTER ONE LINE COMMENT ',,$)
00900          READ(5,60)A
01000  60      FORMAT(80A1)
01100          PRINT 1150
01200  1150     FORMAT(' ****')
01300          PRINT 1200,A
01400  1200     FORMAT(1X,80A1)
01500          WRITE(5,1300)
01600  1300     FORMAT(1, ENTER PULSE WIDTH IN usec = ',,$)
01700          READ(5,1400) PD
01800  1400     FORMAT(G)
01900          PRINT 1500,PD
02000  1500     FORMAT(1, PULSE WIDTH = ',F8.3,' usec')
02100          WRITE(5,100)
02200  100      FORMAT(1, NPOINT= NUMBER OF THE DATA POINTS =',,$)
02300          READ(5,200) NPOINT
02400  200      FORMAT(G)
02500          DO 1 I=1,NPOINT
02600          WRITE(5,300) I
02700  300      FORMAT(1, T(' ,I1,' ) = TEMPERATURE      ',,$)
02800          READ(5,400)T(I)
02900  400      FORMAT(G)
03000          X(I)=1./T(I)
03100          WRITE(5,500)
03200  500      FORMAT(1, ENTER THE FIRST SAMPLING INSTANT IN msec ',,$)
03300          READ(5,600)T1
03400  600      FORMAT(G)
03500          WRITE(5,1000)
03600  1000     FORMAT(1, ENTER THE SECOND SAMPLING INSTANT IN msec ',,$)
03700          READ(5,600)T2
03800          WRITE(5,510)
03900  510      FORMAT(1, ENTER THE APERTURE DURATION IN usec ',,$)
04000          READ(5,520) AD
04100  520      FORMAT(G)
04200          T11=T1
04300          T22=T2
04400          T1=T1-.001*PD+.0005*AD
04500          T2=T2-.001*PD+.0005*AD
04600          TAU(I)=.001*(T2-T1)/ ALOG(T2/T1)
04700          TTTAU=T(I)**2*TAU(I)
04800          AX=1000*X(I)
04900          RATIO=EXP(-.001*T1/TAU(I))-EXP(-.001*T2/TAU(I))
05000          PRINT 1100,T11,T22,AD,T(I),TTTAU,AX
05100  1100     C      FORMAT(1, T1= ',F6.3 ' T2= ',F6.3 ' MSEC ', ' AD= ',F8.3-
05200          ' USEC ', ' TEMP= ',F8.3 ', K', ' T**2*TAU= ',F10.3, ' T**2-
05300          SEC ', ' 1000/T = ',F8.4)
05400          PRINT 1250, RATIO
05500  1250     C      FORMAT(1, AMPLITUDE RATIO= EXP(-T1/TAU)-EXP(-T2/TAU)= ',F7.5)
05600          F(I)=8.625E-5*ALOG(T(I)**2*TAU(I))
05700          WRITE(5,530)
05800  530      C      FORMAT(1, THE EFFECTIVE MASS OF ELECTRON AND HOLE IN SILICON
05900          ARE 1.963, .55587 ; IN GAAS ARE .068, .5'')
06000          WRITE(5,550)
06100  550      C      FORMAT(1, EFFECTIVE MASS = ',,$)
06200          READ(5,560) EMMAS
06300  560      C      FORMAT(G)
06400          CALL LISQUA(NPOINT,X,F,SLOPE,GONST)
06500          TYPE 751
06600  751      C      FORMAT(1, EMISIN(I) IS THE EMISSION PROPORTIONAL
06700          CONSTANT WHICH SHOULD BE CONST ',/)
06800          PRINT 751
06900          DO 2 I=1,NPOINT
07000          ASLOPE(I)=(F(I)-GONST)*X(I)
07100

```

```

00100
00200
00300 801      TYPE 801,I,ASLOPE(I)
00400
00500 2        FORMAT(' ASLOPE('I1,') = ',E16.8)
00600
00700
00800 701      PRINT 801,I,ASLOPE(I)
00900
01000
01100
01200
01300
01400
01500 901      CONTINUE
01600
01700
01800
01900
02000
02100
02200
02300
02400
02500
02600
02700
02800
02900 10       951      CONST=EXP(-GONST/8.625E-5)
03000
03100
03200
03300
03400
          701      FORMAT(' CONSTANT=(3K/M**.5* NC*SIGMA= ',E16.8)
          PRINT 701,CONST
          SIGMA=CONST*3.071986E-22/EFFMAS
          TYPE 901,SIGMA
          901      FORMAT(' CAPTURE CROSS SECTION = ',E16.8/)
          PRINT 901,SIGMA
          TYPE 951,SLOPE
          951      FORMAT(' THERMAL EMISSION ENERGY = ',E16.8/)
          PRINT 951,SLOPE
          END
          SUBROUTINE LISQUA(NPOINT,X,F,SLOPE,GONST)
          DIMENSION X(10),F(10)
          XBAR=0.
          YBAR=0.
          PRODUC=0.
          SQUARE=0.
          DO 10 I=1,NPOINT
          XBAR=XBAR+X(I)
          YBAR=YBAR+F(I)
          PRODUC=PRODUC+X(I)**F(I)
          SQUARE=SQUARE+X(I)**2
          CONTINUE
          XBAR=XBAR/NPOINT
          YBAR=YBAR/NPOINT
          SLOPE=(PRODUC-NPOINT*XBAR*YBAR)/(SQUARE-NPOINT*XBAR**2)
          GONST=YBAR-SLOPE*XBAR
          END

```

APPENDIX D

Projected Range Statistics of Implanted
B, Be, Ga, O, and N in GaAs, Obtained from LSS Theory

1 LSS RANGE STATISTICS FOR BERYLLIUM

IN GALLIUM ARSENIDE		ENERGY (KEV) 10	PROJECTED RANGE (MICRONS) 0.0308	PROJECTED STANDARD DEVIATION (MICRONS) 0.0103	RANGE (MICRONS) 0.1069	STANDARD DEVIATION (MICRONS) 0.0178	NUCLEAR ENERGY LOSS (KEV/MICRON) 0.59248+02	ELECTRONIC ENERGY LOSS (KEV/MICRON) 0.64532+02
+ SUBSTRATE PARAMETERS-								
+ GALLIUM ARSENIDE		20	0.0615	0.0410	0.1821	0.0267	0.50356+02	0.91252+02
+ 2 31 33		30	0.0916	0.0555	0.2492	0.0331	0.43336+02	0.11182+03
+ 69.720 74.920		40	0.1262	0.0676	0.3108	0.0380	0.39316+02	0.12918+03
+ 0.22148+23 .22148+23		50	0.1590	0.0788	0.3683	0.0419	0.35488+02	0.14438+03
+ RHO/R .4991E-01 .4561E+01		60	0.1917	0.0885	0.4223	0.0450	0.32675+02	0.15818+03
+ EPS/E .66038E-01 .61199E-01		70	0.2210	0.0971	0.4733	0.0476	0.29918+02	0.17072+03
+ CHSE .10148+02 .10271E+02		80	0.2564	0.1051	0.5268	0.0498	0.27297E+02	0.18251E+03
+ MU 7.747 8.324		90	0.2887	0.1123	0.5688	0.0517	0.24998E+02	0.19363E+03
+ 180 0.4452 0.4747		100	0.3209	0.1188	0.6136	0.0534	0.23098E+02	0.20418E+03
+ 150 0.4747 0.4844		110	0.3528	0.1248	0.6589	0.0549	0.21545E+02	0.21403E+03
+ 120 0.3842 0.4151		130	0.4151	0.1303	0.6986	0.0563	0.20371E+02	0.22351E+03
+ 140 0.4452 0.4747		150	0.4452	0.1400	0.7739	0.0575	0.19575E+02	0.23271E+03
+ 160 0.5026 0.5305		170	0.5305	0.1525	0.8879	0.0612	0.17908E+02	0.26618E+03
+ 180 0.5682 0.5972		190	0.5682	0.1662	0.9267	0.0619	0.17026E+02	0.27738E+03
+ 200 0.6128 0.6128		220	0.6662	0.1630	0.9900	0.0633	0.16205E+02	0.28138E+03
+ GAMMA .4050 .3830		230	0.7185	0.1745	1.0541	0.0644	0.15468E+02	0.29862E+03
+ 280 0.8191 0.8191		260	0.7695	0.1794	1.1759	0.0664	0.12571E+02	0.34908E+03
+ 300 0.8613 0.8613		320	0.9132	0.1919	1.2334	0.0679	0.12196E+02	0.30278E+03
+ 340 0.9596 0.9596		360	1.0041	0.1988	1.4462	0.0692	0.11312E+02	0.36508E+03
+ 460 1.2180 1.2180		500	1.0486	0.2019	1.4958	0.0697	0.10718E+02	0.38722E+03
+ 480 1.2587 1.2587		550	1.2987	0.2164	1.7275	0.0702	0.10158E+02	0.39782E+03
+ 550 1.3961 0.2220		600	1.3961	0.2220	1.7711	0.0726	0.18728E+01	0.46638E+03
+ 600 1.4896 0.2221		440	1.1767	0.2099	1.6379	0.0715	0.87888E+01	0.42808E+03
+ 650 1.5729 0.2229		460	1.2180	0.2122	1.6832	0.0719	0.84328E+01	0.43763E+03
+ 700 1.6666 0.2222		500	1.2587	0.2143	1.7275	0.0722	0.81275E+01	0.44718E+03
+ 750 1.7511 0.2352		550	1.2987	0.2164	1.7711	0.0733	0.78728E+01	0.45638E+03
+ 800 1.8332 0.2380		600	1.3961	0.2220	1.8763	0.0740	0.74528E+01	0.48858E+03
+ 850 1.9132 0.2408		440	1.0920	0.2047	1.5442	0.0707	0.96188E+01	0.40918E+03
+ 900 1.9911 0.2439		460	1.1347	0.2074	1.5916	0.0711	0.91938E+01	0.41828E+03
+ 950 2.0672 0.2469		500	1.1896	0.2221	1.9770	0.0740	0.11376E+02	0.51650E+03
+ 1000 2.1116 0.2480		440	1.1767	0.2099	1.6379	0.0715	0.87888E+01	0.42808E+03
+ CROSS SECTION SUB. E = 4.00		650	1.5729	0.2289	2.0737	0.0745	0.71968E+01	0.50928E+03
+ ELECTRONIC CROSS SECTIONS OF		700	1.6666	0.2322	2.1668	0.0750	0.68128E+01	0.53998E+03
+ LINDHARD, SCHAFF, SCHIOTT		750	1.7511	0.2352	2.2567	0.0755	0.616668E+01	0.55888E+03
+ 800 1.8332 0.2380		800	1.8332	0.2380	2.3438	0.0759	0.61575E+01	0.57718E+03
+ 850 1.9132 0.2408		850	1.9132	0.2380	2.4262	0.0766	0.58792E+01	0.59492E+03
+ 900 1.9911 0.2439		900	1.9911	0.2408	2.5031	0.0769	0.56227E+01	0.61222E+03
+ 950 2.0672 0.2469		950	2.0672	0.2439	2.5901	0.0772	0.53973E+01	0.63098E+03
+ 1000 2.1116 0.2480		1000	2.1116	0.2480	2.6880	0.0772	0.516883E+01	0.64532E+03

1 LSS RANGE STATISTICS FOR BORON
IN GALLIUM ARSENIDE

	SUBSTRATE PARAMETERS-		PROJECTED RANGE (KEV)	PROJECTED STANDARD DEVIATION (MICRONS)	RANGE (MICRONS)	STANDARD DEVIATION (MICRONS)	NUCLEAR ENERGY LOSS (KEV/MICRON)	ELECTRONIC ENERGY LOSS (KEV/MICRON)
+	GALLIUM ARSENIDE		20 0.0468	0.0334	0.1396	0.0242	0.786E+02	0.102E+03
+		30 0.0542	0.0446	0.1926	0.0308	0.709E+02	0.125E+03	
+		40 0.0698	0.0548	0.2420	0.0361	0.644E+02	0.144E+03	
+		50 0.1256	0.0643	0.2885	0.0404	0.588E+02	0.161E+03	
+		60 0.1517	0.0730	0.3329	0.0441	0.541E+02	0.176E+03	
+		70 0.1777	0.0808	0.3752	0.0472	0.503E+02	0.191E+03	
+		80 0.2035	0.0880	0.4158	0.0499	0.476E+02	0.204E+03	
+		90 0.2290	0.0947	0.4548	0.0522	0.442E+02	0.216E+03	
+	RHO/R	.5159E+01	100 0.2546	0.1009	0.4925	0.0542	0.418E+02	0.228E+03
+		110 0.2802	0.1067	0.5390	0.0561	0.384E+02	0.239E+03	
+	EPS/E	.50669E-01	120 0.3057	0.1121	0.5644	0.0578	0.3601E+02	0.250E+03
+		130 0.3311	0.1171	0.5989	0.0593	0.3390E+02	0.260E+03	
+	CMSB	.1134E+02	140 0.3563	0.1218	0.6324	0.0608	0.3211E+02	0.270E+03
+		150 0.3812	0.1262	0.6851	0.0621	0.3066E+02	0.279E+03	
+	HU	6.338 6.811	160 0.4058	0.1303	0.6969	0.0632	0.2949E+02	0.288E+03
+		170 0.4301	0.1342	0.7279	0.0643	0.2866E+02	0.297E+03	
+	GAMMA	.4708 .4465	180 0.4626	0.1378	0.7582	0.0653	0.2852E+02	0.306E+03
+		190 0.4771	0.1413	0.7877	0.0663	0.2798E+02	0.314E+03	
+		200 0.4997	0.1445	0.8165	0.0671	0.2803E+02	0.323E+03	
+	SNO	.7177E+02	220 0.5839	0.1507	0.8723	0.0686	0.2610E+02	0.338E+03
+		240 0.6303	0.1616	0.9781	0.0712	0.2271E+02	0.368E+03	
+	ION-BORON		260 0.6726	0.1664	1.0285	0.0723	0.2125E+02	0.382E+03
+		280 0.7141	0.1707	1.0773	0.0733	0.2008E+02	0.408E+03	
+		320 0.7548	0.1748	1.1248	0.0742	0.1909E+02	0.421E+03	
+		340 0.7947	0.1785	1.1709	0.0750	0.1839E+02	0.421E+03	
+		360 0.8338	0.1820	1.2158	0.0758	0.1775E+02	0.433E+03	
+		380 0.8720	0.1853	1.2596	0.0765	0.1717E+02	0.445E+03	
+		400 0.9093	0.1884	1.3022	0.0771	0.1621E+02	0.456E+03	
+	H	11.0000	440 0.9816	0.1941	1.3846	0.0783	0.1669E+02	0.479E+03
+		460 1.0171	0.1967	1.4246	0.0788	0.1503E+02	0.499E+03	
+		480 1.0520	0.1992	1.4637	0.0793	0.1424E+02	0.515E+03	
+		500 1.0865	0.2015	1.5021	0.0802	0.1345E+02	0.535E+03	
+		550 1.1709	0.2058	1.5922	0.0806	0.1266E+02	0.555E+03	
+		600 1.2526	0.2115	1.6844	0.0817	0.1235E+02	0.559E+03	
+	CROSS SECTION SUB. E = 6.00		650 1.3318	0.2156	1.7702	0.0825	0.1156E+02	0.582E+03
+		700 1.4086	0.2193	1.8530	0.0832	0.1104E+02	0.604E+03	
+	ELECTRONIC CROSS SECTIONS OF LINDHARD, SCHARPF, SCHIOTTI		750 1.4830	0.2226	1.9329	0.0838	0.1080E+02	0.625E+03
+		800 1.5553	0.2257	2.0102	0.0844	0.1074E+02	0.645E+03	
+		850 1.6254	0.2287	2.0852	0.0849	0.1053E+02	0.665E+03	
+		900 1.6939	0.2317	2.1581	0.0854	0.1032E+02	0.685E+03	
+		950 1.7627	0.2346	2.2291	0.0858	0.997E+01	0.703E+03	
+		1000 1.8261	0.2358	2.2983	0.0862	0.931E+01	0.722E+03	

1 LOSS RANGE STATISTICS FOR NITROGEN

IN GALLIUM

ARSENIDE

			PROJECTED RANGE (MICRONS)	PROJECTED STANDARD DEVIATION (MICRONS)	RANGE (MICRONS)	STANDARD DEVIATION (MICRONS)	NUCLEAR LOSS (KEV/MICRON)	ELECTRONIC LOSS (KEV/MICRON)
+	SUBSTRATE PARAMETERS-							
+	GALLIUM ARSENIDE							
+	Z 31 33		0.0354	0.0240	0.0952	0.0197	0.1450E+03	0.8728E+02
+	M 69.720 74.920		0.0324	0.0320	0.1313	0.0256	0.1314E+03	0.1512E+03
+	N .2214E-23 .2214E+23		0.0682	0.0682	0.1658	0.0307	0.1234E+03	0.1746E+03
+	RHO/R .6286E+01 .5809E+01		0.0682	0.0682	0.1987	0.0351	0.1147E+03	0.1952E+03
+	EPS/E .3395E-01 .3179E-01		0.1062	0.0903	0.2204	0.0389	0.1071E+03	0.2139E+03
+	CHSE .1369E+02 .1392E+02		0.1243	0.0593	0.2610	0.0423	0.1012E+03	0.2309E+03
+	HU 4.980 5.351		0.1424	0.0656	0.2907	0.0453	0.9523E+02	0.2469E+02
+	SNO .1201E+03		0.1606	0.0711	0.3195	0.0481	0.2618E+02	0.2816E+02
+	Z 7		0.1788	0.0764	0.3747	0.0505	0.9599E+02	0.2760E+02
+	M 14.000		0.1968	0.0813	0.3747	0.0528	0.8221E+02	0.2895E+02
+	CROSS SECTION SUB. E= 7.00		0.2147	0.0859	0.4013	0.0547	0.7912E+02	0.3024E+02
+	ELECTRONIC CROSS SECTIONS OF LINDHARD, SCHAFER, SCHIOTT		0.2324	0.0903	0.4272	0.0566	0.7553E+02	0.3147E+02
+			0.2502	0.0985	0.4726	0.0582	0.7198E+02	0.3266E+02
+			0.2679	0.0985	0.4774	0.0598	0.6861E+02	0.3380E+02
+			0.2856	0.1023	0.5017	0.0613	0.6519E+02	0.3492E+02
+			0.3033	0.1083	0.5256	0.0627	0.6261E+02	0.3599E+02
+			0.3209	0.1095	0.5421	0.0640	0.5971E+02	0.3803E+02
+			0.3284	0.1129	0.5521	0.0653	0.5541E+02	0.3903E+02
+			0.3559	0.1163	0.5958	0.0663	0.5151E+02	0.4276E+02
+			0.3735	0.1226	0.6189	0.0680	0.4911E+02	0.4092E+02
+			0.3743	0.1226	0.6195	0.0685	0.4918E+02	0.4095E+02
+			0.3775	0.1336	0.6228	0.0722	0.4750E+02	0.4451E+02
+			0.3898	0.1372	0.7627	0.0731	0.4679E+02	0.4619E+02
+			0.5210	0.1526	0.8614	0.0731	0.4167E+02	0.4768E+02
+			0.5215	0.1526	0.8615	0.0731	0.4154E+02	0.4763E+02
+			0.5216	0.1456	0.8790	0.0773	0.4230E+02	0.5083E+02
+			0.5217	0.1455	0.8757	0.0774	0.4230E+02	0.5083E+02
+	ION-NITROGEN		0.6114	0.1531	0.9115	0.0785	0.4065E+02	0.5237E+02
+	Z 7		0.6109	0.1535	0.9465	0.0794	0.3808E+02	0.4619E+02
+	M 14.000		0.6701	0.1598	0.9909	0.0804	0.3693E+02	0.5520E+02
+			0.6989	0.1628	1.0145	0.0812	0.3536E+02	0.5651E+02
+			0.7274	0.1657	1.0474	0.0820	0.3339E+02	0.5779E+02
+			0.7274	0.1657	1.0798	0.0828	0.3220E+02	0.5924E+02
+			0.7553	0.1655	1.1115	0.0835	0.3161E+02	0.6047E+02
+			0.8106	0.1716	1.1426	0.0842	0.3008E+02	0.6178E+02
+			0.8106	0.1716	1.1733	0.0852	0.2944E+02	0.6317E+02
+			0.8773	0.1733	1.2181	0.0857	0.2805E+02	0.6478E+02
+			0.9114	0.1814	1.2904	0.0870	0.3030E+02	0.6761E+02
+			1.0033	0.1811	1.3599	0.0882	0.2877E+02	0.7031E+02
+			1.0637	0.1924	1.4271	0.0892	0.2644E+02	0.7303E+02
+			1.1227	0.1972	1.4922	0.0901	0.2451E+02	0.7559E+02
+			1.1805	0.2007	1.5553	0.0910	0.2229E+02	0.7801E+02
+			1.2973	0.2059	1.6163	0.0924	0.2055E+02	0.8280E+02
+			1.3464	0.2097	1.7345	0.0931	0.1963E+02	0.8505E+02
+			1.3994	0.2122	1.7913	0.0937	0.1892E+02	0.8729E+02

LSS RANGE STATISTICS FOR OXYGEN IN CALCIUM ARSENIDE

LSS RANGER STATISTICS FOR OXYGEN IN GALLIUM ARSENIDE									
SUBSTRATE PARAMETERS-									
PROJECTED ENERGY	PROJECTED RANGE	NUCLEAR ENERGY	STANDARD DEVIATION	NUCLEAR ENERGY	STANDARD DEVIATION	NUCLEAR ENERGY	STANDARD DEVIATION	NUCLEAR ENERGY	STANDARD DEVIATION
(KEV)	(MICRONS)	(KEY/MICRON)	(MICRONS)	(KEY/MICRON)	(MICRONS)	(KEY/MICRON)	(MICRONS)	(KEY/MICRON)	(MICRONS)
GALLIUM ARSENIDE									
2 31 33	20 30 40 50	0.0169 0.0315 0.0614 0.0770	0.0210 0.0277 0.0345 0.0409	0.0807 0.1113 0.1468 0.1632	0.0138 0.0238 0.0288 0.0333	0.189E+03 0.1753E+03 0.161E+03 0.1523E+03	0.0113 0.0113 0.0113 0.0113	0.1301E+03 0.1593E+03 0.1839E+03 0.2056E+03	0.9/19E+02 0.9/19E+02 0.9/19E+02 0.9/19E+02
H H	69.720 74.920	0.0169	0.0169	0.0169	0.0169	0.0169	0.0169	0.0169	0.0169
N N	.2214E+23 .2214E+23	0.0169	0.0169	0.0169	0.0169	0.0169	0.0169	0.0169	0.0169
RHO/R	.6684E+01 .6197E+01	0.0169	0.0169	0.0169	0.0169	0.0169	0.0169	0.0169	0.0169
EPS/E	.2865E+01 .2667E+01	0.0169	0.0169	0.0169	0.0169	0.0169	0.0169	0.0169	0.0169
CNS/E	.1441E+02 .1867E+02	0.0169	0.0169	0.0169	0.0169	0.0169	0.0169	0.0169	0.0169
MU	4.358 4.683	0.0169	0.0169	0.0169	0.0169	0.0169	0.0169	0.0169	0.0169
GAMMA	.6073 .5800	0.0169	0.0169	0.0169	0.0169	0.0169	0.0169	0.0169	0.0169
SNR	.1514E+03	0.0169	0.0169	0.0169	0.0169	0.0169	0.0169	0.0169	0.0169
ION-OXYGEN									
2 8	220 240 260	0.3427 0.3732 0.4033	0.1121 0.1129 0.1129	0.5619 0.6099 0.6388	0.0700 0.0743 0.0743	0.738E+02 0.769E+02 0.801E+02	0.1314E+03 0.1505E+03 0.1689E+03	0.9/19E+02 0.9/19E+02 0.9/19E+02	0.9/19E+02 0.9/19E+02 0.9/19E+02
H H	16.000	0.3427	0.3732	0.4033	0.1121	0.5619	0.0700	0.738E+02	0.9/19E+02
CROSS SECTION SUB. E = 8.00									
ELECTRONIC CROSS SECTIONS OF									
LINDHARD, SCHARPF, SCHIOTT									
800 850 900 950 1000	1.0700 1.1200 1.1700 1.2200 1.2700	0.1942 0.1978 0.2014 0.2049 0.2085	1.4123 1.4738 1.5353 1.5968 1.6583	0.0975 0.0994 0.0993 0.0992 0.0991	0.2126E+02 0.2151E+02 0.2176E+02 0.2201E+02 0.2226E+02	0.8226E+02 0.8251E+02 0.8276E+02 0.8301E+02 0.8326E+02	0.9/19E+02 0.9/19E+02 0.9/19E+02 0.9/19E+02 0.9/19E+02	0.9/19E+02 0.9/19E+02 0.9/19E+02 0.9/19E+02 0.9/19E+02	0.9/19E+02 0.9/19E+02 0.9/19E+02 0.9/19E+02 0.9/19E+02

LSS RANGE STATISTICS FOR GALLIUM IN GALLIUM ARSENIDE

LSS RANGE STATISTICS FOR GALLIUM IN GALLIUM ARSENIDE									
SUBSTRATE PARAMETERS-		GALLIUM ARSENIDE		PROJECTED ENERGY (KEV) 10		PROJECTED STANDARD DEVIATION (MICRONS) 0.0031		STANDARD DEVIATION (MICRONS) 0.0107	
PROJECTED RANGE (MICRONS) 0.0070		NUCLEAR ENERGY LOSS (KEV/MICRON) 0.1244E-04		NUCLEAR ENERGY LOSS (KEV/MICRON) 0.1275E+03		NUCLEAR ENERGY LOSS (KEV/MICRON) 0.1275E+03		NUCLEAR ENERGY LOSS (KEV/MICRON) 0.1275E+03	
Z	31	33		20	0.0115	0.0049	0.0174	0.0061	0.1430E-04
				30	0.0156	0.0065	0.0233	0.0081	0.150E-04
				40	0.0195	0.0080	0.0288	0.0100	0.1600E-04
				50	0.0233	0.0095	0.0341	0.0117	0.1632E-04
				60	0.0270	0.0109	0.0393	0.0135	0.1672E-04
				70	0.0307	0.0122	0.0443	0.0152	0.1712E-04
				80	0.0344	0.0136	0.0493	0.0169	0.1750E-04
				90	0.0380	0.0149	0.0543	0.0185	0.1788E-04
				100	0.0417	0.0162	0.0592	0.0201	0.1819E-04
				110	0.0453	0.0174	0.0640	0.0217	0.1850E-04
RHO/R	.7733E+01	.7561E+01		120	0.0489	0.0186	0.0689	0.0233	0.1884E-04
EPS/E	.3830E-02	.3688E-02		130	0.0525	0.0198	0.0736	0.0248	0.1910E-04
CNSE	.1985E+02	.2048E+02		140	0.0561	0.0210	0.0784	0.0263	0.1944E-04
				150	0.0597	0.0222	0.0831	0.0278	0.1978E-04
				160	0.0632	0.0233	0.0878	0.0292	0.2010E-04
				170	0.0668	0.0243	0.0925	0.0307	0.2044E-04
				180	0.0704	0.0256	0.0972	0.0321	0.2078E-04
				190	0.0740	0.0267	0.1019	0.0335	0.2112E-04
				200	0.0776	0.0278	0.1065	0.0349	0.2146E-04
GMMA	1.0000	.9983		220	0.0848	0.0301	0.1159	0.0377	0.2181E-04
				240	0.0921	0.0323	0.1254	0.0414	0.2215E-04
				260	0.0995	0.0345	0.1347	0.0432	0.2249E-04
				280	0.1071	0.0368	0.1442	0.0460	0.2283E-04
				300	0.1146	0.0390	0.1536	0.0487	0.2317E-04
				320	0.1222	0.0411	0.1631	0.0513	0.2351E-04
				340	0.1298	0.0433	0.1726	0.0543	0.2385E-04
				360	0.1375	0.0454	0.1821	0.0566	0.1366E-04
				380	0.1451	0.0475	0.1916	0.0591	0.1352E-04
				400	0.1528	0.0495	0.2010	0.0617	0.1358E-04
				420	0.1605	0.0516	0.2105	0.0642	0.1358E-04
				440	0.1682	0.0536	0.2200	0.0666	0.1266E-04
				460	0.1760	0.0556	0.2294	0.0690	0.1208E-04
				480	0.1837	0.0576	0.2389	0.0714	0.1150E-04
				500	0.1915	0.0596	0.2484	0.0737	0.1125E-04
				520	0.1991	0.0616	0.2579	0.0761	0.1100E-04
				540	0.2067	0.0636	0.2674	0.0785	0.1075E-04
				560	0.2143	0.0656	0.2769	0.0809	0.1050E-04
				580	0.2203	0.0676	0.2864	0.0834	0.1025E-04
				600	0.2260	0.0696	0.2959	0.0859	0.1000E-04
				620	0.2317	0.0716	0.3054	0.0884	0.9750E-05
				640	0.2370	0.0736	0.3149	0.0909	0.9500E-05
				660	0.2420	0.0756	0.3244	0.0934	0.9250E-05
				680	0.2470	0.0776	0.3339	0.0959	0.9000E-05
				700	0.2510	0.0796	0.3434	0.0984	0.8750E-05
				720	0.2549	0.0816	0.3529	0.1009	0.8500E-05
				740	0.2587	0.0836	0.3624	0.1034	0.8250E-05
				760	0.2623	0.0856	0.3719	0.1059	0.8000E-05
				780	0.2657	0.0876	0.3814	0.1084	0.7750E-05
				800	0.2690	0.0896	0.3909	0.1109	0.7500E-05
				820	0.2720	0.0916	0.4004	0.1134	0.7250E-05
				840	0.2749	0.0936	0.4099	0.1159	0.7000E-05
				860	0.2777	0.0956	0.4194	0.1184	0.6750E-05
				880	0.2803	0.0976	0.4289	0.1209	0.6500E-05
				900	0.2820	0.0996	0.4384	0.1234	0.6250E-05
				920	0.2837	0.1016	0.4479	0.1259	0.6000E-05
				940	0.2853	0.1036	0.4574	0.1284	0.5750E-05
				960	0.2869	0.1056	0.4669	0.1309	0.5500E-05
				980	0.2883	0.1076	0.4764	0.1334	0.5250E-05
				1000	0.2897	0.1096	0.4859	0.1359	0.5000E-05
				1020	0.2910	0.1116	0.4954	0.1384	0.4750E-05
				1040	0.2923	0.1136	0.5049	0.1409	0.4500E-05
				1060	0.2936	0.1156	0.5144	0.1434	0.4250E-05
				1080	0.2948	0.1176	0.5239	0.1459	0.4000E-05
				1100	0.2960	0.1196	0.5334	0.1484	0.3750E-05
				1120	0.2971	0.1216	0.5429	0.1509	0.3500E-05
				1140	0.2983	0.1236	0.5524	0.1534	0.3250E-05
				1160	0.2994	0.1256	0.5619	0.1559	0.3000E-05
				1180	0.3005	0.1276	0.5714	0.1584	0.2750E-05
				1200	0.3016	0.1296	0.5809	0.1609	0.2500E-05
				1220	0.3027	0.1316	0.5904	0.1634	0.2250E-05
				1240	0.3038	0.1336	0.6099	0.1659	0.2000E-05
				1260	0.3049	0.1356	0.6194	0.1684	0.1750E-05
				1280	0.3060	0.1376	0.6289	0.1709	0.1500E-05
				1300	0.3070	0.1396	0.6384	0.1734	0.1250E-05
				1320	0.3081	0.1416	0.6479	0.1759	0.1000E-05
				1340	0.3091	0.1436	0.6574	0.1784	0.7500E-06
				1360	0.3102	0.1456	0.6669	0.1809	0.5000E-06
				1380	0.3112	0.1476	0.6764	0.1834	0.2500E-06
				1400	0.3123	0.1496	0.6859	0.1859	0.0000E+00
				1420	0.3133	0.1516	0.6954	0.1884	0.0000E+00
				1440	0.3143	0.1536	0.7049	0.1909	0.0000E+00
				1460	0.3153	0.1556	0.7144	0.1934	0.0000E+00
				1480	0.3163	0.1576	0.7239	0.1959	0.0000E+00
				1500	0.3173	0.1596	0.7334	0.1984	0.0000E+00
				1520	0.3183	0.1616	0.7429	0.2009	0.0000E+00
				1540	0.3193	0.1636	0.7524	0.2034	0.0000E+00
				1560	0.3203	0.1656	0.7619	0.2059	0.0000E+00
				1580	0.3213	0.1676	0.7714	0.2084	0.0000E+00
				1600	0.3223	0.1696	0.7809	0.2109	0.0000E+00
				1620	0.3233	0.1716	0.7904	0.2134	0.0000E+00
				1640	0.3243	0.1736	0.8099	0.2159	0.0000E+00
				1660	0.3253	0.1756	0.8194	0.2184	0.0000E+00
				1680	0.3263	0.1776	0.8289	0.2209	0.0000E+00
				1700	0.3273	0.1796	0.8384	0.2234	0.0000E+00
				1720	0.3283	0.1816	0.8479	0.2259	0.0000E+00
				1740	0.3293	0.1836	0.8574	0.2284	0.0000E+00
				1760	0.3303	0.1856	0.8669	0.2309	0.0000E+00
				1780	0.3313	0.1876	0.8764	0.2334	0.0000E+00
				1800	0.3323	0.1896	0.8859	0.2359	0.0000E+00
				1820	0.3333	0.1916	0.8954	0.2384	0.0000E+00
				1840	0.3343	0.1936	0.9049	0.2409	0.0000E+00
				1860	0.3353	0.1956	0.9144	0.2434	0.0000E+00
				1880	0.3363	0.1976	0.9239	0.2459	0.0000E+00
				1900	0.3373	0.1996	0.9334	0.2484	0.0000E+00
				1920	0.3383	0.2016	0.9429	0.2509	0.0000E+00
				1940	0.3393	0.2036	0.9524	0.2534	0.0000E+00
				1960	0.3403	0.2056	0.9619	0.2559	0.0000E+00
				1980	0.3413	0.2076	0.9714	0.2584	0.0000E+00
				2000	0.3423	0.2096	0.9809	0.2609	0.0000E+00
				2020	0.3433	0.2116	0.9894	0.2634	0.0000E+00
				2040	0.3443	0.2136	0.9989	0.2659	0.0000E+00
				2060	0.3453	0.2156	0.9994	0.2684	0.0000E+00
				2080	0.3463	0.2176	0.9999	0.2709	0.0000E+00
				2100	0.3473	0.2196	0.9994	0.2734	0.0000E+00
				2120	0.3483	0.2216	0.9999	0.2759	0.0000E+00
				2140	0.3493	0.2236	0.9994	0.2784	0.0000E+00
				2160	0.3503	0.2256	0.9999	0.2809	0.0000E+00
				2180	0.3513	0.2276	0.9994	0.2834	0.0000E+00
				2200	0.3523	0.2296	0.9999	0.2859	0.0000E+00
				2220	0.3533	0.2316	0.9994	0.2884	0.0000E+00
				2240	0.3543	0.2336	0.9999	0.2909	0.0000E+00
				2260	0.3553	0.2356	0.9994	0.2934	0.0000E+00
				2280	0.3563	0.2376	0.9999	0.2959	0.0000E+00
				2300	0.3573	0.2396	0.9994	0.2984	0.0000E+00
				2320	0.3583	0.2416	0.9999	0.3009	0.0000E+00
				2340	0.3593	0.2436	0.9994	0.3034	0.0000E+00
				2360	0.3603	0.2456	0.9999	0.3059	0.0000E+00
				2380	0.3613	0.2476	0.9994	0.3084	0.0000E+00
				2400	0.3623	0.2496	0.9999	0.3109	0.0000E+00
				2420					

ELECTRONIC CROSS SECTIONS OF
LINDHARD, SCHARFF, SCHIOTT

VITA

Ding-Yuan Samuel Day was born on September 2, 1950 in Tainan, Taiwan. He attended National Taiwan University at Taipei, Taiwan where he received the Bachelor of Science degree in Electrical Engineering with highest honors in June, 1973. He entered Michigan State University in September, 1975 and received the Master of Science degree in Electrical Engineering in December, 1976. Since January, 1977, he has been attending the University of Illinois at Urbana-Champaign. Mr. Day is a member of the Institute of Electrical and Electronic Engineers and the Phi Kappa Phi honor society.